Image Processing Methods for Myocardial Scar Analysis from 3D Late-Gadolinium Enhanced Cardiac Magnetic Resonance Images

Fatma Usta

Thesis submitted to the University of Ottawa

In partial Fulfillment of the requirements for the

Master's degree in Applied Science in Electrical and Computer Engineering

Ottawa-Carleton Institute of Electrical and Computer Engineering

Department of Electrical and Computer Engineering

Faculty of Engineering

University of Ottawa

Ottawa, Canada

To my moon and light, my mother Aynur..

Thank you, my family and friends.

Abstract

Myocardial scar, a non-viable tissue which occurs on the myocardium due to the insufficient blood supply to the heart muscle, is one of the leading causes of life-threatening heart disorders, including arrhythmias. Analysis of myocardial scar is important for predicting the risk of arrhythmia and locations of re-entrant circuits in patients' hearts. For applications, such as computational modeling of cardiac electrophysiology aimed at stratifying patient risk for post-infarction arrhythmias, reconstruction of the intact geometry of scar is required.

Currently, 2D multi-slice late gadolinium-enhanced magnetic resonance imaging (LGE-MRI) is widely used to detect and quantify myocardial scar regions of the heart. However, due to the anisotropic spatial dimensions in 2D LGE-MR images, creating scar geometry from these images results in substantial reconstruction errors. For applications requiring reconstructing the intact geometry of scar surfaces, 3D LGE-MR images are more suited as they are isotropic in voxel dimensions and have a higher resolution.

While many techniques have been reported for segmentation of scar using 2D LGE-MR images, the equivalent studies for 3D LGE-MRI are limited. Most of these 2D and 3D techniques are basic intensity threshold-based methods. However, due to the lack of optimum threshold (Th) value, these intensity threshold-based methods are not robust in dealing with complex scar segmentation problems. In this study, we propose an algorithm for segmentation of myocardial scar from 3D LGE-MR images based on Markov random field based continuous max-flow (CMF) method. We utilize the segmented myocardium as the region of interest for our algorithm.

We evaluated our CMF method for accuracy by comparing its results to manual delineations using 3D LGE-MR images of 34 patients. We also compared the results of the CMF technique to ones by conventional full-width-at-half-maximum (FWHM) and

signal-threshold-to-reference-mean (STRM) methods. The CMF method yields a Dice similarity coefficient (DSC) of 71±8.7% and an absolute volume error (|VE|) of 7.56±7 cm^3. Overall, the CMF method outperformed the conventional methods for almost all reported metrics in scar segmentation.

We present a comparison study for scar geometries obtained from 2D vs 3D LGE-MRI. As the myocardial scar geometry greatly influences the sensitivity of risk prediction in patients, we compare and understand the differences in reconstructed geometry of scar generated using 2D versus 3D LGE-MR images beside providing a scar segmentation study. We use a retrospectively acquired dataset of 24 patients with a myocardial scar who underwent both 2D and 3D LGE-MR imaging. We use manually segmented scar volumes from 2D and 3D LGE-MRI. We then reconstruct the 2D scar segmentation boundaries to 3D surfaces using a LogOdds-based interpolation method. We use numerous metrics to quantify and analyze the scar geometry including fractal dimensions, the number-of-connected-components, and mean volume difference. The higher 3D fractal dimension results indicate that the 3D LGE-MRI produces a more complex surface geometry by better capturing the sparse nature of the scar. Finally, 3D LGE-MRI produces a larger scar surface volume (27.49±20.38 cm^3) than 2D-reconstructed LGE-MRI (25.07±16.54 cm^3).

Acknowledgements

This thesis is possible due to the help and support of my supervisors Professor Wail Gueaieb from the University of Ottawa and Professor Eranga Ukwatta from the Carleton University, individually. I received an extensive support and help during my thesis and writing even during holidays. I would like to acknowledge and thank the co-authors of my two conference papers whose ideas also constructed my two methods chapters of the thesis. I would like to thank Professor James A. White from Calgary University for providing the 2D and 3D LGE-MRI dataset. I acknowledge Professor Jing Yuan for his CMF method I used at the beginning of my scar quantification study. I would like to thank Dr. Rebecca Thornhill from the University of Ottawa Heart Institute for her illustrations about the clinical manual segmentations. I also acknowledge Conor McKeen from Carleton University for his help in reconstructing 2D LGE-MRI segmentations into 3D scar surfaces that constitute the base for my 2D-3D comparison work in Chapter 4. I am indebted to Nadia El Farrag and Jinny Lee for completing the manual variability study in 3D scar segmentations for Chapter 3. I am indebted to my colleague Fatemeh Zabihollahy for valuable advice and guidance. I would like to acknowledge the help of Dr. Martin Rajchl from Empirical College of London for answering my questions regarding atlas based myocardium segmentation. For the fractal-dimension metrics calculation, I would like to thank Xander May from Carleton University Systems and Computer Engineering. I am grateful to Carleton University Systems and Computer Engineering for providing me with a laboratory space as an affiliate. I have special thanks to my mentors and friends during my masters, thank you, Amal Mohammed, Nahla Abu ElKheir, and Enas Ahraeli for supporting and inspiring me along the way.

Finally, I acknowledge the Ministry of Education of the Republic of Turkey for funding my Master's that helped me accomplish the presented work.

Table of contents

List of Figures

List of Abbreviations

2D	Two-dimensional
3D	Three-dimensional
AVE	Absolute volume error
BP	Blood Pool
CMF	Continuous max-flow
CMRI	Cardiac magnetic resonance imaging
CNN	Convolutional neural networks
CT	Computed tomography
DSC	Dice similarity coefficient
ECG	Echocardiogram
EF	Ejection fraction
FD	Fractal dimension
FWHM	Full-width-at-half-maximum
GPU	Graphical Programming Unit
GT	Ground truth
LA	Left atria
LAX	Long axis
LGE	Late gadolinium enhancement
LV	Left ventricular
MI	Myocardial infarction
MRI	Magnetic resonance imaging
NCC	Number of connected components
PDF	Probability density function

PET	Positron emission tomography
ROI	Region of interest
SAX	Short axis
SD	Standard deviation
SI	Signal intensity
STRM	Signal-threshold-to-reference-mean
US	Ultrasound
VE	Volume error
VT	VT Ventricular tachycardia
WH	WH Whole-heart

Introduction

Myocardial scarring is a complication that can occur due to ischemia or plaque formation inside the coronary arteries. Coronary arteries supply oxygen-rich blood to the heart muscle, myocardium. The fatty plaques formation will reduce the blood flow to the descending regions of clogged arteries on the myocardium. The reduced blood flow will lead to the mortality of the myocardium, which will accumulate a fibrosis tissue called scar during the healing process. The myocardial scar can disrupt the electrical conduction system of the heart. It can also cause spontaneous depolarization of the heart muscle.

The 3D segmentation of myocardial scar is important for analyzing the response of patients to the cardiac resynchronization therapy (CRT) [1, 2]. The CRT therapy is a procedure where doctors ablate around the scar tissue carefully to repair the electrical conductor system of the heart. It is important to carefully segment the scarred region prior to the CRT procedure to obtain the high achievement rate and to reduce the number of non-responders to the therapy. The 3D scar segmentation also allows for other new applications, such as computer simulations of cardiac electrophysiology [3].

0.1 Objectives

In this study, we have two main objectives. First, we want to segment myocardial scar from 3-dimensional (3D) LGE-MR images in a semi-automated manner using an optimized based segmentation method called the Continuous Max-Flow (CMF) method [4]. Our second objective is to compare the volume and the shape of the manually segmented scar geometries from 2D versus 3D LGE-MR images of same patients.

0.2 Motivation

Due to the latest advancements in image acquisition technology in the past decade, acquiring 3D high-resolution, high contrast images of the myocardial scar is now possible. These 3D LGE-MR images provide approximately one millimeter inner and outer-plane resolutions which allow for capturing finer details of scar in the out-of-plane resolution as compared to the anisotropic 2D LGE-MR images.

Although 3D scar segmentation is needed for several applications, the 3D scar segmentation methods are still limited in the literature. The existing studies either use a small number of image dataset or needs an excessive amount of user interaction to obtain decent scar segmentations. State-of-the-art deep learning methods are also working in a 2D manner and their results are validated on a small number of patients. There is a clear need for scar segmentation from 3D LGE-MR images which motivates our research in the first part of our work.

After reviewing the relevant literature, we have also encountered a gap in regards to comparing the reconstructed geometries of scar using 2D and 3D LGE-MRI. While several studies analyzed the performance of the 2D versus 3D LGE-MRI in scar mass, scar volume, SNR, and some other measures, the reconstructed scar geometry and shape analysis remained unexplored. We manually segment the scar regions from 2D and 3D LGE-MR images of same patients to analyze at the reconstructed scar volume and shape. 2D manual scar segmentation is conventionally commonly performed, yet not interpolated to 3D surfaces in the clinic. We are driven by the motivation that it is important to give clinicians insight on the implications of choosing either 2D or 3D LGE-MR images for manual scar segmentations by analyzing the scar shape based on complexity and scar morphology.

0.3 Contributions

In our study, we propose to use a continuous max-flow based scar segmentation method for 3D segmentation of myocardial scar. Using the CMF method by Yuan [4], we segmented the myocardial scar tissue within the borders of the pre-segmented myocardium without any further user interaction from 34 3D LGE-MR images. Including the CMF, six scar segmentation methods were compared to manual expert segmentations using six well-known comparison metrics including DSC, volume error, absolute volume error, normalized scar volume, precision, and recall, as well as using two statistical tests called the Bland-Altman plots and the student t-test. We contribute to the literature by reporting that the CMF method outperformed other conventional segmentation methods in almost all computed metrics including accuracy on our image dataset.

We also contribute to the scar shape analysis by interpolating 2D scar segmentations into 3D scar geometries and comparing them with 3D manual scar segmentations. We computed shape comparison metrics fractal dimensions (FD) and the number of connected components as well as the scar volumes. In on our experiments, we show that the 3D LGE-MRI method captured a more complex scar geometry than the 2D LGE-MRI in our dataset of 24 2D and 3D LGE-MRI. The 3D LGE-MRI presented a higher mean scar volume than the 2D LGE-MRI.

0.4 Statement of Originality

In this thesis, we present a semi-automated myocardial scar segmentation study which involves a 3-dimensional (3D) segmentation study of myocardial scar and a comparison study of scar geometries obtained from 2D and 3D LGE-MR images. For the 3D scar segmentation study, we propose to use an optimized based continuous max-flow (CMF) method. We segment the left-ventricular scar in a 3D manner from thirty-four 3D late gadolinium-enhanced magnetic resonance (LGE-MR) images. We utilize manually segmented myocardium as a prerequisite to scar segmentation. In our experiments, the CMF

method segments the scar tissue within the borders of the pre-segmented myocardium without any further user interactions. We compare our developed scar segmentation method to well-known segmentation methods: full-width-at-half-maximum (FWHM) and several signal-to-reference-mean (STRM) methods. We evaluate our scar segmentation method using a regional overlap metric called DSC, and several scar volume metrics. Our method outperforms the conventional FWHM and STRM methods in both DSC accuracy and volume metrics. To be able to understand the observer variability of manual scar segmentations, we also perform an inter and intra-observer variability analysis for scar segmentations from 3D LGE-MR images. We ask three different observers to segment a randomly selected subset of five 3D LGE-MR images repetitively three times on different days. The inter and intra-observer variability study shows that there are variations in segmented scar volumes among different observers and each observer also has certain variability in their own delineations when they are asked to re-segment the scar on the same dataset on different days.

In addition to the 3D scar segmentation study, we present a comparison study of 3D scar geometries created using standard multi-slice 2D LGE-MRI versus high-resolution 3D LGE-MRI. For this, we manually segment the myocardial scar from twenty-four 2D and 3D LGE-MR images. We use the 3D scar segmentations as is, while we reconstruct 3D scar models from the 2D scar segmentations using an interpolation method called LogOdds. The 3D scar geometries from 2D and 3D LGE-MRI are compared using several shape description metrics. The computed shape metrics show that the 3D LGE-MRI produces a more complex scar structure; capturing the sparse nature of the scar, having fewer disconnected regions and higher fractal dimension than the 2D LGE-MRI. Further, we present a statistical analysis of the manual scar and myocardium segmentations to compare the scar volumes obtained from 2D and 3D LGE-MR images. According to the Bland-Altman and student t-test, we found that there are no significant differences in scar volumes generated using twenty-four 2D and 3D LGE-MRI, and they can be used interchangeably. The previous studies although comparing the 2D and 3D LGE-MRI

in regards to several cardiac metrics such as scar volume, scar mass, SNR, and image acquisition times, have not explored the reconstructed scar geometries. To our knowledge, this study is the first attempt at investigating differences in scar geometries generated using 2D and 3D LGE-MR images by analyzing various shape descriptor metrics.

Based on this thesis, we have published two conference papers [5, 6] in the SPIE 2018 Medical Imaging Conference.

1

Background

Heart-related diseases are the number one cause of death globally. According to the World Health Organization, about 17 million people die worldwide of heart-related diseases every year [7]. These include diseases in the heart muscle and in the vessels of the heart. In the scope of this thesis, we are interested in a serious heart-muscle-related disease called myocardial scarring. The focus of this thesis is to develop algorithms to segment the non-viable scar tissue on the left ventricular of the heart myocardium from 3D Late Gadolinium-Enhanced Magnetic Resonance images (LGE-MRI).

In this chapter, we will first describe the context and background information pertaining to the need for segmenting the myocardial scar using 3D LGE-MR images. We will then introduce the basics of cardiac anatomy and discuss our disease of interest, myocardial scarring. We will then briefly explain the cardiac imaging planes and different imaging technologies for cardiovascular imaging. Finally, our focus will be on the LGE-MR imaging, which is a special kind of MRI for imaging the myocardial scar. We

will categorize different MRI acquisitions as 2D vs 3D.

1.1 Ischemic Heart Disease and Myocardial Scar

The heart is supplied with its nutrient vessels called coronary arteries. If fatty plaque builds up inside the arteries, this may lead to damages to the heart muscle and to the coronary artery disease (CAD). Due to the built-up plaque, the blood flow to the heart muscle is reduced or stopped in the case of a clogging. The reduced oxygen and nutrition to the heart muscle cause partial defects and tissue deaths in the locations of narrow or occluded arteries. This is called the ischemic heart disease (IHD)[8]. Any damage to the heart muscle affects the functionality of the heart to supply oxygen to the organs.

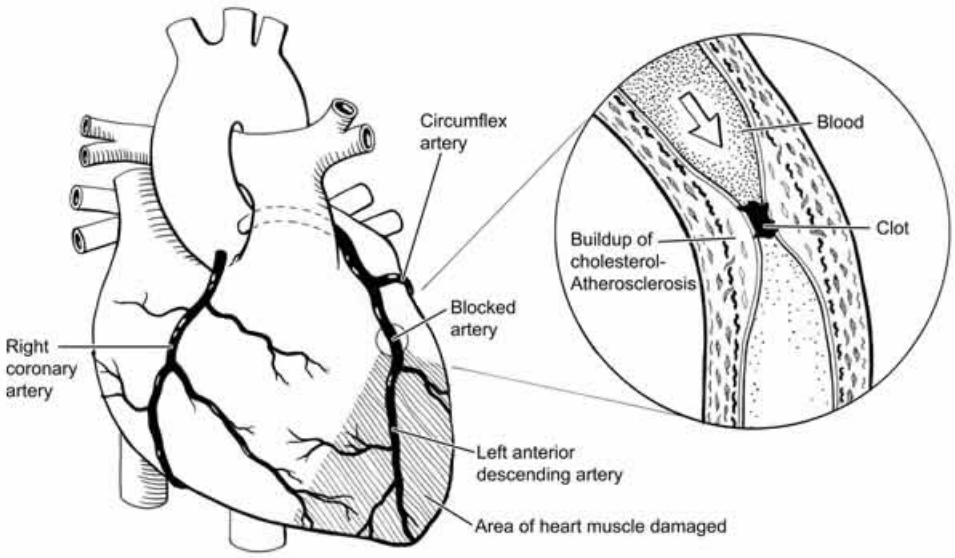

Figure 1: The occlusion of coronary arteries and accumulation of scar tissue in the area of damaged heart muscle. The image is downloaded from 'wsiat.on.ca' in September 2017.

After a coronary artery occlusion of the heart, myocardial scarring usually occurs. If the occlusion continues, the viability of the heart muscle (myocardium) cannot be sustained. During the healing process, a non-viable fibrosis tissue known as the scar is

formed on the patients' heart. Scarring of the myocardium is a major cause of heart failure and ventricular arrhythmias [9, 10]. The LGE-MRI has been used as a gold standard imaging technique for assessing the myocardial tissue viability. Scar models from LGE-MRI showed excellent agreement with the myocardial scar in histopathology [11, 12].

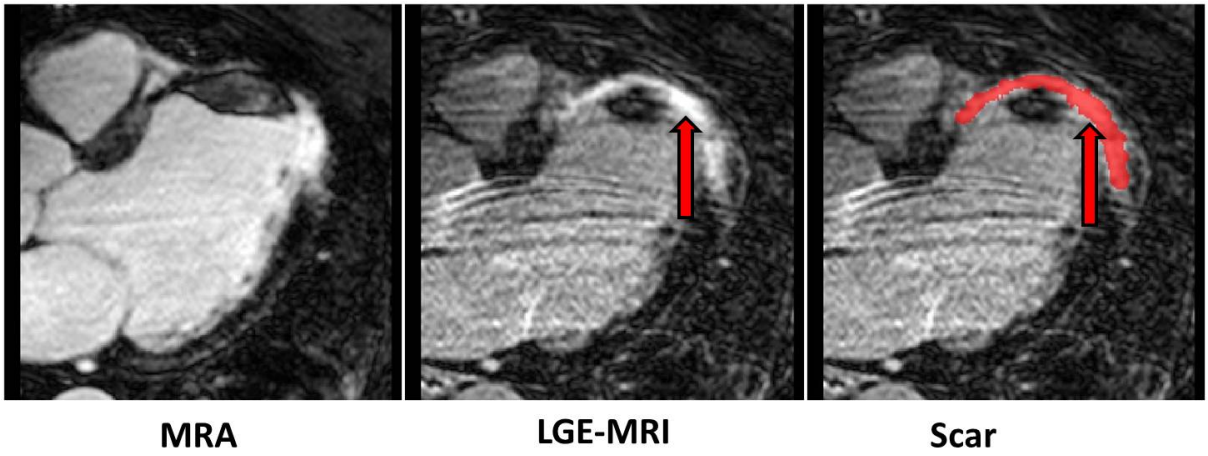

Figure 2: The MRA and LGE-MR images of the same patient with the myocardial scar. The MRA image (on the left) visualizes the heart anatomy well while the LGE-MR image (middle and the right) highlights the scar structure. The scar is manually segmented on the LGE-MR image in red (on the right).

There are two major coronary arteries in the human heart. The right coronary artery is located along the right atrium (RA) and right ventricle (RV), similarly two main left coronary arteries descend along the left atrium (LA) to left ventricle (LV). Based on which coronary arteries are blocked, the corresponding areas will vary for the scar accumulation. The damage to the left coronary arteries negatively impacts the largest heart muscle, the LV. The LV is responsible for ejecting blood through the systemic circulatory system through the entire body. The oxygenated blood circulation throughout the body and its systems depend heavily on the mechanical contraction motion of the LV. Contrary to a healthy myocardium, the scarred myocardium cannot contract properly, which yields to ventricular arrhythmias. Information related to scar size, shape, and the scar location on

the heart muscle is necessary for the planning of treatments of scar-related diseases such as ventricular tachycardias (VT) [13, 14, 15]. In Figure 1, a coronary artery blockage is seen in the myocardium. Due to the built-up plaques, the arteries narrow down which reduces the blood flow to the heart muscle in the areas of the descending arteries. In Figure 2, a medical image of the heart muscle can be seen which the myocardial scar is segmented on the image (in red). In the first image (left) the anatomy of the LV can be seen. The middle image shows the scar tissue (brighter area) and on the right, the scar tissue is segmented manually in red.

1.2 Cardiac Anatomy and Function

The heart is an electrical and a mechanical organ. It is positioned obliquely in the thoracic cavity and is surrounded by lungs from two sides [16]. The heart consists of a self-contracting muscle named as myocardium, its blood supplying coronary arteries, great valves and great arteries which carry blood in and out of the heart chambers. The electrical impulse starting from the sinoatrial node, known as the SA node initiates the contraction of the myocardium. The heart has two double chambers in which the oxygenated and de-oxygenated blood is separated. The two small chambers at the top are called atria, and the two larger chambers at the bottom of the heart are called the right and the left ventricles (RV and LV). The LV is the largest chamber of the heart which is capable of pumping blood with great force to the entire body at once. Therefore, any electrical or mechanical abnormalities in the LV of the heart lead to several complications. In Figure 3, a model of the human heart and its main chambers can be seen. The heart model includes the four blood chambers, the great vessels, and the valves of the heart. The valves are responsible for the controlled flow of the blood between atria and ventricles and the great valves.

During the systole and diastole, the part of the blood in the heart is ejected from the LV, and the ventricles refill with blood, respectively. The left ventricular ejection fraction (LVEF) is an important measure of the functionality of the heart. The LVEF

shows the percentage of the blood that is ejected from the LV at each heartbeat. If LVEF is smaller than 35%, it is an indicator of cardiac mortality, which may require an implantable cardioverter defibrillator (ICD) therapy [17].

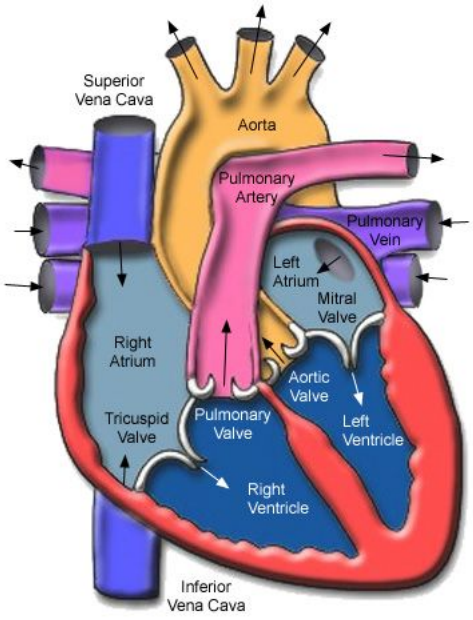

Figure 3: The four chambers of the heart: the left and right atria (RA) are at the top in light blue and the left and right ventricles (LV and RV) in darker blue are at the bottom. Also, the great arteries and veins, such as the aorta and pulmonary artery, as well as valves between atria and ventricles can be seen. The image is downloaded from 'texasheart.org' in September 2017

1.3 Anatomy of the Heart Wall

The heart wall has several diverse functioning layers. In Figure 4, a detailed wall model of the heart is seen. From the outermost to the innermost, the main layers are named as the pericardium, epicardium, myocardium, and endocardium. These layers have several functionalities such as protecting the heart from the outside (pericardium) against infection or surrounding the heart from the inside (endocardium). The yellow-painted structure on the image depicts the pericardial cavity which is filled with a fluid and

minimizes the effect of contracting motion of the heart to the surrounding organs. The epicardium includes coronary arteries that supply oxygen to the heart tissue. The myocardium is a thick muscle layer and it is responsible for the contraction motion. Lastly, the endocardium is the interior layer which holds the valves from the inside of the heart.

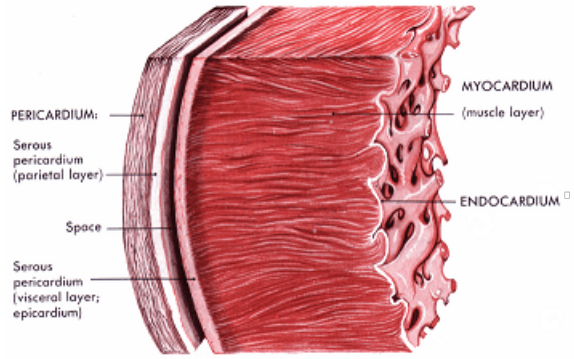

Figure 4: From the outermost to the innermost layers are the pericardium, pericardial cavity, epicardium, myocardium, and endocardium. The image is downloaded from 'scientificinformer.com' in April 2018.

1.4 Cardiac Imaging Planes and Modalities

For diagnostic cardiac imaging, medical experts benefit from several imaging modalities such as echocardiography, cardiac computed tomography (CT), cardiac magnetic resonance (MR), and nuclear myocardial perfusion imaging. These modalities use standardized imaging planes to refer to the orientation of images.

1.4.1 Cardiac Imaging Planes

For imaging the human body, the imaging modalities use standardized orthogonal planes called transverse, coronal, and sagittal planes. On the other hand, the heart is oriented obliquely in the thoracic cavity. This complex orientation of the heart necessitates specific planes for the heart imaging rather than the aforementioned standardized planes. The special heart imaging planes are called the long-axis (LAX) and short-axis (SAX) planes which are the lengthwise and widthwise lines from the center of the heart, respectively.

The SAX is the most commonly used view for the ventricular scar segmentation. The SAX images of the LV depict a donut-shape and the myocardial scar is visible through this view from the LGE-MR images. In a multi-slice 2D LGE-MRI, a heart is imaged using multi-slice (8 - 12 SAX 2D images). Figure 5 shows the body imaging planes. Figure 6 is a medical image of the heart showing the SAX and LAX views. Figure 7 shows the specific cardiac imaging planes on a model heart.

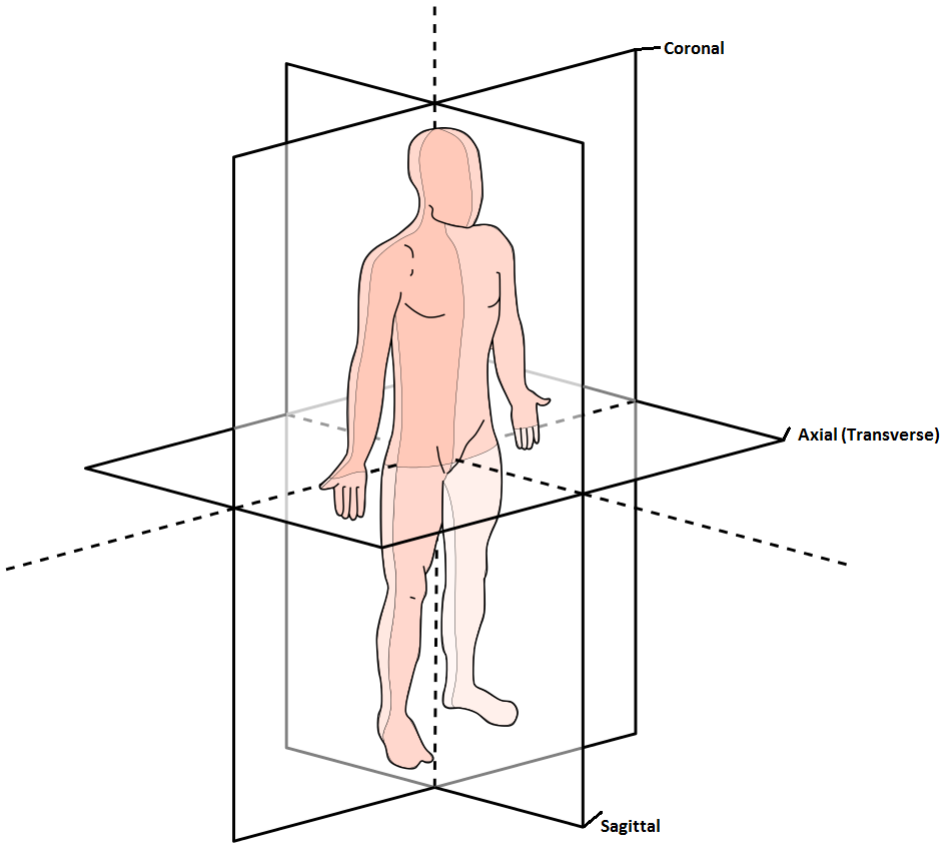

Figure 5: Standard body imaging planes or so called anatomical planes. The image is downloaded and modified from 'commons.wikimedia.org' in April 2018.

1.4.2 Ultrasound (US) or EchoCardiogram

The Ultrasound (US) is a real-time and safe imaging technology, which emits sound waves to the body and constructs an image of inner organs using the reflecting waves.

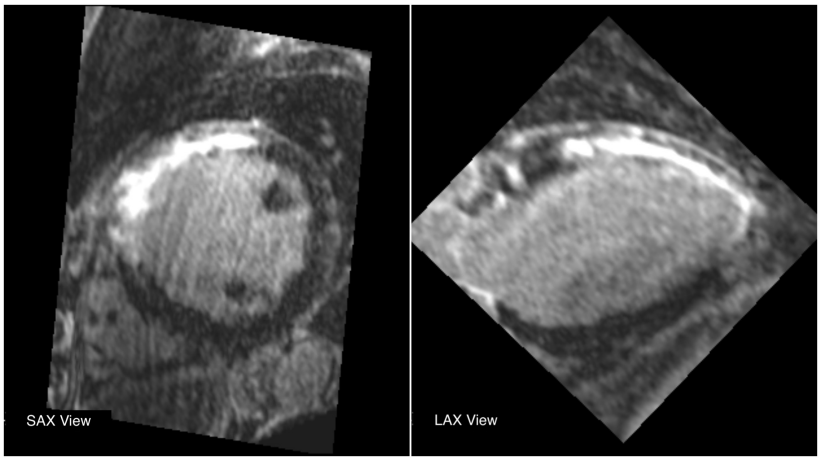

Figure 6: Short-axis (SAX) (left) and Long-axis (LAX) (right) of cardiac images.

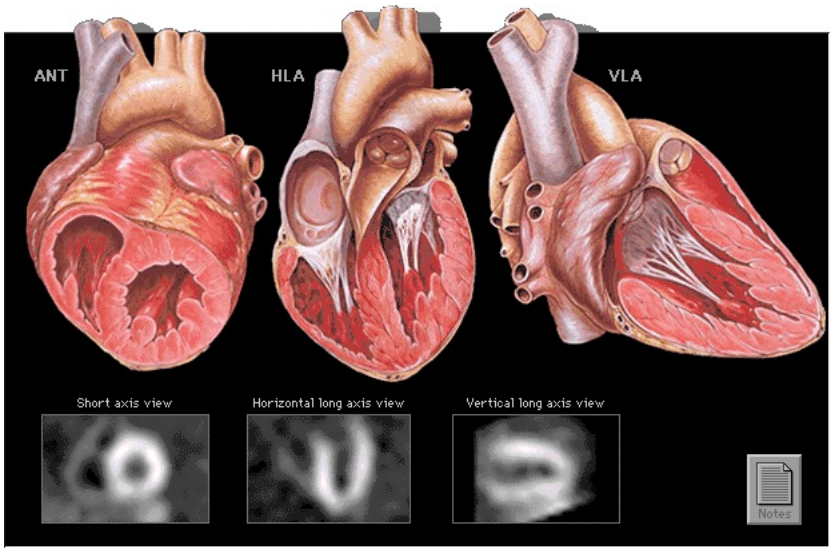

Figure 7: Short-axis (SAX) (left), four chamber (middle), and long-axis (LAX) (right) view of cardiac images. The image is downloaded from 'peninsulaheart.wordpress.com' in December 2017.

The US is a low-cost, safe, and mobile imaging modality and it can provide real-time and non-invasive images of the inner body. The US has smaller acquisition times compared to other modalities like CT and MRI. The US can provide multi-planar images of the body. Furthermore, advancements in software for processing received US waves enable US to provide 3D images of inner organs similar to the CT images. However, the US is low resolution and the acquisition and positioning of the US probe require expertise.

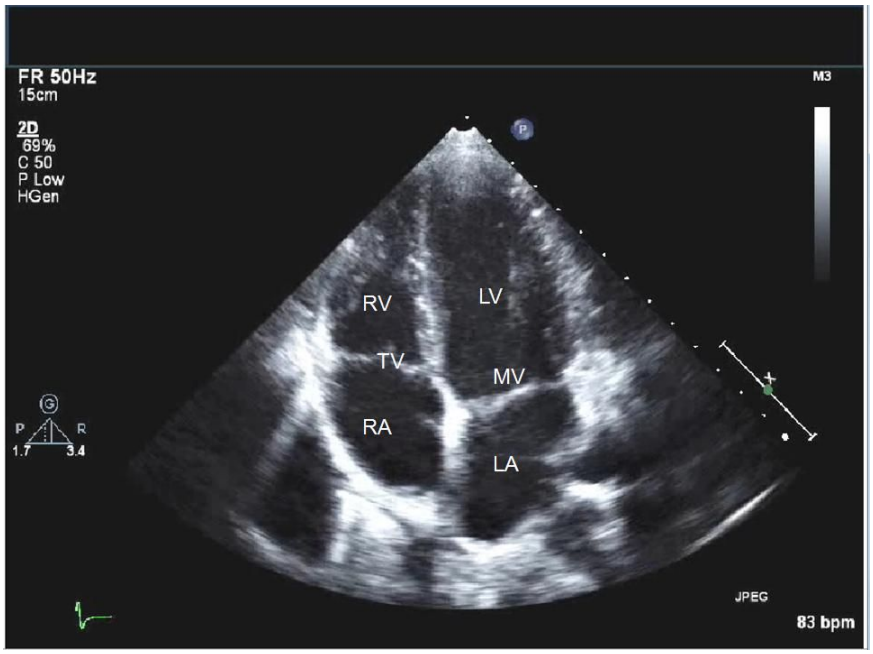

Figure 8: An echocardiogram of the heart. Four chamber view. Two ventricles and two atria are seen. The image is downloaded from 'echocardiographer.org' in December 2017.

Furthermore, a Doppler US can image the blood flow in the heart and in great vessels, and it is the gold standard for imaging valvular abnormalities.

Echocardiography is an alternative name for a cardiac US exam. It is useful to view the size and shape of several cardiac structures such as the heart muscle, heart chambers, valves, pericardium and great vessels. An echocardiogram can provide real-time images of the heart while the heart is constantly beating. Moreover, a 2D echocardiogram and the M-mode US can view the wall-thinning and systolic and diastolic functions of the heart.

Echocardiography can be used to analyze the myocardial scar [18]. Clinicians visually interpret the occurrence of the scar tissue from electrocardiogram images. Echocardiogram can assess the LV function [19, 20], LVEF [21], LV size and volume [22], and LV geometry [23]. Using these measures obtained by a US exam, a clinician can assess the myocardial viability and measure the extent of LV remodeling [24, 25]. There are several studies used to classify the scar using US images [26]. The Figure 8 shows a US image of

the heart. On the image, the right atria (RA), right ventricle (RV), left ventricle (LV), left atrium (LA), mitral valve (MV), and tricuspid valve (TV) can be observed. The LV, LA, RV, and RA are the four chambers of the heart. The TV and MV allow for unidirectional and controlled blood flow from atria to ventricles.

1.4.3 Computed Tomography (CT)

Computed tomography (CT) is a diagnostic imaging that is capable of creating high-resolution images of bones, internal organs, soft tissue and blood vessels. The CT uses radiation to produce the images of the inner organs. As CT technology is becoming cheaper, it is becoming a preferred tool for cardiac imaging. A cardiac CT computationally reconstructs cross-sectional 2D X-ray images of the heart. By using a contrast agent, a cardiac CT can image the details of arteries and veins of the heart. Cardiac CT is the gold standard modality to detect coronary artery stenosis. Clogged arteries are seen excellent on a cardiac CT [27].

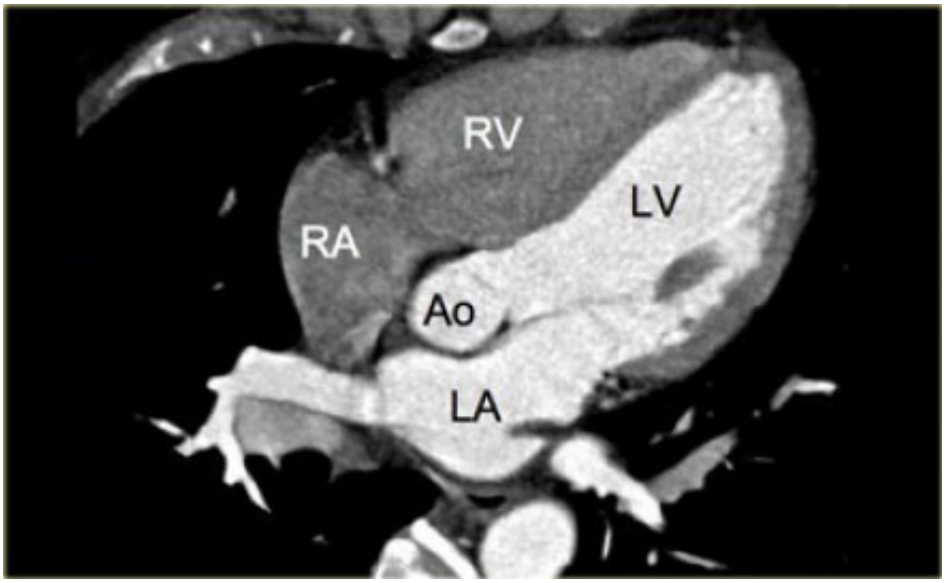

Figure 9: The four chamber view of the heart imaged using a cardiac CT. The image is downloaded from 'radiologyassistant.nl' in December 2017.

Few studies showed that cardiac CT can be used to detect the scar size and its extent.

Delayed enhanced CT is able to enhance the scar region at the cost of additional radiation exposure and injection of a contrast agent [28, 29]. A CT image of a four-chamber view of the heart can be seen in Figure 9.

1.4.4 Nuclear Myocardial Perfusion Imaging or PET

Nuclear PET imaging uses heavy radioisotope elements for imaging the body. It is called functional imaging, which is capable of imaging the metabolism of soft tissues and organs such as brain functions and the growing cancer tissues.

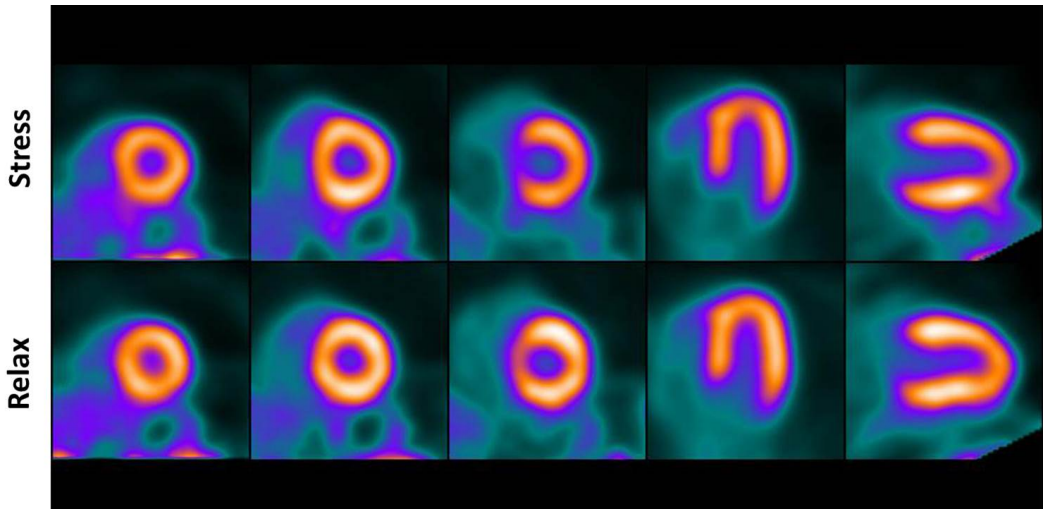

Figure 10: Nuclear Perfusion Image of a heart during stress (first row) and relax (second row) states. The image is downloaded from 'cedars-sinai.edu' in April 2018.

The PET myocardial perfusion Imaging (MPI) is an imaging technology to view the blood flow in the myocardium. Coronary artery disease can be diagnosed using a PET MPI. However, this imaging technology lacks detailed information on scar size, shape and exact location and it has a very low resolution compared to other modalities. For cardiac imaging, in particular, the heart is imaged at rest and under stress and in the case of a discrepancy between two acquisitions, perfusion imaging can diagnose the scarring of the heart.

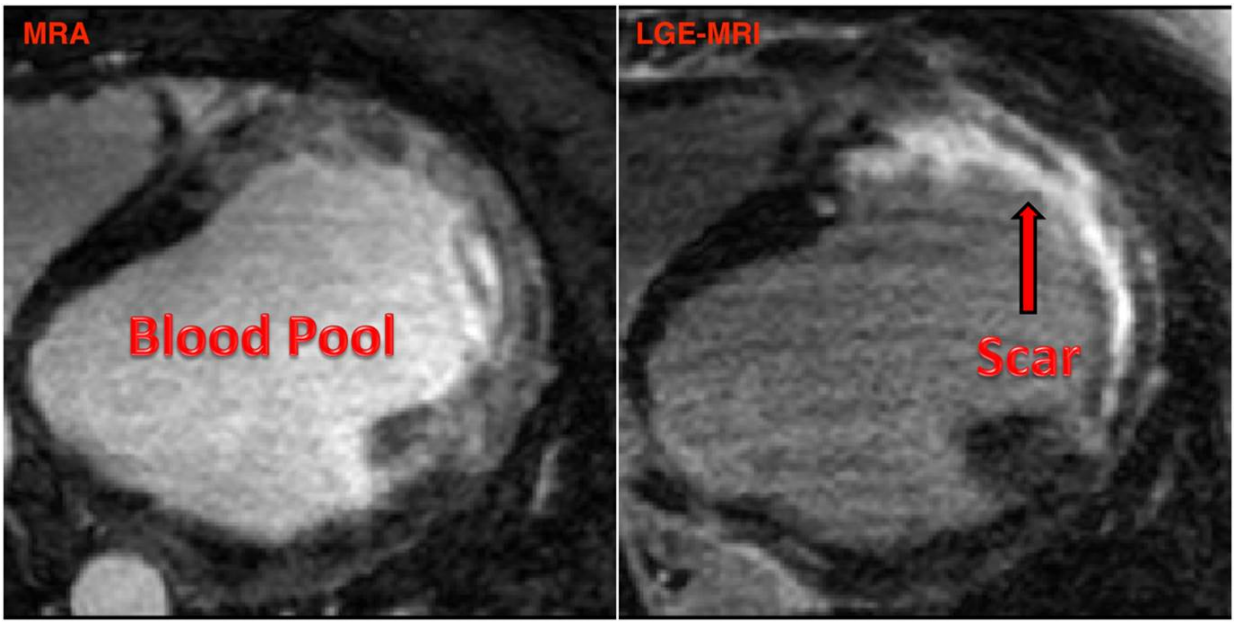

Figure 11: Short-axis view of left-ventricular using an MRA image (left) and an LGE-MR image (right).

1.4.5 Magnetic Resonance Imaging (MRI)

Magnetic resonance imaging (MRI) is a non-invasive imaging technique which can provide high-resolution and multi-dimensional images/videos of the whole body. An MRI uses high magnetic field and radio waves for imaging the inner organs non-invasively. The MRI provides high contrast and resolution of soft tissues, and it is useful for imaging both cardiac anatomy and function. The MRI provides better soft tissue contrast than a CT image; furthermore, it uses no ionizing radiation. However, the disadvantage of the MRI is its high cost. There are many different MR modalities such as CINE-MRI, T1-weighted MRI, MRA, and LGE-MRI which can be used to image the heart. These modalities can also be combined with others after the image acquisition. In Figure 12 a hybrid PET and MR images can be seen to highlight the scar tissue using a PET image on the MRA image to provide the anatomy of the myocardium.

Cinematic (CINE) MRI

Cinematic (CINE) MR images are short videos of heart motions during cardiac cycles which are acquired in accordance with the electrocardiography (ECG) signals. The CINE-MR images use ECG signals to create frame-by-frame images of the cardiac cycle from the systolic phase to the diastolic phase. The CINE-MR images are generally implemented to evaluate the cardiac function. Parameters such as LVEF, stroke volume (SV), left ventricular end systolic and end diastolic volume (LVESV and LVEDV) among others are evaluated using CINE-MRI. It is not very common to use CINE-MRI for scar quantification since the scarred and the normal tissue appears similar in image contrast.

T1 Mapping MRI

A T1-weighted image demonstrates differences in the T1-relaxation times of tissues, which is a unique parameter to all tissues in the body. This parameter is based on the longitudinal relaxation time of a tissue's magnetization vector after excitation by a radio frequency (RF) pulse. As different tissues take different amounts of time to relax back to equilibrium after RF excitation, the longitudinal relaxation time of a tissue is what determines its contrast on a T1-weighted image. In cardiac MR imaging, T1-weighted images are acquired using a gradient echo (GRE) pulse sequences pre- and post- contrast using intravenous (IV) gadolinium injection. The gadolinium will go through the circulatory system and eventually infiltrate the myocardium. Diseased myocardium typically produces an increased uptake of contrast, which helps to differentiate the scar tissue from healthy tissue.

Magnetic Resonance Angiography (MRA)

Magnetic resonance angiography (MRA) is a contrast-enhanced MR imaging technique for visualizing the anatomy of the vessels and the muscles of the heart. For imaging

the blood pool anatomy, a gadolinium-based contrast agent can be utilized. Once the contrast agent is injected into the IV bloodstream, it travels to the heart through the blood. Depending on the location of the traveling contrast agent, the MRA allows us to visualize the blood pool (if gadolinium is in the blood pool) and/or the great vessels of the heart. Gadolinium enhances wherever it travels in the blood which highlights the corresponding regions until it vanishes by the time. Once the blood pool is brighter, the myocardium area appears darker and more distinguishable. The myocardium can be identified using an MRA image, which can be utilized for segmenting the myocardium prior to the scar segmentation studies. However, MRA is not useful for scar imaging.

Late Gadolinium-Enhanced (LGE) MRI

For myocardial scar visualization and quantification, late gadolinium-enhanced magnetic resonance imaging (LGE-MRI) is a well-established tool and the gold standard imaging method. Among the aforementioned cardiac imaging techniques, the LGE-MRI is capable of capturing the detailed size, location, and extent of the scar. The LGE-MRI uses a gadolinium-based contrast agent (Gd-DTPA) that is injected into patients' bloodstream similar to the MRA imaging. The scar tissue has damaged cell-membranes which allow the gadolinium inside the intracellular space while the healthy cells with intact cell membranes do not absorb the gadolinium. 10 to 15 minutes after the injection, the gadolinium will be fully absorbed by the scarred tissue and an LGE-MR image of the heart can be acquired, afterward. The gadolinium saturated areas (scarred or fibrosis tissues) appear brighter than the others (healthy myocardium) on LGE-MR images which allows the distinction of the scar from the healthy myocardium. The Figure 11 highlights the differences between the MRA and LGE-MR image using one SAX slice of an image. While MRA highlights the blood pool, LGE-MRI highlights the scar tissue.

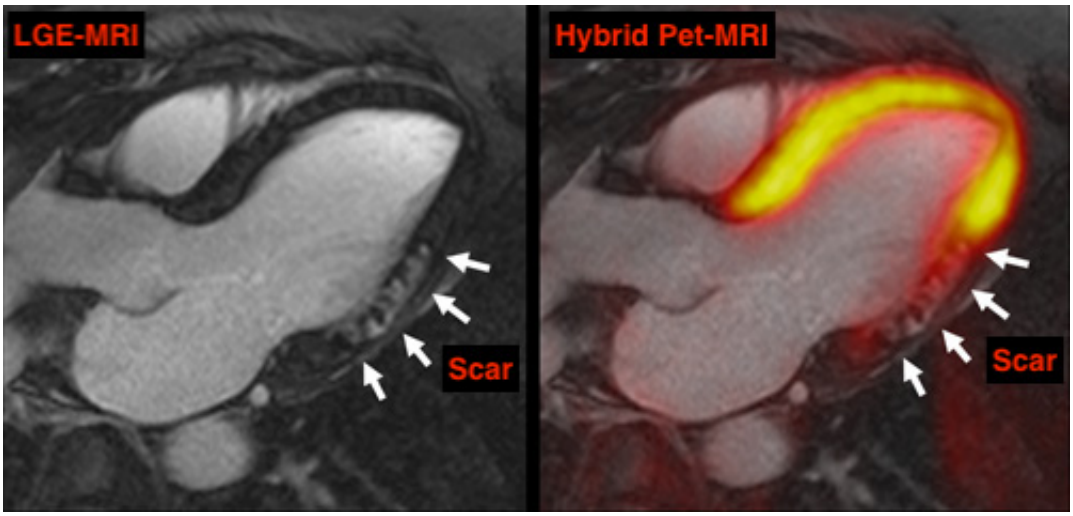

Figure 12: Long-axis view of the heart using hybrid PET/MR imaging which consists of an LGE-MRI and a PET images of the same patient. The scar tissue is non-viable; therefore, there is no activity seen on the PET image on the scarred region while the healthy myocardium appears bright. The image is downloaded from F. Nensa and T. Schlosser, University Hospital Essen, Germany and is downloaded from 'auntminnieeurope.com' in December 2017.

1.5 Image Segmentation

Image segmentation is one of the main fields of study in medical image computing. It can be described as partitioning an image into at least two meaningful areas, such as distinguishing a tumor tissue from the surrounding tissues from an image of the brain; or separating myocardial scar from the surrounding healthy tissues in a medical image of the heart. Image segmentation can be performed manually by medical experts, semi-automatically or automatically with the aid of several medical image analysis algorithms using 2D, 3D or 4D images. Cardiac medical image segmentation aims to extract clinically relevant information from the medical images of the heart for diagnosis and treatment planning.

1.5.1 Manual Scar Segmentation using 2D and 3D LGE-MRI

Manual image segmentation is usually performed by an expert radiologist for identifying and distinguishing an organ or structure of interest in a medical image. Based on their expertise and experience, radiologists can identify the diseased areas and label the related image regions by hand, using a mouse or brush tools on a computer, in a computerized but qualitative manner by eyeballing on the image. The manual image segmentation is commonly preferred due to the lack of well-established computerized methods.

For the 2D scar segmentation, the myocardium is initially segmented by tracing the endocardial and epicardial boundaries using multiple slices taken in the SAX view.The manual segmentation is performed using a commercial or open-source software such as CVI42, 3D-Slicer, ITK-Snap or several other programs of choice. After identifying the myocardial region on all consecutive image slices, the scar is then segmented on all slices within the identified region in the same manner. The present artifacts can be removed and both myocardium and scar regions care labeled accordingly.

For the 3D LGE-MRI, the manual segmentation is a very tedious task since it requires the segmentation of many image slices. A high-resolution LGE-MR image may consist of over one hundred slices. Segmenting these slices individually is time-consuming, subjective, sensitive to human error and not reproducible [30, 31]. Moreover, manual segmentation of scar is subject to high inter and intra-observer variability due to the varying experience of radiologists to define the boundaries of scar [32]. Due to the aforementioned disadvantages and challenges of the 3D manual segmentation, semi-automated and automated scar quantification methods are highly desirable. For a 3D dataset, the manual myocardium segmentation can be performed using a semi-automated segmentation method [33]. It requires relatively fewer user interactions to segment the myocardium. Afterward, the segmented myocardium can be refined and the errors are corrected by an expert manually. Then, the scar region is labeled manually using a 3D brush tool. This brush can trace several slices of a 3D image simultaneously. In the bottom left corner of the Figure 13, one slice of a masked LGE-MRI can be seen. Instead of segmenting the

myocardial scar from the full-size LGE-MR images, it is preferable to limit the region-of-interest to only myocardium area (masking) and segment the scar from only the masked LGE-MRI. For our study, an expert clinician segmented the scar manually on 34 3D LGE-MR images. Also, a semi-automated myocardium segmentation is performed and manual corrections are performed. These myocardium segmentations are used to limit the volume of interest for the scar segmentation algorithms.

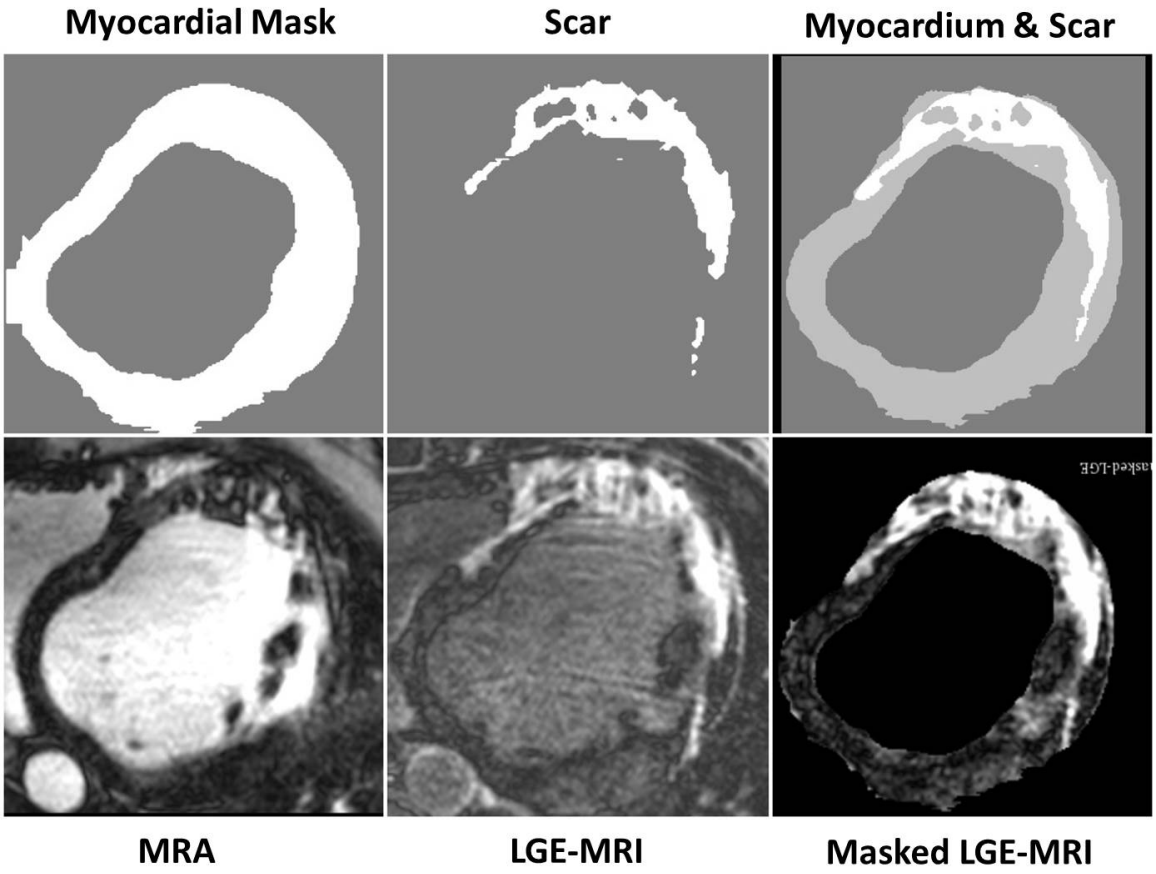

Figure 13: At the top, the manual segmentation of the myocardium (left), manual scar segmentation (middle) and the scar aligned within the myocardium region. At the bottom, there is MRA (left), LGE-MRI (middle), and the masked LGE-MRI (right). The masked LGE-MRI is obtained using LGE and the manual myocardium by element-wise multiplying the LGE-MR images and the binary myocardium segmentations.

1.6 Evaluation Metrics

To evaluate algorithm-generated results against manual segmentation results, several different measures called accuracy metrics can be employed. For comparison, manual segmentation of scar is identified as a surrogate of ground truth. By having the manual scar delineations created by an expert for the comparison, several other computerized methods can be implemented on the same dataset. After saving the resulted segmentations in binary form, these segmentation results can be compared to the manual segmentation results using several well-known accuracy metrics such as the Dice Similarity Coefficient (DSC) [34, 35], scar volume difference, or recall and precision values. One single accuracy metric is generally not enough to compare all aspects of two algorithms, so an algorithm is determined as successful if it yields to good results from several metrics, such as a high DSC accuracy value together with a low volume error [36].

1.6.1 Metrics for Comparing Scar Segmentation Results

Dice Similarity Coefficient (DSC)

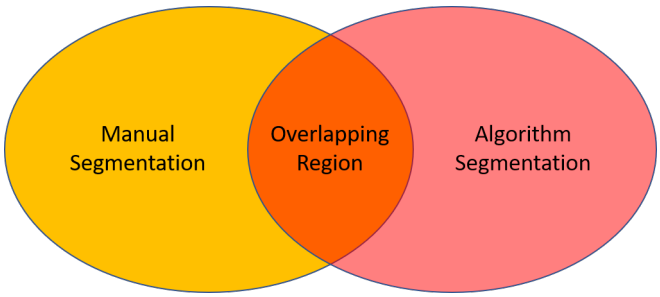

Figure 14: A visual representation of DSC overlap metric.

The Dice Similarity Coefficient (DSC) [34, 35] is a measure of regional overlap between two binary segmentations such as algorithm generated results and manual scar segmentations. The DSC metric yields an accuracy value for the algorithm segmentation from 0 to 100 in terms of the regional overlap between the algorithm generated scar

regions and manual segmentations. A DSC value of 100% represents the perfect overlap between two segmentations; whereas, a DSC value of 0% means that there is no area of overlap between two segmentations. Figure 14 shows partial overlap between manual and algorithm segmentations. The DSC overlap metric can be calculated as below;

$$DSC = \frac{2\,|S_M \bigcap S_A|}{|S_M + S_A|} \tag{1}$$

The S_M represents the spatial surface area of the manual segmentation provided by an expert, and the S_A means the surface area obtained by the algorithm segmentations. The DSC is calculated as two times the intersection of the scar generated by experts and the algorithm segmentation. Then this value is divided into the union of both segmentation results. The intersection or overlap is calculated by summing the pixels/voxels of the overlapped area. The union is calculated by summing pixels/voxels in both segmentations individually. In the case of perfect DSC, two segmentations will be identical and overlap fully which will give $\frac{2*S}{2S} = 1$.

Volume Metrics

Volume metrics are important measures for evaluating the accuracy of a segmentation since the scar volume has shown to be a predictor of the risk of arrhythmia in patients. By comparing the scar volumes between the manual segmentations versus the algorithm produced segmentations, the algorithm segmentation results can be interpreted as over or under-segmenting the scar. The volume of a scar segmentation can be calculated by multiplying the volume of one voxel with the number of voxels that are segmented as scar as follows;

$$N_{Voxels} * V_{voxel} \tag{2}$$

In the equation, N_{Voxels} is the number of voxels that are labeled as a scar, and V_{voxel} is the volume of one single voxel. The volume of one single voxel is calculated as;

$$V = d_x * d_y * d_z \tag{3}$$

where d is the voxel size of either x, y or z axis. Since voxel volume sizes are on a scale of mm, the volume of a voxel is in mm^3. The mean absolute volume error and normalized volume error are two of the many volume metrics that can be computed.

Mean of Absolute Volume Error

It is common to report the mean absolute value of scar volume differences that are generated from the manual and the algorithm segmentations for measuring the performance of an algorithm. For this, first, we calculated the volume differences between manual and algorithm generated scar segmentations for each patient. Then we took the absolute value of the volume errors. Finally, we calculate the mean of absolute volume differences over our patient dataset. The volume error is calculated as;

$$|VE| = V_A - V_M \tag{4}$$

In (4), $|VE|$ is the absolute value of volume error VE, V_A and V_M are the scar volumes generated from the algorithm and manual segmentation results, respectively.

Normalized Scar Volume

The absolute volume error yields a single number for each algorithm. While it is practical to compare single numbers representing the performance of each compared algorithms, this approach has some limitations when the scar volume is highly varying for different patients. Only calculating the mean value of the absolute volume differences might yield discrepancies when comparing different algorithms. Besides calculating the mean absolute volume differences of scar segmentations, it is also meaningful to report the fraction of the scar volume in respect to the volume of the myocardium.

One commonly used volume metric is the normalized scar volume, which represents the fraction of the scar and myocardium volumes. The fraction of the scar and the LV volumes can be calculated as V_{scar}/V_{LV}. It is interesting to see how much of the myocardium area is segmented as scar by different methods of scar segmentations. We can calculate the normalized scar volume for each scar segmentation method including the manual scar segmentations as follows;

$$\frac{V_{scar}}{V_{myo}} * 100 \tag{5}$$

1.6.2 Metrics for Comparing Scar Geometries Obtained using 2D and 3D LGE-MRI

Shape analysis of a scarred surface can be performed by using several different shape descriptor metrics. In this thesis, we utilize fractal dimensions, number of connected components, and mean volume difference as volume and shape descriptor metrics.

Fractal Dimensions

Fractal dimension is a measure of the complexity of an object. An object can be called a fractal if it presents self-similar components. It is used in mathematics for measuring the complexity of an object. It is also suggested to use for describing the pathologies of tumors [37] which may categorize them as malignant or benign based on the complexity of the shape.

The FD can be measured for both 2D and 3D objects. A 3D object can take a fractal dimension value between one and three. The more complex is an object, the higher the fractal dimension is. Figure 15 shows different FD values based on the complexity of an object. On the image, the FD calculation is shown in 2D, so the FD value is expected to be between 1 and 2. The D on the image refers to the FD.

The FD can be calculated using a box-counting or cube-counting (voxel counting in

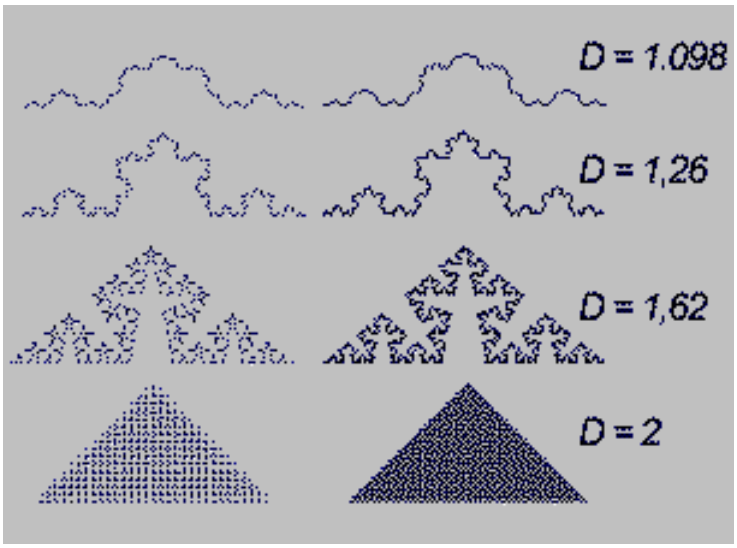

Figure 15: Fractal dimension of several 2D objects. The FD value is higher and closer to 2 when the object is more complex. The image is downloaded and modified from 'charles.vassallo.pagesperso-orange.fr' website in April 2018.

our case) algorithm. The box-counting algorithm has been utilized on 3D volumetric medical data for several different applications [38]. Reconstructed scar geometries are complex structures, so we suggest to use FD calculations for comparing the 3D scar geometries obtained using 2D and 3D LGE-MRI. The details of the FD metric can be found in Chapter 4 under 'Metrics Based on Scar Geometry'.

Number of Connected Components

The connected component analysis is a classical image processing algorithm to count the disconnected regions on a segmented image. The algorithm can count the adjacent voxels that are combined with each other based on some neighborhood. The smallest component of a 3D object will be one voxel with 6 faces, 12 edges, and 8 corners. We use the number of connected components in 3D scar geometries to compare the shape of scar geometries generated using 2D versus 3D LGE-MRI. The details of the shape metrics will be explained in Chapter 4 in the comparison study of scar geometries generated from

2D and 3D LGE-MRI.

1.7 Motivation and Thesis Outline

1.7.1 Motivation for Scar Segmentation using 3D LGE-MRI

The measures of the scar and myocardium volumes such as left ventricular end diastolic volume (LVEDV), LV end systolic volume (LVESV), LV ejection fraction (LVEF) are highly frequently associated with the cardiac death [39]. The LVEDV and LVESV are computed by segmenting the myocardium at the end of the diastolic and systolic cardiac phases of the heart. The measure of the scar extent or the scar volume is crucial to quantify because it is used together with the other aforementioned measures for analyzing the risk stratification for patients with myocardial infarction [39].

Furthermore, the quantitative analysis of myocardial scar has been found to be a predictor of future cardiovascular events in ischemic cardiomyopathy patients [40]. In other words, patients who had larger scar volume and larger scar/myocardium percentage developed further cardiovascular events as compared to other patients [40]. On the other hand, recent studies have shown potential that patients may greatly benefit from treatments utilizing non-invasive computational modeling of the scar, which can predict the risk of arrhythmia in patients [10, 41, 42, 43].

Currently, there are several imaging techniques for capturing the intact scar structure from the medical images of the heart. The most widely used technique is the two-dimensional (2D) late-gadolinium enhanced magnetic resonance (LGE-MR) imaging [44, 45]. Using the 2D LGE-MRI, the discrimination between the viable and non-viable (scar) tissue can be performed by medical experts either manually or by the aid of computers using intensity threshold-based techniques. Although being the most widely used method in the clinic, 2D multi-slice imaging has several disadvantages, mainly due to its anisotropic outer-plane resolution.

However, with the advancement of high-resolution 3D cardiac imaging technology,

nearly isotropic LGE-MR imaging for viewing the myocardial scar is available. The 3D isotropic MR acquisitions have performed higher diagnostic scores[46, 47] than the conventional 2D acquisitions due to their high resolution in any given plane. Yet, despite the advancements in 3D MR imaging technologies, methods to analyze and quantify the scar tissue on high-resolution 3D LGE-MR images are still lacking. To benefit from the advantages that 3D imaging can offer for the computational scar for the treatments of myocardial scar, robust and well-developed scar quantification and modeling algorithms are promptly needed. In this study, we have developed image processing methods for segmenting the myocardial scar from 3D LGE-MR images.

1.7.2 Motivation for Comparing Scar Geometries Obtained Using 2D and 3D LGE-MRI

Segmentation of myocardial scar is important for several applications. The degree of scar transmurality is important to assess for predicting the myocardial restoration after revascularization. Using the location and extent of myocardial scar, one can predict the response to cardiac resynchronization therapy (CRT) and implantable cardioverter defibrillator (ICD) therapy. The infarct size, shape, and location can guide ablation therapies to eliminate the ventricular tachycardias (VT). The optimum pacemaker placement is also possible by assessing the location and extent of the scar. Furthermore, scar modeling allows creating personalized computational models of the heart. These cardiac models then can be used to guide arrhythmia management therapies such as CRT.

Accurate reconstruction of myocardial scar geometry is important for creating the computational modeling of the heart to predict the risk of arrhythmia and the locations of re-entrant circuits in patients' hearts [48, 49]. Furthermore, for applications requiring intact myocardial scar geometry, reconstruction of myocardial scar geometry is important [43, 41, 48, 50]. Currently, multi-slice 2D LGE-MRI is the clinical standard for quantifying myocardial scar, which acquires transverse slices with anisotropic dimensions [51]. However, reconstructing a 3D model of the scar from 2D LGE-MR images is problem-

atic due to these anisotropic pixel dimensions in 2D LGE-MR images. Creating a scar geometry from these 2D multi-slice images may result in reconstruction errors due to the partial volume effect of 2D images. However, through the advancements in MRI technology, we can now acquire 3D LGE-MR images to compute a high-resolution and isotropic representation of myocardial scar. The 3D LGE-MRI is suitable for applications requiring reconstructing the intact scar geometry, as it is isotropic in voxel dimensions and have a higher resolution [52].

1.8 Thesis Outline

The first chapter of this thesis contains the introduction and background information of my research work. Chapter 2 provides the literature review for existing segmentation methods used in medical image segmentation with a specific focus on methods developed for left ventricular scar segmentation. The developed methods are placed in Chapter 3 which describes a scar segmentation method based on a continuous max flow (CMF) method. Chapter 4 describes our analysis of comparing scar geometries determined by 2D and 3D LGE-MRI. Results of our proposed methods can be seen after each method chapter, Chapter 3 and 4. Finally, Chapter 5 includes the summary, conclusion, discussion and future directions of the thesis work.

2

Literature Review

A considerable amount of research has been devoted to quantitatively analyze the myocardial scar from medical images of the heart. This review of the literature will be focusing on the comparison of two-dimensional (2D) versus three-dimensional (3D) imaging and the segmentation aspects of the myocardial scar. We categorize the scar segmentation studies according to two separate classes. First, scar segmentation methods are categorized as being 2D versus 3D. Second, these studies are separated between basic methods (e.g. intensity thresholding) versus more advanced methods. Some of the advanced methods include clustering methods, functional optimization methods, and deep learning methods. Finally, we employ a summary table to highlight the main features of several scar segmentation studies.

2.1 Scar Segmentation using 2D Late Gadolinium Enhanced-Magnetic Resonance Imaging (2D LGE-MRI)

In terms of image acquisitions, the previous scar segmentation studies can be divided into two groups: studies using multi-slice 2D LGE-MRI and studies using 3D whole-heart LGE-MRI. The 2D multi-slice LGE-MRI is used as a gold-standard tool for analyzing the myocardial scar since the beginning of myocardial viability assessment studies [11]. Although being the most commonly-used technique, the 2D LGE-MRI has the disadvantage of being highly anisotropic in the out-of-plane resolution. While their resolution in short-axis (SAX) view is 1-2 mm, the resolution of 2D LGE-MRI in long-axis (LAX) view is highly anisotropic (around 8 mm). The 2D LGE-MR images with anisotropic pixel dimensions represent the heart as 8 to 12 consecutive 2D images taken 10 mm apart and the images are stacked on top of each other [53]. This gap between each image slice stacks leads to the loss of information in the corresponding areas of the myocardium. Due to the anisotropic pixel dimensions of the 2D images, the SAX images are processed in a slice by slice basis along the LAX axis. The segmentation results are approximated to obtain the 3D scar volume or the volume of the heart. Slice by slice analysis of 2D LGE-MRI is sometimes insufficient when representing a complex 3D object, like the human heart. The 2D anisotropic images carry the partial volume errors, which may lead to overestimation or underestimation of the myocardial scar volume when a 3D volume is reconstructed.

Another trend in 2D scar segmentation is to utilize the pre-segmented myocardium as the region of interest before computing scar segmentation. This is because the scar tissue is present only within the borders of the myocardium. For these studies, the myocardial segmentation is either obtained manually [54, 55], semi-automatically [56, 57], or automatically [58]. In addition, some researchers obtain myocardial segmentations from other spatially registered images, such as cine-MRI [59, 60, 32].

After obtaining the myocardial segmentations either manually or semi-automatically,

the scar then can be segmented slice by slice in a 2D manner using different image processing methods. These methods are usually intensity threshold methods, or more advanced methods as will be explain in this chapter. Basic threshold methods include the full-width at half-maximum (FWHM) [54, 61, 51], signal-threshold to reference-mean (STRM) [61, 59, 54], and region growing [32]. On the other hand, the advanced techniques include support vector machines (SVM) [62, 60], clustering [63], watershed segmentation [56], and machine learning methods [58].

After segmenting the scar from multi-slice 2D LGE-MRI, then the scar segmentation results are usually compared to some expert manual segmentation results in a slice-by-slice manner. The comparison against the manual scar segmentations in regards to the overlap of the scar regions, scar volume and mass can be calculated for algorithm segmentation results. This comparison is generally made in a slice-by-slice basis and the average number of the slice-wise results is reported. To validate the algorithms, results are also compared to some conventional segmentation methods such as the FHMM and, the STRM.

2.2 Advantages of 3D LGE-MRI

The 3D LGE-MRI has established itself as an alternative to 2D LGE-MRI [53, 64, 65]. The resolution of 3D LGE-MR images is close to being isotropic in any given plane meaning; close to or less than 1 mm, i.e. 1 x 1x 1 mm^3. Recently, the 3D LGE-MR images have been utilized for myocardial scar segmentation by several researchers[52, 66, 67]. These 3D LGE-MRI acquisitions are reported as superior to 2D multi-slice LGE-MRI in terms of being able to better distinguish the scar lesions [46, 68], having better signal intensity [68] and image contrast [46], superior image quality [69], higher diagnostic quality scores [46, 47, 68, 69], and shorter image acquisition times [53, 64, 65]. The 3D LGE-MRI is also reported to capture finer details and small structures on an image, such as myocardial scar [8, 52, 70]. The high resolution 3D LGE-MRI can produce more reliable scar segmentation results [71].

Besides their high resolution, another advantage of the 3D Whole Heart LGE-MR images is that they can be acquired while a patient is freely-breathing [66, 72, 73, 73, 74] or in a single breath-hold [75, 76]. On the other hand, the multi-slice imaging has to be acquired during several breath-holds [77, 53]. Each breath-hold requires approximately 15 seconds [78]. Therefore, the procedure of 2D conventional LGE-MR image acquisition is uncomfortable for cardiac patients who have difficulty holding their breath [53]. Furthermore, with the advancements in image acquisition times, 3D free-breathing LGE-MRI requires shorter image acquisition times, which makes them more preferable than the 2D acquisitions [53, 64, 65, 71].

As a result, the advancements in the high-resolution 3D whole heart image acquisitions have increased the interest in image-guided therapies. Several researchers suggest the use of 3D LGE-MRI for scar visualization due to its high resolution [79, 80, 81]. Specifically, there are studies utilizing 3D scar models in cardiac electrophysiology studies. Moreover, the 3D LGE-MRI has been found useful in recent interventional studies such as in the ventricular tachycardia ablation [79, 80] as well as in the planning and implementation of cardiac resynchronization therapies [79, 80].

Utilizing myocardium segmentation as a region of interest is also a common practice in scar segmentation studies from 3D LGE-MRI. Several studies either used manually segmented myocardium or semi-automatically segmented the myocardium prior to the scar segmentation. Rajchl et. al. [82] utilized a semi-automated segmentation interface which segmented the scar directly from the 3D LGE-MR images while semi-automatically segmenting the myocardium, blood pool, and background along with the scar region. Myocardium region is then corrected manually by an expert.

2.3 Studies in Scar Segmentation for Comparing 2D and 3D LGE-MRI

Several previous studies compared scar segmentation methods as being 2D versus 3D LGE-MRI. Studies mainly compared the scar volume, scar mass and several other mea-

sures such as signal-to-noise-ratio (SNR), or left ventricular ejection fraction (LVEF) between the 2D and the 3D LGE-MRI. Goetti et. al. [53] assessed sixty 2D and 3D LGE-MR images for segmenting the myocardial scar in terms of produced scar volumes. The author reported that the 2D and 3D LGE-MRI can be used interchangeably with no significant difference in scar volumes. In addition, the author compared the acquisition times and reported that the single-breath-hold 3D LGE-MR images required significantly shorter acquisition times than the conventional 2D LGE-MRI while providing superior imaging of scar. Pierce et. al. [83] compared the blood SNR, image quality, and artifacts from 2D and 3D LGE-MRI and reported no significant difference in aforementioned measures between 2D and 3D LGE-MRI. Rajchl et. al. [71] compared several scar segmentation methods using 2D and 3D LGE-MR images of thirty-five patients. The author compared an optimization based segmentation method [82] and several threshold-based methods implemented in both 2D and 3D LGE-MRI.

2.4 Conventional Methods in Scar Segmentation

The majority of the studies in myocardial scar segmentation are fixed threshold methods using 2D multi-slice LGE-MRI. Although there are several known advantages of 3D LGE-MR imaging over 2D LGE-MRI, relevant computerized quantification and segmentation methods are lacking and need further exploration [71]. Current basic image segmentation methods are not successful in segmenting the myocardial scar on the 3D LGE-MRI due to the complexity of medical LGE-MR images [82, 36].

Applications of scar imaging require a 3D model of the heart and the myocardial scar. Some of these applications are the electrophysiological mapping study, and guidance of the ablation procedure of ventricular tachycardias (VT) [79, 13]. However, reconstruction of 3D scar structure from conventional 2D MRI may lead to errors due to the anisotropic dimensions of 2D images [52]. The 3D LGE-MRI is an appealing method when it comes to providing superior inner and out-of-plane resolution, which enables superior reconstruction of scar geometries than 2D LGE-MRI. Despite these advantages, little research

has been conducted on 3D myocardial scar segmentation. This thesis represents a contribution towards a better 3D left ventricle (LV) scar segmentation using 3D LGE-MR images.

2.4.1 Intensity Threshold Methods

Intensity Threshold (th) methods are the most widely used techniques in scar segmentation. These threshold methods include, but are not limited to, the FWHM [51, 54], STRM [61, 59], and manually set threshold methods [51, 54]. Other threshold-based methods include Otsu's method [84], region growing [32], region split and merge[85], and watershed methods [56].

These th methods are commonly preferred since they are easy to implement, fast, and computationally cheap. However, there are several disadvantages and challenges to using these methods. The main disadvantage is that they solely rely on the signal intensity of images. Therefore, the th method is only effective when the intensities of the target object (scar) and the background are well-separated. Furthermore, they ignore the spatial information and they cannot utilize the shape, geometry, or anatomical information of scar to obtain the desired segmentation.

Another disadvantage of the th methods is the challenge of choosing an optimal th value. The th value separates the normal myocardium from the scar intensities from within an LGE-MRI. Inconsistent image contrasts over patients hinder choosing an optimal intensity th. The th methods often use a heuristic approach to set the th value for varying image contrasts among patient groups. The FWHM method [54, 61, 51] uses half of the maximum value of all the pixels within myocardium. The STRM method sets the th value to several standard deviations (SD) from the mean intensity of a region in the remote myocardium [61, 59, 54]. Broadly used STRM methods are STRM 2-SD, 3-SD, 5-SD, and 6-SD. For example, STRM 2-SD method sets the th value as the mean signal intensity plus 2 standard deviations, as defined in (6).

$$th = \mu(I_m) + 2 * \sigma(I_m) \tag{6}$$

In (7), $g(x, y)$ represent the label for the pixel value in location (x,y) on an image I. Threshold methods assign a pixel to 1 if the intensity value is equal or higher to the th value, and assign 0 to the pixel otherwise.

$$g(x, y) = \begin{cases} 1 & for I(x, y) \geq th \\ 0 & for I(x, y) < th \end{cases} \tag{7}$$

I_m is the myocardium area within an image I, μ and σ are the mean and the standard deviation of the signal intensity of the myocardium area, respectively. Otsu's thresholding method decides on the th value automatically by calculating the minimum variance from above and below the threshold. Region growing is a variation of the th methods which starts with placing the manual seed points on the image. Region growing iteratively decides on whether to include neighboring pixels in the segmented region. Location for the initial seed point placement and the growing criteria of the region can be based on pixel intensity, texture, and color. Watershed segmentation is another heuristic image segmentation method. It treats a grayscale image as a topographic map. Brightest points represent the highest point on the map. The image segmentation boundaries are the separation lines along the ridges.

These heuristic and threshold-based approaches tend to either over- or under-segment the scar tissue. As a result, they lead to highly varying results than manual expert segmentations [36, 71]. The th methods are not suitable for cardiac imaging modalities, such as the US and the MRI, due to several image artifacts and variations in complex body structures. One example of variations is that the th methods cannot handle the false-positive scar structures on an LGE-MRI, such as the pericardial cavity or the mitral valve [36]. These structures contain liquid or fibrosis tissue, which absorb the gadolinium-based dye like a scar tissue does by nature. These well-known structures are recognized by experts by their anatomical location and are excluded from the scar region. However,

threshold methods blindly consider the brightest parts of images as a scar, so they fail in excluding these variations from the segmentation. The occurrence of these two cases can be seen in Figure 16. The figure on the left shows the pericardial cavity which is a thin layer outside of the myocardium filled with a fluid structure. The figure on the right shows the mitral valve which lets blood flow from one chamber to the other. Mitral valve appears bright on an LGE-MR image due to its fibrosis tissue content. Therefore, th methods fail to determine the false-positive structures as part of the background due to the high intensity of these regions on the LGE-MR images. To incorporate the shape and location of false-positive structures, more advanced methods needed to be used. The CMF method may distinguish these structures if texture or shape based features can be incorporated into the energy function of the method.

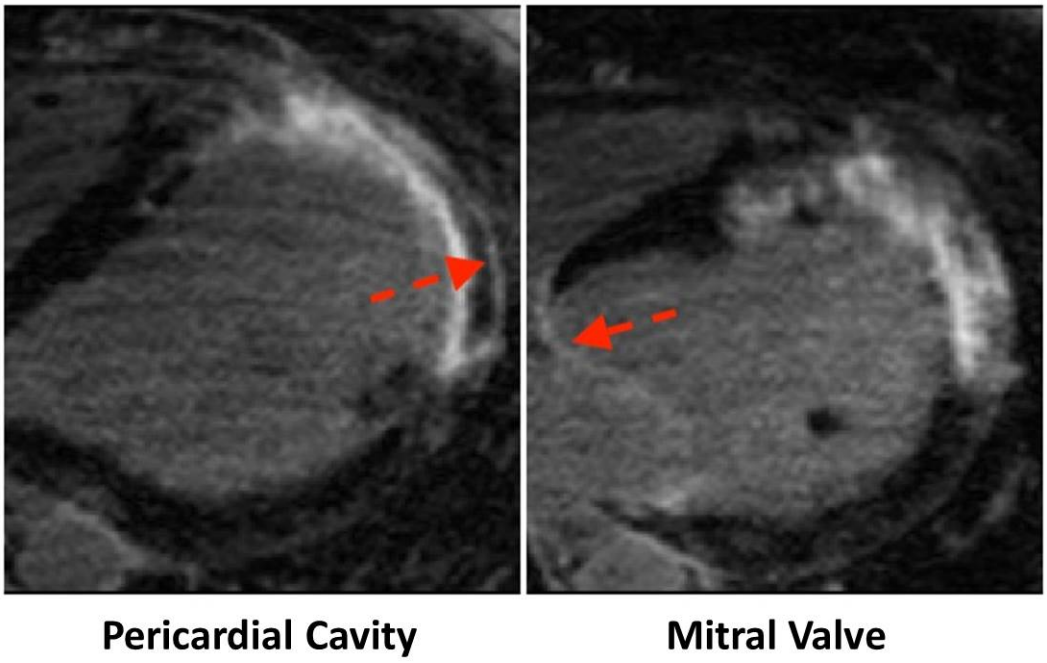

Figure 16: Two commonly seen pseudo scar structures. A pericardial cavity (left), and a mitral valve (right).

Several different results of th methods are reported in the literature by different researchers. Rajchl et. al. [71] reported 58% and 68% average DSC accuracy for FWHM and STRM-6SD methods over 35 LGE-MR images, respectively. The STRM 6-SD out-

performed other 2-SD, 3-SD, and 5-SD methods in terms of Dice similarity coefficient (DSC) accuracy. Other researchers reported that the 3-SD outperformed the other 2-SD, 5-SD and 6-SD methods in DSC accuracy and volume errors. These varying results show that the th methods are not robust in scar segmentation. For watershed segmentation, Grau et. al. [86] reported some drawbacks such as over-segmentation of the scar and sensitivity to noise on the medical images.

2.4.2 Clustering Methods

Feature clustering methods cluster pixels/voxels into groups depending on similarities in intensity, color, texture, location or some combination of these features. These techniques use some distance metrics to decide on the similarity criteria. Some feature clustering methods can be listed as support vector machines (SVM) [62, 60], fuzzy C-mean clustering (FCM)[63, 87, 88], improved fuzzy means clustering [89], mean-shift algorithm, and k-means clustering [90, 91].

Although clustering methods are able to utilize information beyond the image intensity, they cannot use smoothness constraints, anatomical and spatial information in the segmentation evolution. Therefore, they are sensitive to image noise, as in the case of the th methods. The biggest drawback of clustering methods is that the results of the algorithm are sensitive to the starting point of segmentation. Depending on different starting points, the algorithm can fall into local minima.

Several researchers reported image segmentation results using different clustering techniques on different natural and medical images. Detsky et. al.[92] segmented the scar core, gray zone, and border zone on fifteen delayed enhanced (DE-MR) images using a fuzzy clustering algorithm. The fuzzy clustering algorithm determined the probability of each voxel belonging to either if three clusters based on a distance metric. The voxels having probabilities greater than 75% were assigned to the scar core. The author compared the scar segmentation results using DE-MRI and conventional inversion-recovery gradient echo (IR-GRE). The DE-MRI yielded favorable results in terms of ability to

distinguish scar core, gray zone, and border zone areas.

2.4.3 Functional Optimization Methods

Functional optimization methods formulate a segmentation problem as an optimization problem. Typically an energy function is employed to represent a contour and this function is minimized to achieve optimal results for a segmentation problem. The main advantage of functional optimization methods over the aforementioned th and clustering methods is that the optimization methods are able to incorporate high-level information, such as shape, smoothness, and location into the desired segmentation. Some of the optimization methods are snakes [93], level sets [94], graph cuts [95], continuous max-flow [96, 4] methods and their variations. Optimization-based methods give acceptable results for several segmentation problems. Brief descriptions of these various optimization based methods are provided below.

Deformable Snakes

Snakes or Active Contours method [93] is able to provide closed and smooth contours or surfaces of objects [97]. They use a set of points to represent a contour in a parameterized manner. The idea is to start with an initial curve and allow the points on the curve to evolve iteratively to minimize an objective function. Then, iteratively modify the curve by shrinking and expanding it according to an energy function. One of the disadvantages of snakes is their dependency on local optimization. Therefore, the initial contour should be close enough to the desired contour to achieve good results. Furthermore, it is difficult to change the initially defined contour topology. The Snakes method has been used for several medical image segmentation problems such as brain lesion segmentation or myocardium segmentation. In Equation 8, E_{obj} is the energy term for the object to be segmented. E_{int} and. E_{ext} are the internal and external energy terms, which correspond to the smoothness and data terms, respectively.

$$E_{obj} = E_{int} + E_{ext} \tag{8}$$

Studies used some variations of the snakes method [97, 98] or they commonly combined the snakes method with other methods to be able to segment the complicated medical images. These hybrid methods can be seen in several studies [99, 100]. An interesting recent application of snakes method is to segment the skin cancer [100] on medical images. The snakes method is used to extract the edges of the cancer lesions, and an SVM method is used to make predictions about the type of cancer according to this shape. The author reported that the edges of the skin lesions extracted using the snakes method are 'close' to the edges that experts detected. Another author, Itai et. al. [101] segmented lung volumes as well as the abnormal areas in the lung tissues using snakes method on nine CT images as well. The author reported 0.81 true positive fraction and 0.2 false positive fraction in segmenting the abnormal regions.

Level Sets

Level sets is a frequently used optimization-based segmentation method, which is proposed by Osher et. al. [94]. Level sets method represents a contour implicitly by defining a level set function at the zero level set of a higher dimensional surface. The dimensionality of a level set function is one level higher than the object dimension to be segmented. The contour is iteratively evolved by optimizing an energy function. Let us take an image I, in a domain as $\Omega \subset \Re^3$. The $x \subset \Omega$ is one point in an image corresponding to a single spatial variable. Level set function can be defined as $\Phi(x) : |omega \rightarrow \Re$. The zero level set of this function defines the boundary as follows: $\Phi(x) = 0$. Segmentation is performed by implicitly evolving the level set function $\Phi(x)$ instead of evolving the boundary function itself. The evolution of the level set is defined as follows:

$$\frac{\partial \Phi(x)}{\partial t} + F\,|\bigtriangledown \Phi(x)| = 0 \tag{9}$$

Here, F represents the speed function. Level sets can modify the initial contour more conveniently than the Snakes method. They take into consideration the region based statistics for the segmentation. However, the major shortcoming of level sets is the computational cost. Several researchers reported scar segmentation results using level sets. Karim et. al. [36] reported 48%, 68%, and 89% mean DSC accuracy values for segmenting the scar using Level sets method using thirty poor, medium, and good quality LGE-MR images, respectively. Lara et. al. [102] also segmented the myocardial scar on thirty DE-MR images and reported around DSC of 60% accuracy. However, the author reported that the interobserver variability was high for manual scar segmentations for creating a ground truth segmentation for comparisons.

Graph Cuts

The graph cuts is another commonly used optimization-based segmentation method. The graph cuts method [95] constructs a graph whose vertices are the pixels/voxels and edges are the pixel boundaries of an n-dimensional image to be segmented. By attaching every pixel of an image to two terminals, named as the source and the sink, the object and the background pixels are separated. The separation is performed by finding the minimum cut (min-cut) that in the means of maximum flow from the source to the sink. The min-cut is the minimum cost of separating an object from a background. A model of the graph cuts technique can be seen in Figure 17, where S is the source node, and T is the sink node. A minimum cut to separate the image into two regions is highlighted in yellow. Green nodes are attached to the source and pink nodes are attached to the sink to separate the object and the background pixels.

Karim et. al. [103] reported a DSC of 93% and 87% accuracy on scar volume over ten human and ten animal dataset using graph cuts method. Lu et. al. [104] presented a semi-automated scar segmentation algorithm using graph cuts. He reported an agreement between his proposed method and the FWHM method over ten patients' image data. Both studies used a limited number of data which may have lead to inconclusive results.

Further, both researchers utilized FWHM segmentation as the ground truth which may not be a good replacement for expert manual segmentations for comparison purposes.

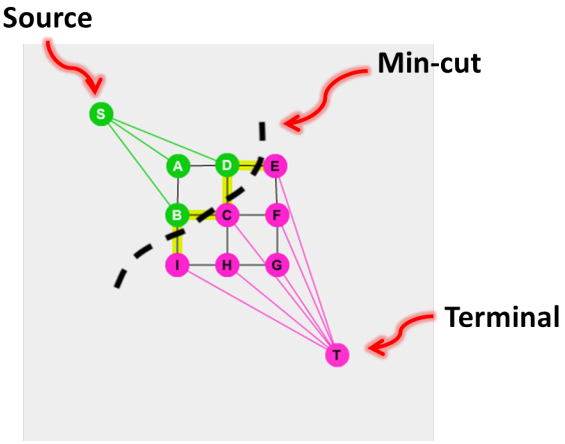

Figure 17: A 2D graph-cut representation.

Continuous Max-Flow (CMF)

Image processing applications can be modeled as energy minimization and solved by using min-cut and max-flow method [105]. Continuous max-flow method (CMF) method represents a scar segmentation problem as an optimization problem by iteratively evolving the surface of scar based on an energy function. A graph is constructed based on an image and a global minimum cut over the graph is searched using a classical min-cut and max-flow theorem. In the cost function of the CMF method, one can use image intensity, gradient, shape, and several other information.

The CMF method has the advantage of both level sets and graph cuts methods. In 3D and higher dimensions, CMF based segmentation methods outperformed the graph cuts methods in speed [106]. Moreover, a fast and global optimization method by Yuan et al. [4] has been proposed for the CMF method for quicker convergence. Previously Ukwatta et. al. [50] segmented myocardial scar from 2D LGE-MR images and reported around a DSC of 75% accuracy over 47 patients. In this thesis, we utilize the CMF method to segment the scar in 3D LGE-MRI. Therefore, the details of the CMF method will be explained further in the methods chapter (Chapter 3).

Hierarchical Max-Flow (HMF)

The Hierarchical Max-Flow (HMF) method is developed by Rajchl et al. [82]. It is an extension and a variation of the CMF [4] segmentation method developed by applying the CMF method to a multi-region cardiac segmentation problem. The HMF method segments the myocardial scar in a hierarchical manner by first separating all image pixels as cardiac and background regions. Then, it divides the cardiac region into three segments: scar, myocardium, and blood pool.

Using the HMF method, the author segmented the myocardial scar from 3D LGE-MR images in an interactive manner. The strength of the HMF is that it enforces ordered labels of different regions in the max-flow formulation. Therefore, it does not rely on incorporating the myocardial boundaries prior to the scar segmentation. Although the HMF method is independent of incorporating the myocardial segmentations into the scar segmentations, it requires progressive user interaction to achieve competitive results. The HMF algorithm yielded a DSC of 77% accuracy in around 6.5 minutes after five consecutive corrections by an experienced expert during the segmentation. However, with one single user interaction, the HMF method yielded a DSC of 54%. After five interaction, the HMF reported high DSC accuracy results (a DSC of 76

2.4.4 Deep Learning Methods

Deep Learning methods are applied to many medical imaging problems. There are hundreds of papers published in medical image computing using deep learning methods between 2016 and 2018 [107]. The motivation behind this trend is that in medical image analysis, finding the relevant features from the data and learning from them is crucial for achieving the desired segmentation results. Finding the right features that can distinguish the scar from the surrounding tissues is crucial for accurate image segmentation. Deep learning methods are not only capable of incorporating high-level information to the segmentation, they are also able to detect the features which are not intuitive to the human eye. Xu et. al. [58] segmented the myocardial scar from 2D multi-slice images

on a pixel level using deep learning methods and reported 94.35% classification accuracy over 114 patients. This method is an automated and an end-to-end quantification method for scar segmentation using 2D MRI. However, a deep learning method to analyze the myocardial scar from 3D LGE-MRI is still missing.

Convolutional Neural Networks (CNN)

One of the most commonly used deep learning approaches is Convolutional Neural Networks (CNN). Recently, CNN has become a preferred method by many researchers in medical image segmentation applications. While dealing with the medical images, the structural and spatial information is crucial to the segmentation. Regular deep learning models only allow for vectorized inputs to the network. However, this approach destroys the structural information on the neighboring pixels on the image data. The CNN is designed to incorporate the spatial information to the deep learning by allowing inputs as 2D or 3D images or patches to the network. A CNN is constructed by adding several convolutional layers, an activation layer, followed by a max pooling layer and a fully-connected layer at the end of the regular deep learning model topologies. A pooling layer is suggested to be placed right after a convolutional layer or a stack of many convolutional layers. The job of a pooling layer is to down-sample the feature maps of a previous convolutional layer. The convolutional layer is responsible for detecting local features on an image. This makes CNN extremely powerful and the preferred method for solving many image processing problems. Additional layers can be used in CNN for different purposes. To reduce overfitting, a dropout layer can be added, which randomly drops learned weights on a network at each training phase. The dropout layers prevent over-fitting and make the deep learning models perform well on both the training and the test datasets [108].

2.5 Summary

In the review of the literature, we have focused on the comparison of scar segmentation studies performed using 2D versus 3D LGE-MRI. Rather than comparing the segmentation accuracy, our purpose is to highlight the number of studies that use 2D versus 3D LGE-MR images. We also noted the amount of image dataset used to validate each algorithm. Furthermore, we listed the commonly used scar segmentation methods and provided insights on their performance in scar segmentation. We gave examples of studies using threshold methods, optimization based methods, clustering, and machine learning methods in scar segmentation. We reported results on several other medical image segmentation applications when no scar segmentation has been found using the aforementioned methods in the literature. We summarized some of the scar segmentation results in the summary table, Table 2. The publications are listed in their chronological order. In the table, we provide the author name and year as well as the citation to the related publication. The 'Dataset' column includes information related to the image dataset such as the number of patient data, the dimensionality of the data, resolution information, and the type of the images. Note that some researchers used the DE-MRI notion instead of LGE-MRI. DE-MR imaging technique utilizes a contrast agent to hyper-enhance the scar tissue and can be considered as the same as the LGE-MRI. In the table, we also highlighted the advantage and disadvantages of the presented methods.

By reviewing the literature, we observed that the dominant trend in scar segmentation is to utilize 2D LGE-MRI while the 3D LGE-MRI has superior imaging features such as higher inner and out-of-plane resolution and better contrast when compared to the 2D LGE-MRI. Although there are several attempts have been found to use 3D LGE-MRI for scar segmentation, there is still potential and need for exploring further methods in scar segmentation from 3D LGE-MR images.

After the review of the relevant literature, we have also encountered a gap in regards to comparing the reconstructed geometries of scar using 2D and 3D LGE-MRI. While

several studies analyzed the performance of the 2D versus 3D LGE-MRI in scar mass, scar volume, SNR, and some other measures, the reconstructed scar geometry and shape analysis remained unexplored.

Summary Table

Table 2: Summary table for scar segmentation methods.

Table 2 continued from previous page

Author, Year	Dataset	Accuracy	Method	Pros	Cons
Zabihollahy et. al. 2018 [109]	**12 3D LGE-MRI** 1.3 x 1.3 x 1.3 mm^3	95% DSC	CNN	Scar segmentation using 3D LGE-MRI reported excellent accuracy	Small Training and Test Dataset, Manual segmentation of myocardium required.
Xu et. al. 2017 [58]	114 2D LGE-MRI 8 mm spacing	95% DSC	CNN, LSTM	Excellent accuracy and end-to-end automated scar segmentation in the pixel level.	Used 2D LGE-MR image dataset.
Ukwatta et. al. 2016 [49]	61 2D LGE-MRI 1.5 x 2.4 x 8 mm^3	76.67% CMF2D, 73.2% CMF3D DSC	Continuous Max-Flow	No user interaction, reconstruction of 2D scar into 3D.	Myocardium segmentation needed.
Lara et. al. 2016 [36]	15 human, 15 porcine 2D LGE-MRI 1.8 x 1.8 x 8 mm^3	73% (human), 86% (porcine) Median DSC	Otsu, SVM, Level sets	Level set incorporated shape constraints to the segmentation.	Increasing run time with post-processing.
Karimaghaloo et. al. 2016 [36]	15 human, 15 porcine 2D LGE-MRI 1.8 x 1.8 x 8 mm^3	85% (human), 73% (porcine) Median DSC	Conditional Random Fields	Good accuracy in both human and porcine datasets.	Small neighborhood used for calculating scar statistics.
Alba et. al. 2016 [36]	15 human, 15 porcine 2D LGE-MRI 1.8 x 1.8 x 8 mm^3	70% (human), 73% (porcine) Median DSC	Region growing, image morphology	Deletion of false-positive scar.	Initialization required for each slice to be segmented.
Rajchl et. al. 2014 [82]	**35 LV, 15 RV 3D LGE-MRI** 1.3 x 1.3 x 1.3 mm^3	76.0% (LV), 71% (RV) scar	Hierarchical Max-Flow	Myocardium is segmented semi-automatically.	With single interaction, yielded a DSC of ∼55%.

Table 2: Summary table for scar segmentation methods.

Table 2 continued from previous page

Author, Year	Dataset	Accuracy	Method	Pros	Cons
Karim et. al. 2014[110]	15 2D LGE-MRI 0.6 x 0.6 x 4 mm^3	>80% median DSC Left Atrial scar	Graph Cuts and EM algorithm	Consensus ground truth, automated myocardium segmentation.	Lower performance when using smaller training data.
Neizel et. al. 2012 [55]	**20 3D DE-MRI**	0.94 correlation with manual scar volume	Automated Threshold method	Automated segmentation of the heart and vessels.	No comparison made with other methods.
Detsky et. al. 2009 [92]	15 2D DE-MRI 8 mm spacing	Agreement with FWHM: scar core r = 0.53, gray zone r = 0.89	Fuzzy Clustering	Infarct core and gray zone analysis.	No expert manual segmentation used for comparison.
Hennemuth et. al. 2008[56]	21 2D LGE-MRI 1.7 x 1.7 x 10 mm^3	0.95 correlation with manual scar volume	EM Fitting	Image slices misalignment correction.	Lack of different comparison methods, such as FWHM.

3

Application of Continuous Max-Flow Method on Semi-automatic Segmentation of Myocardial Scar from 3D LGE-MR Images

The 3D LGE-MRI is increasingly being investigated for assessing myocardial tissue viability. Since manual segmentation of myocardial scar from 3D LGE-MRI is a tedious task, semi-automated and fully-automated segmentation algorithms are highly desirable in a clinical setting. In this study, we developed an approach to segment the myocardial scar from 3D LGE-MRI using a Markov random field based continuous max-flow (CMF) [4] method. The region-of-interest for the scar segmentation is constrained using

manually segmented myocardium. We evaluated our CMF method for accuracy and reproducibility by comparing it to manual scar delineations using 3D LGE-MR images of thirty-four patients.

3.1 Background

The myocardial scar is non-viable tissue formed in the myocardium due to the insufficient blood supply to the heart muscle, is one of the leading causes of life-threatening heart disorders, including arrhythmias. For applications, such as computational modeling of cardiac electrophysiology aimed at stratifying patient risk for post-infarction arrhythmias, quantification of intact scar extent is required [40, 10, 49, 48]. Moreover, recently myocardial scar imaging has shown to be useful for predicting response of patients to arrhythmia therapies especially for cardiac resynchronization therapy (CRT) [1, 2] implantable cardioverter defibrillator (ICD) therapy [14, 15]. Furthermore, the reconstruction of intact scar geometry from LGE-MRI can be used for guiding the ablative ventricular arrhythmias therapies [79, 80]. However, these applications require the accurate segmentation of scar tissue from LGE-MRI.

Currently, 2D multi-slice late gadolinium-enhanced magnetic resonance imaging (LGE-MRI) is widely used to detect and quantify myocardial scar regions of the heart. However, due to the anisotropic voxel dimensions in 2D LGE-MR images, creating scar geometry results in substantial reconstruction errors [50]. For applications requiring reconstructing the intact geometry of scar surfaces, 3D LGE-MR images are more suitable due to isotropic voxel dimensions and higher resolutions [52]. Also, 3D LGE-MRI techniques, when compared to 2D LGE-MRI, have reported superior signal intensity and contrast [71], and higher accuracy and sensibility for discriminating scar [104]. While many techniques have been reported for the segmentation of scar in 2D LGE-MR images, the equivalent studies for 3D LGE-MRI are limited. The full-width-at-half-maximum (FWHM) and signal-threshold-to-reference-mean (STRM) methods are the most widely-used th methods in clinical studies. However, due to the lack of one single optimum threshold

(th) value for a big variety of medical images, these intensity th methods are not robust in scar segmentation. Other methods developed for 2D LGE-MR images are based on support vector machines (SVM), level set based watershed, graph cuts, and continuous max-flow [71]. Most of the 2D techniques are intensity th and require segmented myocardium as the region of interest for scar segmentation. For segmentation of scar in 3D LGE-MR images, only a few studies have been reported. Rajchl et al. [82] proposed a hierarchical max-flow (HMF) approach for segmenting the scar interactively, requiring ≈ 7 minutes for a single 3D LGE-MR image. Their method imposes an anatomical order of cardiac regions as label order constraints and does not need a segmented myocardium prior to scar segmentation. However, to obtain the desired accuracy, the HMF method [82] depends on an extensive number of user interactions. In this study, we propose an algorithm for segmentation of myocardial scar from 3D LGE-MR images using a CMF method. Since the myocardium needs to be segmented for building 3D models of the heart for computer simulations of cardiac electrophysiology, we propose to utilize the segmented myocardium as the region of interest for our algorithm.

3.2 Methods

3.2.1 Image Dataset

For segmenting the myocardial scar, we obtained a 3D LGE-MRI dataset containing volumetric cardiac images of thirty-five patients. All patients presented scar on the left-ventricular region of the myocardium. With the approval of the Western University Research Ethics Board, each patient provided a written consent for the study. These patients with myocardial scar underwent LGE-MRI using an inversion recovery gradient echo (IR-GRE) pulse sequence. The images were acquired from a Siemens Trio 3T MRI scanner. The imaging parameters of 3D LGE-MRI can be seen in the Table 3. The 3D LGE-MRI dataset was isotropic with 1.3x1.3x 1.3 mm^3 resolution. The 3D LGE-MR images consisted of 80 slices on average. One image is excluded from the dataset due to

Table 3: The acquisition parameters of 3D LGE-MRI dataset. [82].

Acquisition Parameters	Value
Manufacturer	Siemens Medical
Model	MAGNETOM Trio w/ Tim
Strength of Field	3 Tesla
Echo Time	1.3 ms
Flip Angle	20 degree
Pixel Spacing	1.3 x 1.3 mm
Slice Thickness	1.3 mm
Pulse Sequence	Inversion-recovery gradient echo

the lack of manual myocardium segmentation. In the dataset, the 3D scar segmentations were manually annotated by an expert clinician as the surrogate to ground truth for evaluating our algorithm segmentation results. The myocardial regions were segmented from 3D images using a semi-automated segmentation tool and manually corrected by an expert.

3.2.2 Experimental Setup and Preprocessing

As a preprocessing step, we first cropped our 3D image dataset to obtain the volume of interest of our algorithm. Afterward, we performed a linear intensity normalization on our LGE-MR images to scale the intensity values different MR images to between 0 and 255 range. Then, we applied a secondary normalization technique which is called blood pool intensity-based normalization and a myocardium intensity-based normalization [3]. Due to the variations in metabolism and health factors among different patients, the contrast agent residue in the blood pool and hence the contrast of images varies between patients. To account for this contrast variation, the blood-pool normalization is calculated using the following formula:

$$NI(i) = (I(i) - \mu_{bp})/\sigma_{bp} \tag{10}$$

I is the image, NI is the normalized intensity, μ_{bp} is the mean, and σ_{bp} is the standard deviation of the signal intensity distribution of the blood pool for each patient. We then computed the CMF algorithm on thirty-four LGE-MR images. We obtained the volumes of the binary scar segmentations in a 3D manner from the 3D LGE-MR images. We then used DSC accuracy metric to compare the scar overlap between the manual scar segmentations and the algorithm segmentations.

After normalization steps, we used our myocardium segmentation to extract the myocardium region from the images. We computed the intensity log-likelihoods manually using probability density function (PDF) calculations. For creating the intensity distribution, an n-fold cross-correlation method is used where we excluded the test image each time from the training dataset. After obtaining the PDF for scar and PDF for healthy myocardium using an n-fold cross-validation, we then applied a grid search to optimize the three parameters that were needed for smoothness term calculation of our CMF method.

We implemented our aforementioned preprocessing steps and the CMF method using a Windows Desktop with 3.40 GHz Intel Core i7 Processor and 16GB of RAM. The CMF method was written by Professor Jing Yuan from Xidian University and it was open source on the Matlab File Exchange website and it was implemented using C++ and a test function was written for the method on Matlab. The C++ max-flow calculation code was called and compiled from Matlab. Besides using these core functions in Yuan's package (et. al. [4], we also wrote several functions such as volume calculation and several volume metrics, DSC accuracy metric and several shape metrics, a 3D image loader, a 3D image visualization function, the conventional methods such as FWHM and STRM, probability distribution function (PDF) generation for the CMF method, an image normalization function, an image interpolation function.

The results of the scar segmentation from the CMF method were also compared to

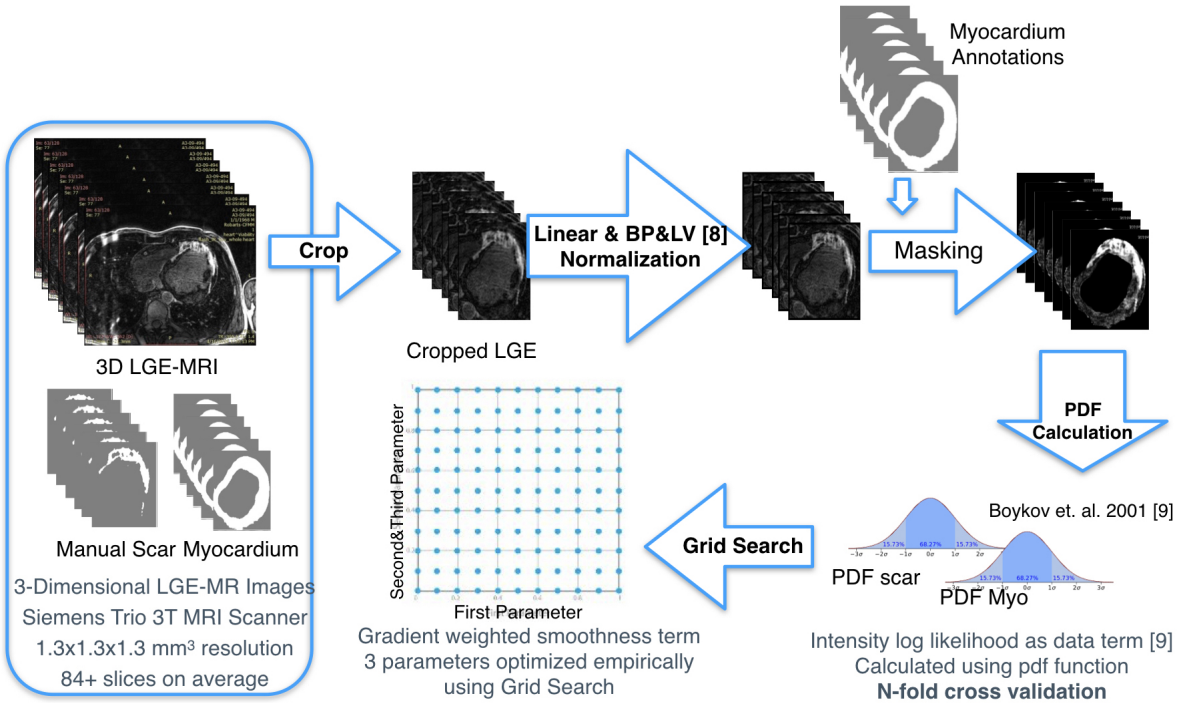

Figure 18: Image dataset and block diagram of preprocessing steps for the CMF method.

that of the FWHM and STRM methods using manual scar segmentations as the surrogate of ground truth. We used DSC accuracy, volume error (VE), absolute volume error ($|VE|$), the percentage of scar volume fraction V_{scar}/V_{myo}, precision, and recall metrics to evaluate the accuracy of scar segmentations. In this study, the $|VE|$ was calculated as the absolute value of $\frac{(V_a - V_m)}{V_a} * 100$ (%), where Va is the algorithm-generated scar volume, and w_m is the volume of manual scar segmentation. The percentage of the scar tissue within the heart myocardium is calculated by taking one hundred times the volume of the scar over the volume of the myocardium. For $V_{scar} - V_{myo}$ volume fraction percentage calculation, w_{scar} is the calculated volume for each method, and V_{myo} is the volume of manual myocardium segmentation. For comparison, we calculated the precision as $\frac{TP}{TP+FP}$ and the recall as $\frac{TP}{TP+FN}$ for each scar segmentation method.

3.2.3 The Continuous Max-Flow Method

For the CMF method, we first modeled our surface evolution as a variational formulation as follows: Let $I(x)\epsilon Z$ be a 3D image, where x represents each voxel and Z is the image intensities. The segmentation task was formulated as an optimization problem. S is an evolving surface corresponding to the foreground, the myocardial scar. The initial surface S_t evolved to S_{t+h} after time h. During this evolution, S_f^+ and S_b^+ represent the expansion of foreground and background surface regions from their first position; the initial surface region S_t. The foreground is set as the scar and the background is as the normal myocardium.

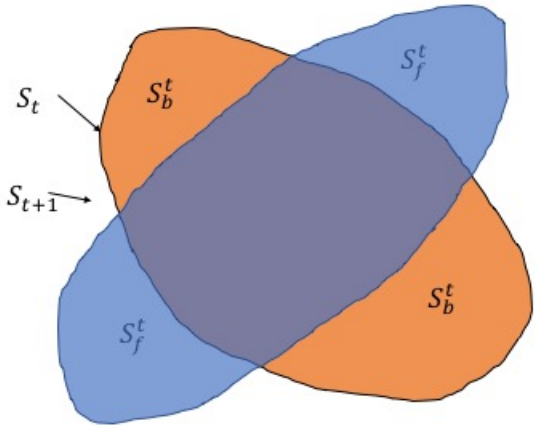

Figure 19: Surface evolution and the change in the segmented region from time t to time t+1. S_t is the surface at time t. S_f^t is the surface belong to the foreground at time t. Similarly, S_b^t is the surface belong to the background at time t.

We calculated the associated costs, e_f^+ and e_b^+ for changing a voxel label from background b to foreground f and vice versa. Function $g(s)$ is the image gradient-weighted boundary regularization term [4]. The surface is evolved from S_t to S_{t+1} based on the following energy function:

$$\min_{S}\{\int_{S_f^+} e_f^+(x)dx + \int_{S_b^+} e_b^+(x)dx + \int_{\partial S} g(s)ds\} \tag{11}$$

In Equation 11, S_f^+ and S_b^+ are the expanding foreground and background surfaces. The regions are expanded by modifying the S_t using the cost functions $e_f^+(x)$ and $e_b^+(x)$. For labeling the regions enclosed by the surface S, we used a labeling function $u(x)\epsilon\{0,1\}$, where $u(x) = 1$ when a voxel x is inside of the surface S_t and $u(x) = 0$ when the voxel is outside of the surface S_t.

We express (11) as a continuous min-cut problem and we define assignment functions $D_1(x)$ and $D_2(x)$ below:

$$D_1(x) := \begin{cases} e_b^t(x), & where \quad x\epsilon S_t \\ 0, & otherwise \end{cases}$$

$$D_2(x) := \begin{cases} e_f^t(x), & where \quad x \notin S_t \\ 0, & otherwise \end{cases}$$

Then we express (11) as the continuous min-cut problem [4] as follows:

$$\min_{u(x)\epsilon\{0,1\}} \langle 1-u, D_1\rangle + \langle u, D_2\rangle + \int_\Omega g(x)\left|\bigtriangledown_u\right| d_x \tag{12}$$

In Equation 12, $u(x)\epsilon\{0,1\}$ is a binary constraint. With that, there is a smoothness function , $g(x) = \lambda_1 + \lambda_2 exp(-\lambda_3\left|\bigtriangledown I(x)\right|)$ where parameters $\lambda_1, \lambda_2, \lambda_3 > 0$. Equation 12 is a non-linear and a non-convex problem. We can express (12) in convex relaxation form and solve it using the convex optimization theory [4, 111] as following:

$$\min_{u(x)\epsilon[0,1]} \langle 1-u, D_1\rangle + \langle u, D_2\rangle + \int_\Omega g(x)\left|\bigtriangledown_u\right| d_x \tag{13}$$

Now, the binary constraint $u(x)\epsilon\{0,1\}$ in Equation 12 is relaxed to $u(x)\epsilon[0,1]$. When we threshold the result of the new convex relaxation in (13), we obtain the same global optimum for the segmentation of (11).

Instead of solving the challenging continuous min-cut problem in (13), one can efficiently solve its dual version, the max-flow technique. The following discrete max-flow problem (14) is called the primal model and the p_s, p_t, and p are the primal constraints.

$$\max_{p_s,p_t,p} \int_\Omega p_s(x)dx \tag{14}$$

Using the primal model (14), one can formulate the primal-dual model (15) by introducing a dual variable λ to the equation. The continuous max-flow model (16) then can be calculated using the equivalent primal-dual model as follows;

$$\max_{p_s,p_t,p} \min_{\lambda} \int_\Omega p_s dx + \int_\Omega \lambda(divp - p_s + p_t)dx \tag{15}$$
$$s.t. p_s(x) \leq C_s(x), p_t(x) \leq C_t(x), |p(x) \leq C(x)|$$

When re-arranged, the primal-dual model yields to 16.

$$\max_{p_s,p_t,p} \min_{\lambda} \int_\Omega \{(1-\lambda)p_s + \lambda p_t + \lambda divp\}\, dx \tag{16}$$
$$s.t. p_s(x) \leq C_s(x), p_t(x) \leq C_t(x), |p(x) \leq C(x)|$$

For further details of the continuous min-cut/max-flow method, the readers are referred to the paper by Yuan et. al. [111].

For the calculations of the continuous max-flow method, we used an intensity log-likelihood as the data term. The intensity log-likelihood [112] was computed as follows; probability density functions (PDF) for scar and normal myocardium were created from a training dataset using manual scar segmentations. $w_i(I(x))$ is the PDF of the scar region, where [w_i is the possibility of a voxel x, to belong to the scar region according to the local intensity information I(x). Similarly, w_b is the PDF of the normal myocardium region, the underscored b indicates the background, which is interchangeably used instead of the myocardium. The intensity log-likelihood can be computed as $p_{i(x)} = -logw_i(I(x))$. The variational formulation in (11) is formulated as an equivalent continuous min-cut problem, which is then formulated as a continuous max-flow problem [111]. The CMF

Table 4: Parameters of CMF method.

λ_1	λ_2	λ_3
0.2	0.1	1

formulation can be seen in Figure 20. The evolution of surfaces can be expressed as a variational model, which then can be formulated as a continuous min-cut model and solved as its dual, the continuous max-flow model. The flow chart for the CMF calculations can be seen in Figure 20.

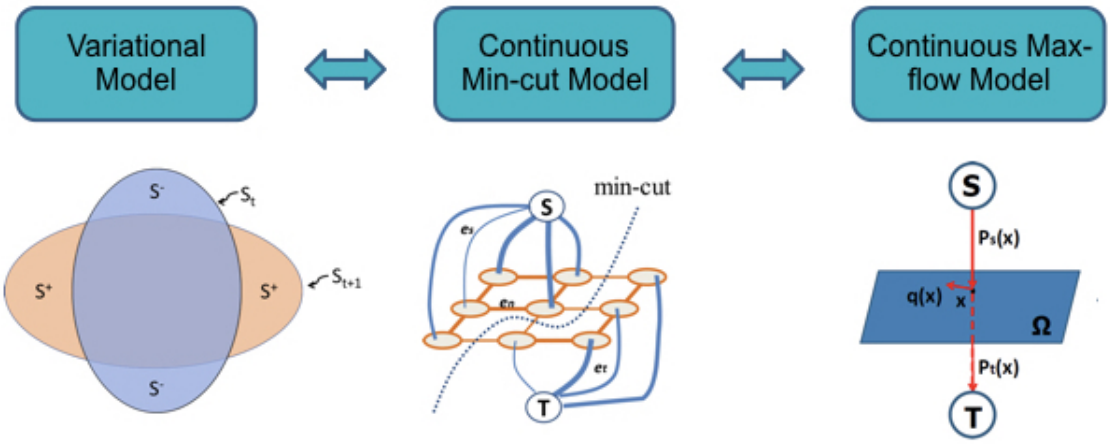

Figure 20: The flow-chart for the CMF formulation.

3.2.4 Parameter Optimization

For the developed CMF method, there was a set of parameters to be optimized. A range of three most effective parameters was selected for optimization. The required parameters were empirically optimized by changing one parameter at a time while keeping other parameters constant. These parameters were called λ_1, λ_2, and λ_3. The λ_1 controlled the smoothness of the segmentation boundaries and the λ_2 is related to the image gradient. The optimal set of these parameters after training were 0.2, 0.1, and 1 for the λ_1, λ_2, and λ_3, respectively. Table 4 shows the optimal values of the three most effective parameters used for the CMF method.

3.3 Results

We present some visual results for the scar segmentations and their surface rendered results from four different methods including manual segmentation, CMF, FWHM, and STRM 3-SD methods. We selected the STRM 3-SD method randomly among other STRM methods for visual comparisons. We show single slice views of scar segmentation results from three different patients. For this, we selected three different patients which the CMF method yielded high accuracy (DSC $>$ 80%) in Figure 21, medium accuracy (DSC $>$ 60%) in Figure 22, and low accuracy (DSC $<$ 50%) in Figure 23 for the regional overlap with the manual scar segmentation results, respectively. As it can be seen from the images, the scar geometries of CMF (in pink) and FWHM (in yellow) methods mostly visually agree with the manual expert segmentations (in red). However, the STRM 3-SD method tends to over-segment the scar for almost all cases.

The algorithm-generated results for the scar segmentation were compared to the expert manual segmentation results using several commonly used similarity metrics. As shown in Table 5, the results were presented for scar segmentation from 3D LGE-MR images using six different scar segmentation methods using six different comparison metrics. According to the table, the CMF method reported the highest accuracy in DSC as compared to other segmentation methods. Particularly, the CMF algorithm yielded a mean DSC of 72.18 $\pm$ 8.51% for our dataset of thirty-four images, whereas the FWHM and STRM 5-SD methods resulted in a mean DSC of 59.77 $\pm$ 12.29 %, and 58.31 $\pm$ 15.19%, respectively. The other STRM methods such as STRM 2-SD, 3-SD, and 6-SD performed worse than the STRM 5-SD method. The CMF method, as well as yielding the best regional overlap with the manual scar segmentation, also reported the lowest volume error $|VE|$, when compared to other presented methods. The $|VE|$ between the CMF and the manually segmented scar was 15.42$\pm$14.1 cm^3, while the FWHM resulted in a higher $|VE|$ of 21.31 $\pm$25.4 cm^3. The STRM 2-SD method over-segmented the scar and it yielded the highest $|VE|$ of 110.71$\pm$69 cm^3 when compared to the other methods.

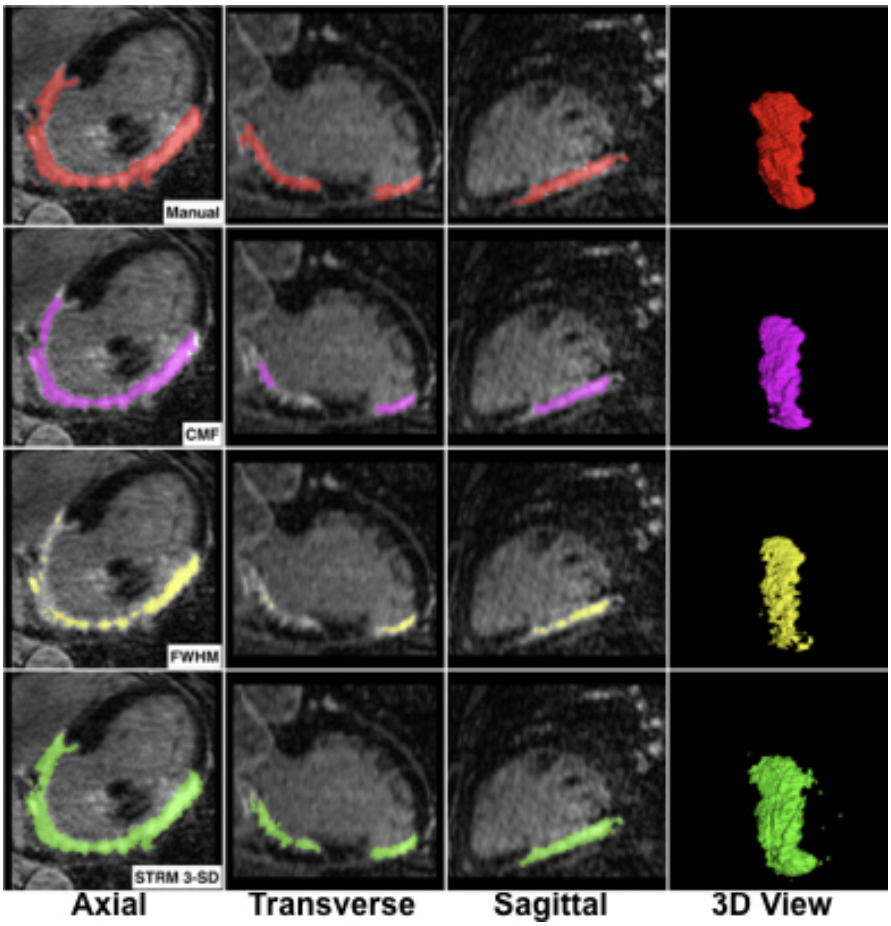

Figure 21: An example segmentation of scar from four different methods. The CMF method performed the best among other presented methods for 34 patients. The columns from left to right represent the segmentation of different views of the heart, the transversal, axial, and coronal. The rows represent different methods. The red segmentations are the manual expert segmentation of scar. Below, in pink is our proposed CMF method, in yellow, is the FWHM, and the green is the STRM 3-SD method.

Among the STRM methods, the STRM 5-SD reported the lowest $|VE|$ of 25.88±29%, which was slightly higher than the $|VE|$ of the FWHM method.

Besides comparing the regional overlap, absolute scar volume error, scar volumes, and normalized scar volumes for the algorithms, we also compared the normalized scar volume percentages, V_{scar}/V_{myo}, of the presented methods. We calculated the V_{scar}/V_{myo} of $10.10 \pm 6.20\%$ for the manual scar segmentation. The CMF method yielded the closest

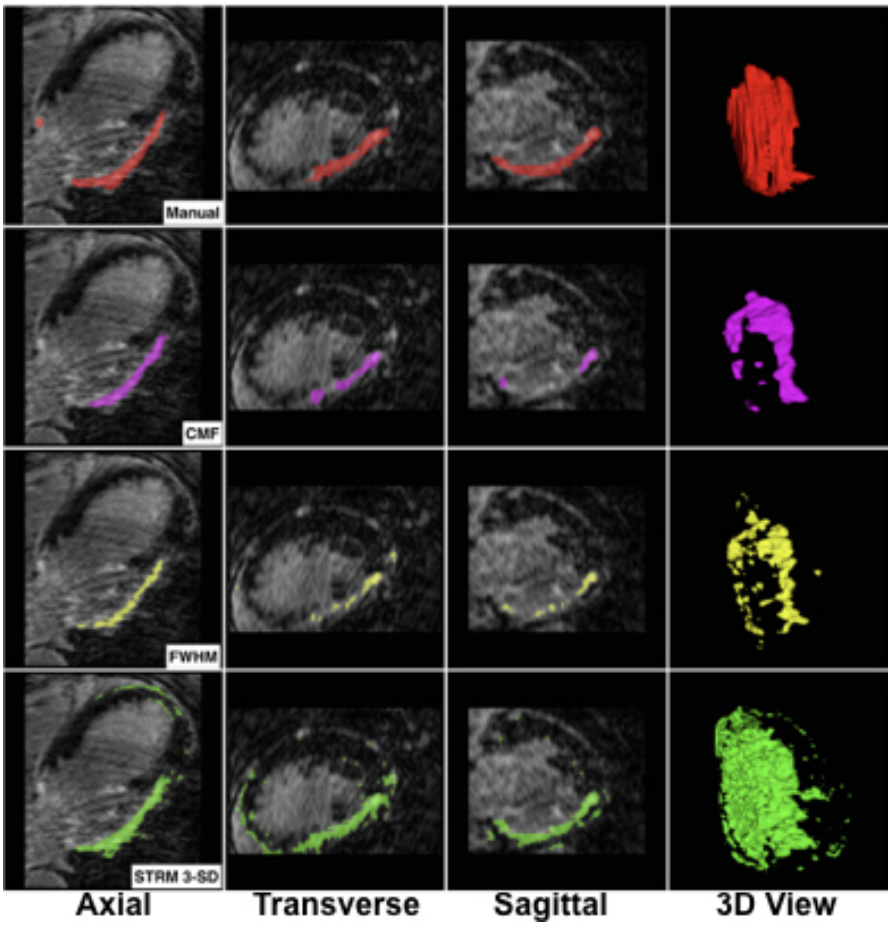

Figure 22: An example segmentation of scar from four different methods. The CMF method performed average among 34 patients. The columns from left to right represent the segmentation of different views of the heart, the transversal, axial, and coronal. Rows represent different methods. The red segmentations are the manual expert segmentation of scar. Below, in pink is our proposed CMF method, in yellow, is the FWHM, and the green is the STRM method.

V_{scar}/V_{myo} percentage, 10±6.16%, to the manual scar volume percentage among all of the six methods presented. The FWHM, STRM 5-SD and STRM 6-SD methods under-segmented the scar and reported low V_{scar}/V_{myo} values of 6.01±3.61%, 7.13±2.47%, and 3.73±1.93%, respectively. The rest of the STRM methods over-segmented the scar and they produced very high V_{scar}/V_{myo} values of 20.19±5.5% and 35.17±9.6 % for STRM 3-SD and STRM 2-SD methods, respectively.

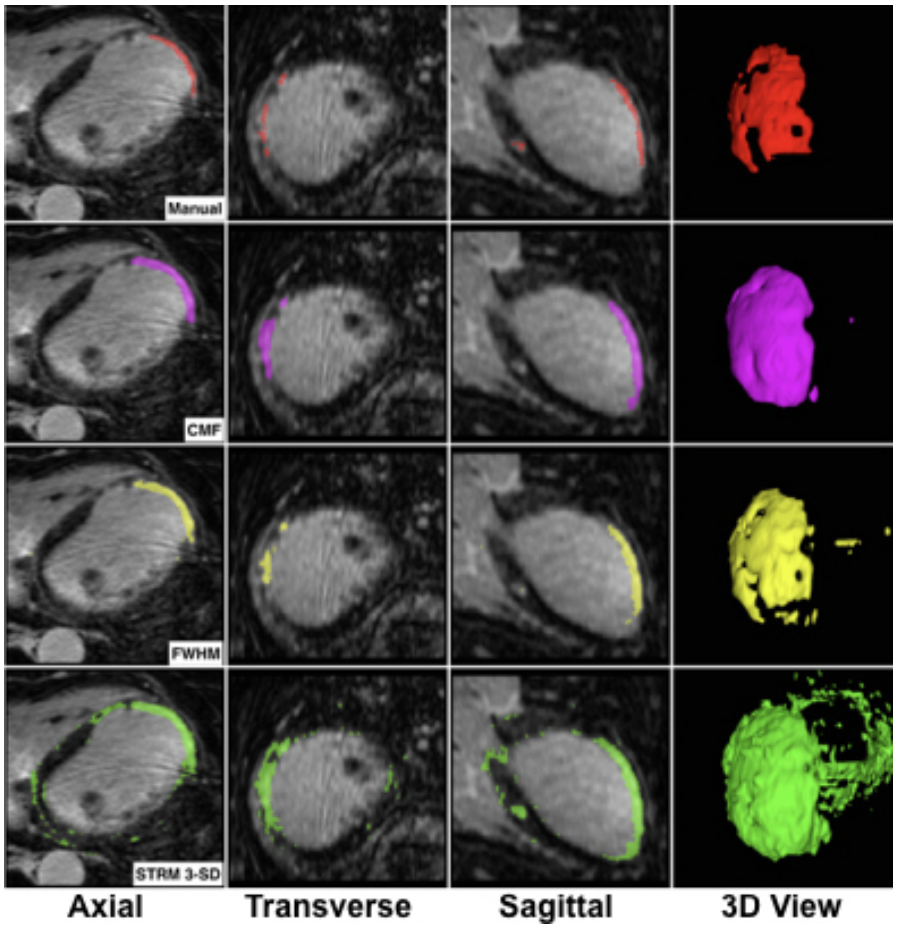

Figure 23: An example segmentation of scar from four different methods. The CMF method performed the worst among 34 patients. The columns from left to right represent the segmentation of different views of the heart, the transversal, axial, and coronal. Rows represent different methods. The red segmentations are the manual expert segmentation of scar. Below, in pink is our proposed CMF method, in yellow, is the FWHM, and the green is the STRM method.

The CMF method presented the highest precision result of 82.43±12.2 % among six different methods. The FWHM and the STRM 6-SD methods reported comparable precision results, which were 79.58 ±14.78% and 81.94±21.47%, respectively. The CMF and STRM 3-SD methods also reported high recall values of 92.84 ± 9.56% and 91.74±9.46%, respectively. The STRM 2-SD method reported the highest recall value of 98.13 ± 3.02%. While its high recall value, STRM 2-SD method reported the lowest

Table 5: Validation of scar segmentation results from CMF, FWHM, STRM 2-SD, STRM 3-SD, STRM 5-SD, and STRM 6-SD methods using six different comparison metrics.

	CMF	FWHM	STRM 2-SD	STRM 3-SD	STRM 5-SD	STRM 6-SD
DSC (%)	72.1± 8.5*	59.7± 12.3	43.48± 23	56.3±22	58.3±15.19	45.5±17.9
VE (cm^3)	4.79±20.4*	-19.8±26.6	110.7±69.1	42.9±44.5	-15.5±35.7	-30.4±36.9
$\|VE\|$ (cm^3)	15.4±14*	21.3±25.4	110.7±69.1	47.8±39	25.8±29	33.7±33.9
V_{scar}/V_{myo}(%)	11.47±6*	6±3.6	35.17±9.6	20.1±5.5	7.13±2.5	3.73±1.9
Precision (%)	82±12*	80±15	31±20	47±25	72±24	82±21
Recall (%)	92.8±9.5*	52±18	98.13±3*	91.7±9.4	61±22	41±25

precision value of 31.20±20.35% among the six methods. The CMF method required 1.8 seconds of computational time for segmenting one whole-heart 3D LGE-MR image on average.

Qualitatively, we created box-plots for the DSC and the $|VE|$ values of the scar segmentation results from six compared methods. As shown in Figure 24, the CMF method reported the highest mean DSC value over thirty-four images as well as one of the lowest standard deviation value after STRM 5-SD. The FWHM method yielded slightly higher DSC value than the STRM 5-SD method. Among all STRM methods, the STRM 5-SD performed the best in terms of DSC, volume error, absolute volume error, normalized scar volume, and precision.

Figure 25 shows the box plots for the absolute volume error values of several scar segmentation results when compared to the manual scar segmentations. The CMF and FWHM methods have almost equivalent scar volume errors. The CMF method presents the lowest absolute volume error and the lowest standard deviation. The STRM 5-SD method outperformed other methods in scar volume error.

Figure 26 and 27 show the box plots for the scar volume error values and normalized

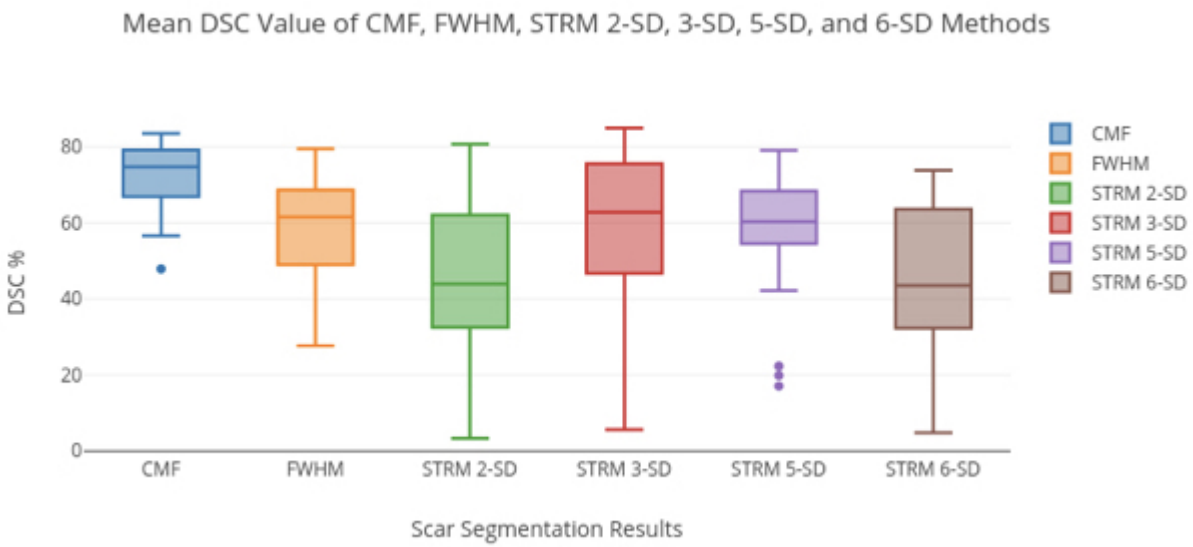

Figure 24: Box-plots represent the DSC results of several scar segmentation methods including CMF, FWHM as well as STRM 2-SD, 3-SD, 5-SD, and 6-SD methods. The CMF method yields the highest mean DSC accuracy and the lowest standard deviation among other methods.

scar volumes of several scar segmentation results. According to the box-plots, the CMF method yielded the closest scar volume and normalized scar volume values to the manual scar volumes.

For comparing the volume of several scar segmentation results against the volume of expert manual segmentation results, the Bland-Altman analysis was performed. The CMF method showed $4.79 \pm 20.18\ cm^3$ bias when compared to the manual segmentation results using thirty-four 3D LGE-MRI. The majority of the data lied between the upper and the lower limit of agreement (LOA). The FWHM method reported -19.83 $\pm$ 26.20 bias. However, the STRM methods showed a significant bias when compared to the manual expert segmentation results. The bias values were 110.71, 42.91, -154.9, and -30.44 for STRM 2-SD, 3-SD, 5-SD, and 6-SD methods, respectively. The smallest bias was reported for STRM 3-SD among different standard deviations of the STRM methods. The results of the Bland-Altman analysis indicated that the CMF method reported lower volume errors when compared to other scar segmentation methods. Therefore, the CMF

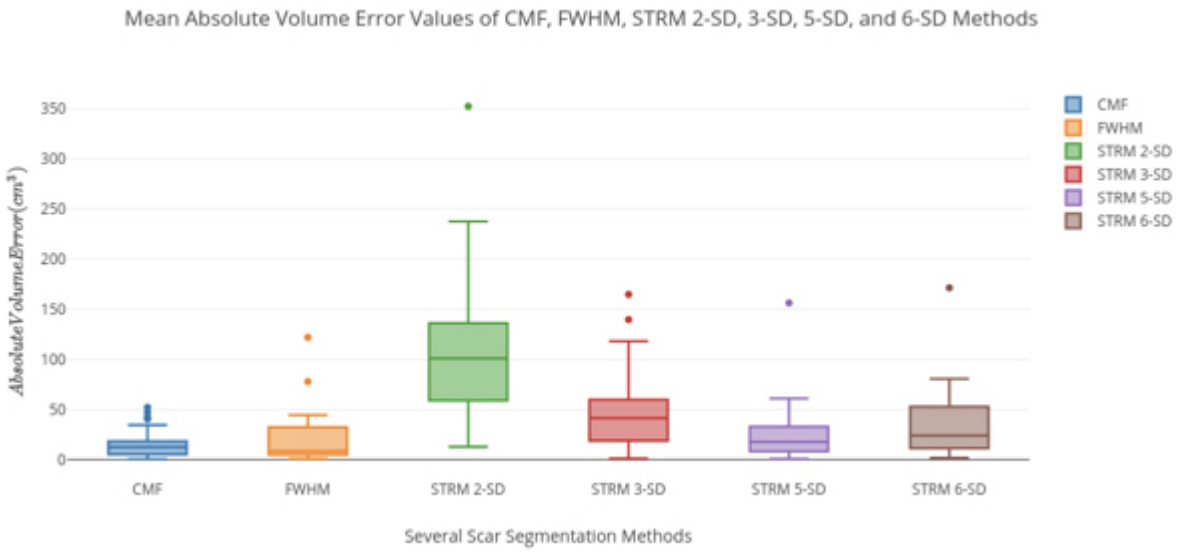

Figure 25: Box-plots represent absolute volume error results of several scar segmentation methods. The box-plots also compare results of 2-SD, 3-SD, 5-SD, 6-SD addition to the FWHM and CMF methods.

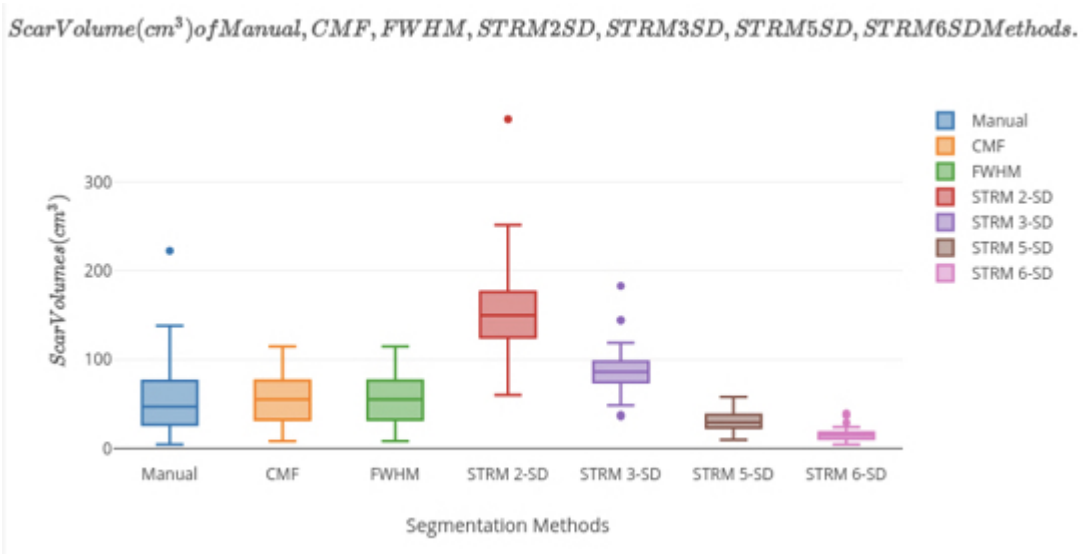

Figure 26: Box-plots represent scar volume results of several scar segmentation methods.

method can be used interchangeably with the manual segmentation.

For the paired student t-test, we set the null hypothesis, H_0, as there is no difference between manual segmentation and algorithm generated scar volume measurements. For

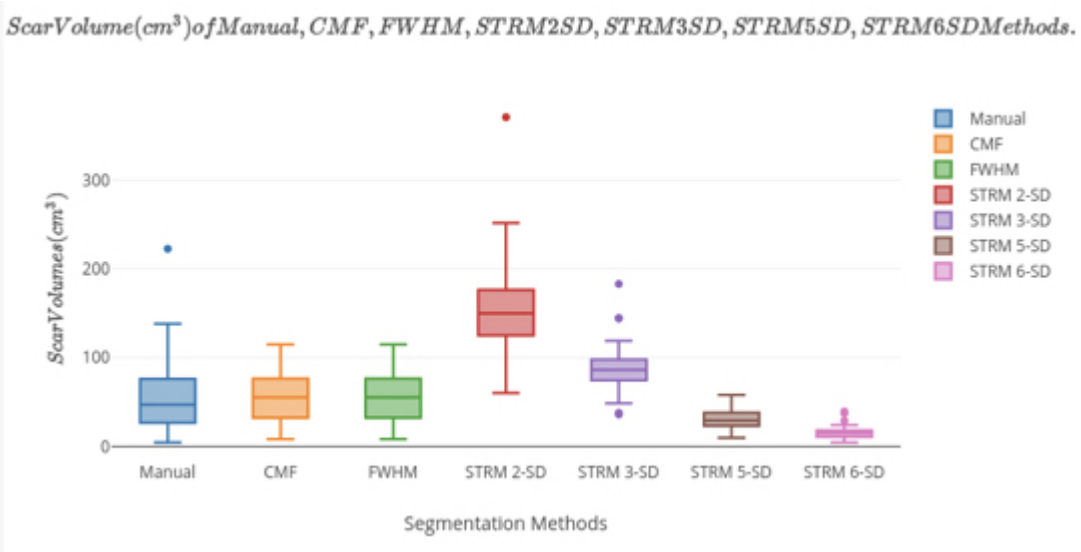

Figure 27: Box-plots represent the normalized scar volume results of several scar segmentation methods.

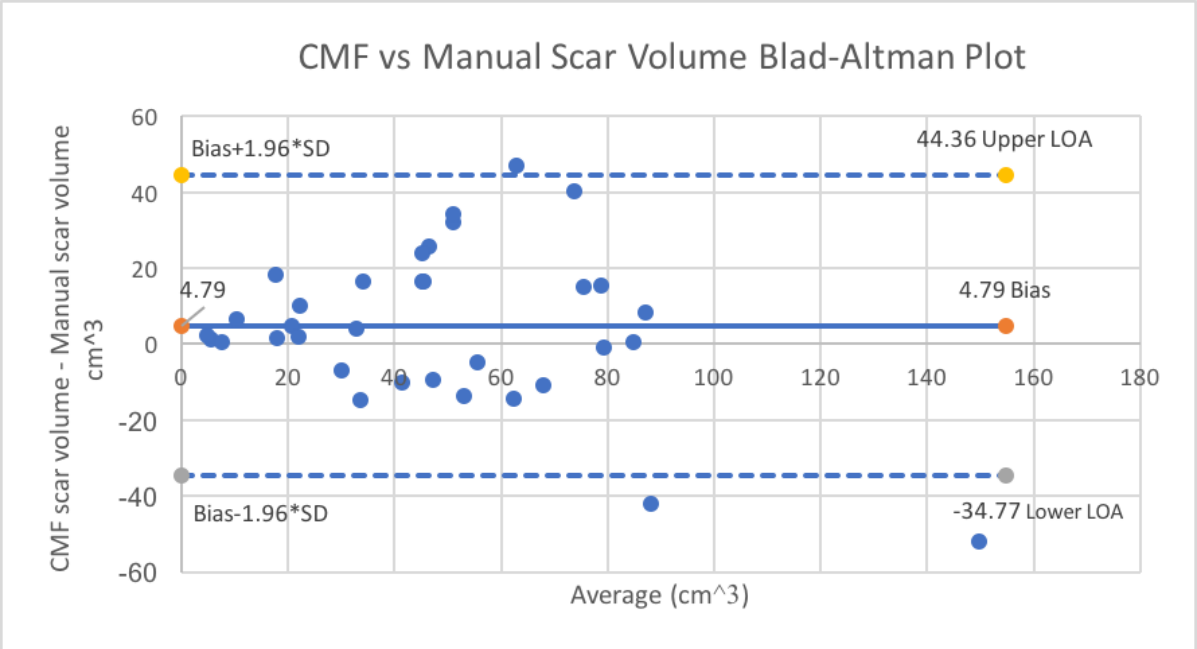

Figure 28: The scar volumes of CMF versus Manual Segmentation methods using Bland-Altman plots of scar volumes.

the CMF and FWHM methods, we accept the H_0, and we found that there is no significant difference ($p > 0.05$) between the algorithm scar segmentations and the manual

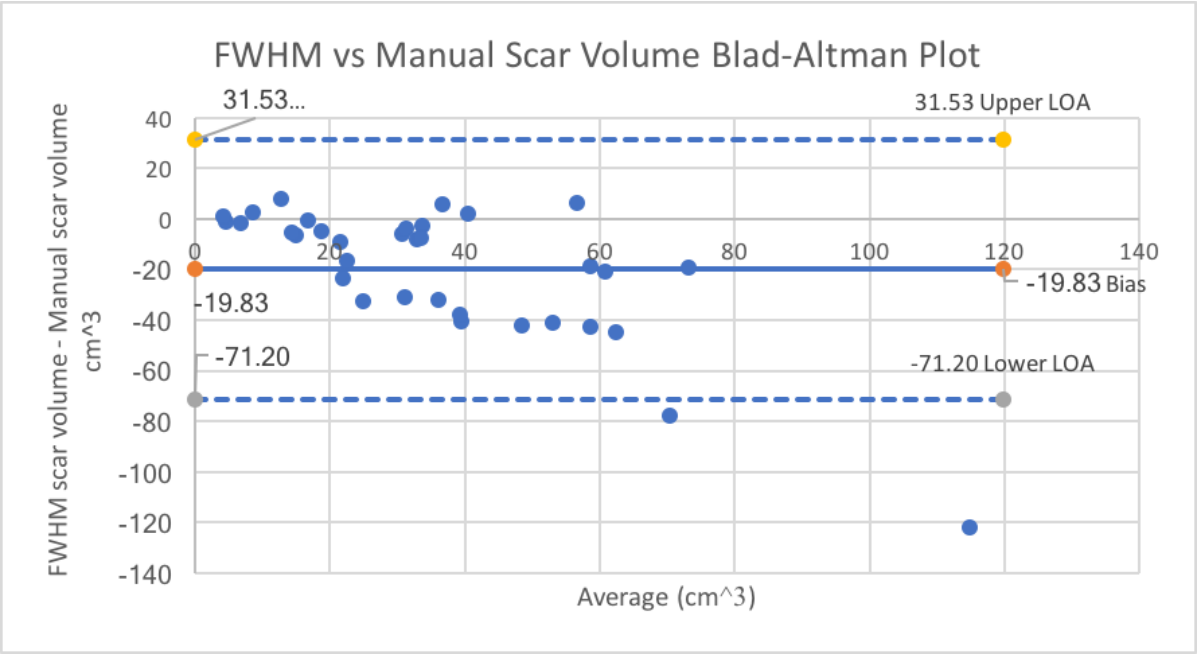

Figure 29: The scar volumes of FWHM versus Manual Segmentation methods using Bland-Altman plots.

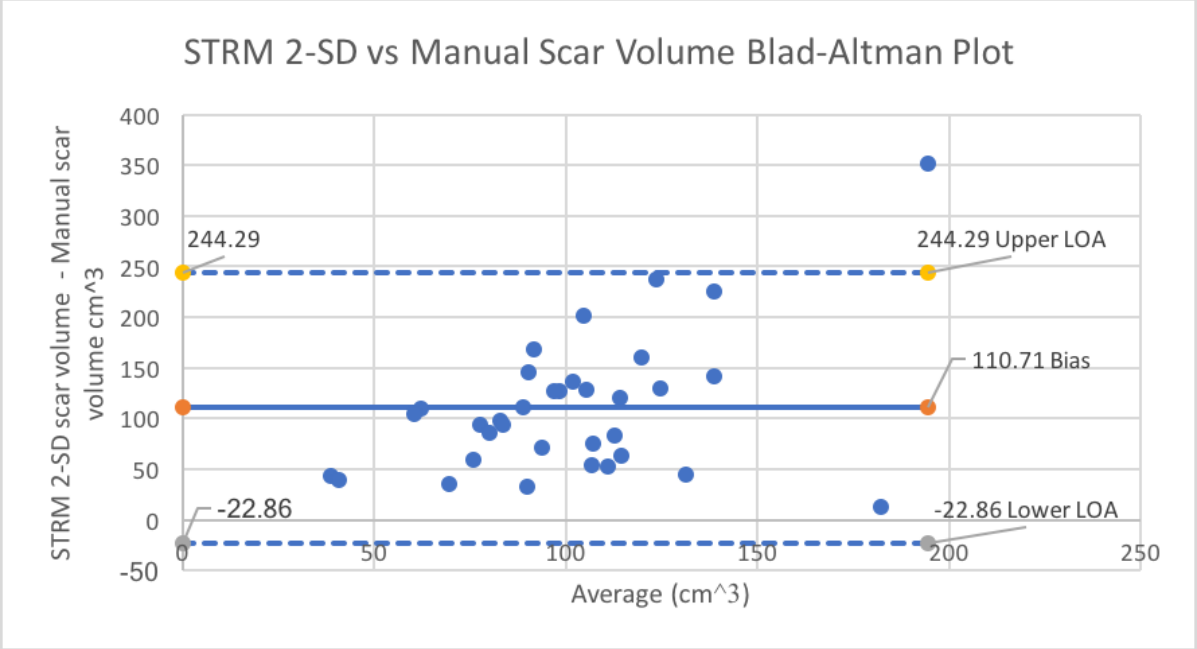

Figure 30: The scar volumes of STRM 2-SD versus Manual Segmentation methods using Bland-Altman plots.

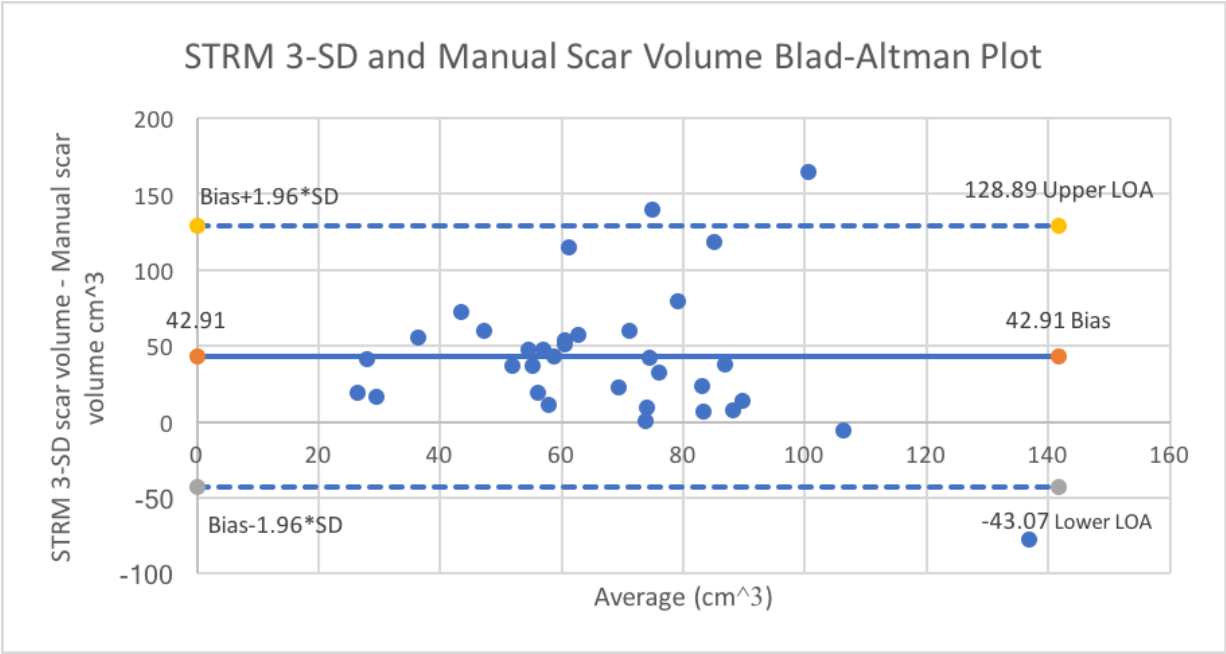

Figure 31: The scar volumes of STRM 3-SD versus Manual Segmentation methods using Bland-Altman plots.

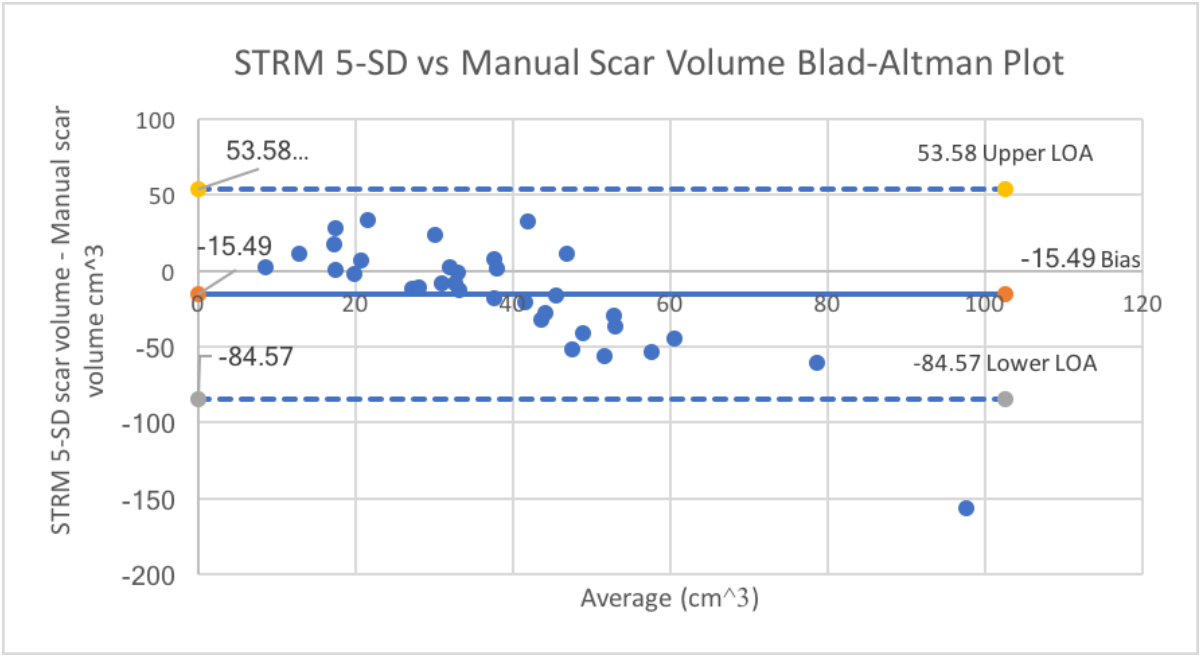

Figure 32: The scar volumes of STRM 5-SD versus Manual Segmentation methods using Bland-Altman plots.

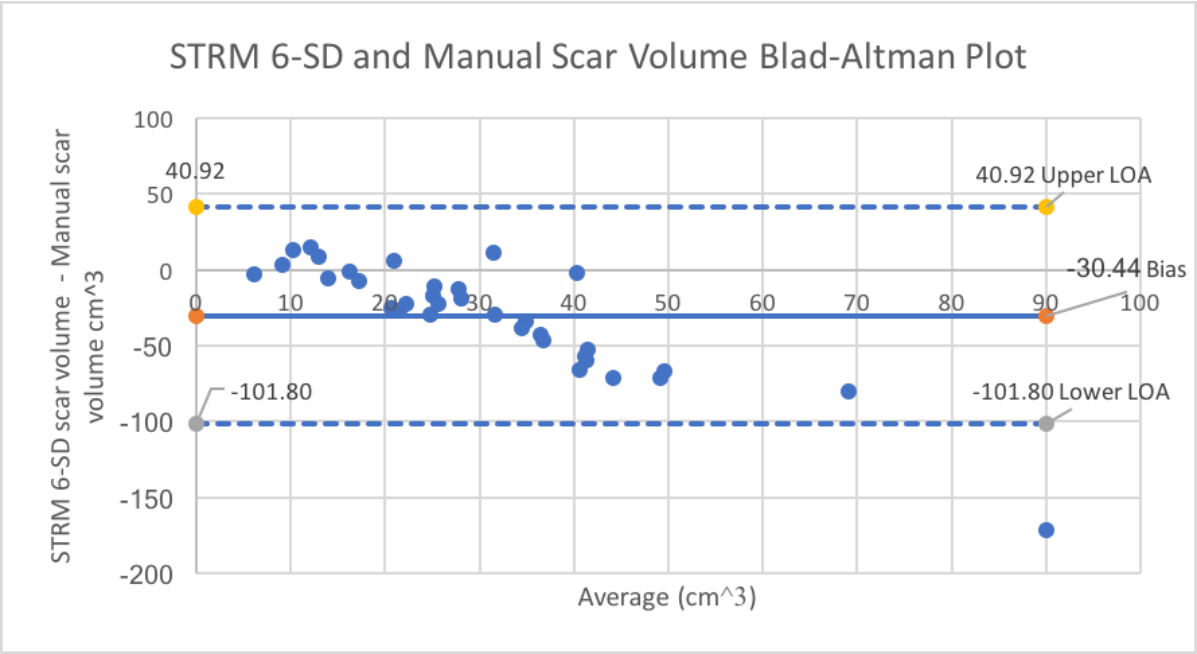

Figure 33: The scar volumes of STRM 6-SD versus Manual Segmentation methods using Bland-Altman plots.

scar segmentations. For all the STRM methods, the volumes of scar segmentations were significantly different from the manual scar segmentations. Figures 28 to 33 present the Bland-Altman plots from the scar volumes generated using the CMF, FWHM, and four different STRM methods named as STRM 2-SD, 3-SD, 5-SD, and 6-SD methods.

3.3.1 Inter and Intra-Observer Variability

Manual scar segmentation is prone to error and high variability. The variability between the scar volumes obtained from different observers is an indicator of subjectivity and different experience among different radiologists. It is important to quantitatively measure the variability of manual scar segmentations from different experts. Therefore, we calculated inter and intra-observer variabilities of manual scar segmentations. Figure 34 shows our results of the inter and intra-observer variability study of manually segmented scar volumes. For the study, we asked three different observers to segment the myocardial scar manually from a small subset of 3D LGE-MR images.

Table 6: Results of the Bland-Altman analysis for the compared methods. Bias, standard deviation, minimum, and maximum volume differences of different segmentation methods when compared to the manual segmentations.

	Bias	Standard Deviation	Minimum $[cm^3]$	Maximum $[cm^3]$
CMF	4.79*	20.19	4.705	149.695
FWHM	-19.83*	26.21	4.08	114.77
STRM 2-SD	110.71	68.15	38.59	194.37
STRM 3-SD	42.91	43.87	26.49	136.83
STRM 5-SD	-15.49*	35.24	8.56	97.58
STRM 6-SD	-30.44	36.41	6.19	90.06

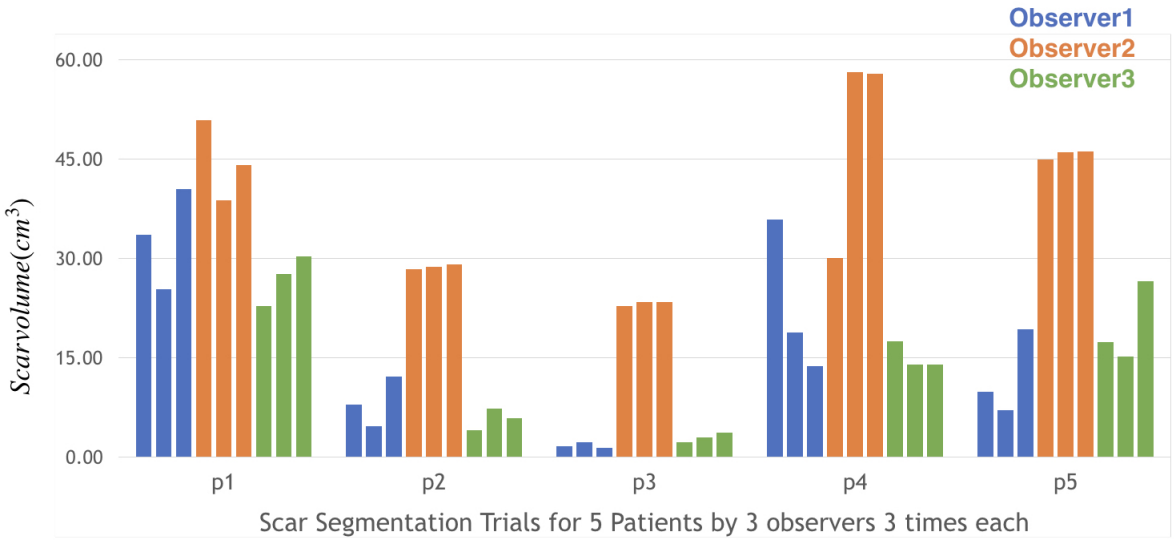

Figure 34: The inter and intra observer variability of manual scar segmentation volumes.

For the inter-observer variability analysis, each observer segmented the same subset of five images. For each patient image, the variability among the manual scar volumes by three different observers are compared. The same procedure is repeated for all observers. Table 7 shows the scar volumes of different segmentations from each observer. The p1 to p5 indicates the patient numbers as one to five. The scar segmentations from different

Table 7: Segmented scar volumes obtained from three different observers. Each observer manually segmented the scar three times which are reported as in 'repetition 1' to 'repetition 3' for five different patients, 'patient 1' to 'patient 5'.

		Observer1	Observer2	Observer3
patient 1	repetition 1	33.6279	50.8529	22.7734
	repetition 2	25.3388	38.8263	27.5859
	repetition 3	40.4676	44.0847	30.2981
patient 2	repetition 1	7.9666	28.3304	4.0351
	repetition 2	4.6556	28.7503	7.2622
	repetition 3	12.1982	29.0982	5.8241
patient 3	repetition 1	6.7570	22.7820	2.2669
	repetition 2	110.8164	23.4599	2.9864
	repetition 3	91.1894	23.3858	3.7532
patient 4	repetition 1	35.8597	30.0483	17.4236
	repetition 2	18.8556	58.0948	13.9318
	repetition 3	13.7409	57.9368	13.9770
patient 5	repetition 1	9.8058	44.9617	17.3162
	repetition 2	7.1074	46.0601	15.1808
	repetition 3	19.2768	46.1243	26.5654

observers were visualized in three different colors on the bars.

On the other hand, for the intra-observer variability analysis, each observer is asked to segment the five images repetitively three times. To overcome the memory bias, the repetitions of the image segmentation are performed on different days for the same patients. For each observer, the variability among the three different manual scar segmentations is compared for each scar volume. The same procedure is repeated for all observers. Figure 35 shows the results of inter and intra-observer variability of different scar segmentation volumes. The bar graph shows each observer in different colors. The consecutive unicolored bars indicate the repetitions of scar segmentations for each observer.

3.4 Contribution

In our 3D quantification of myocardial scar, we proposed to use a continuous max-flow based scar segmentation method. In our experiments, the CMF method outperformed other widely used th methods using several accuracy metrics. Using the CMF method, we segmented the myocardial scar tissue within the borders of the pre-segmented myocardium without any further user interactions. Six different scar segmentation methods were compared using six well-known comparison metrics including DSC, volume error, absolute volume error, normalized scar volume, precision, and recall, as well as using two statistical tests called the Bland-Altman plots, and the student t-test. The proposed CMF method yielded a mean DSC of $72.18 \pm 8.51\%$ in accuracy outperforming the most commonly used methods for scar segmentation including the FWHM and several STRM methods. Moreover, the CMF method outperformed other th methods in almost all presented metrics.

3.5 Discussion

Despite recent advancements in acquiring high-resolution 3D LGE-MR imaging, the transition of computerized methods for utilizing these images during relevant clinical procedures has been fairly slow. In order to fully benefit from the high-resolution 3D

LGE-MRI, robust and accurate scar segmentation techniques are highly desirable. In the scope of this thesis, we made efforts to quantitatively segment the myocardial scar from 3D LGE-MR images and to understand the differences in the reconstructed geometry of scar generated from 2D versus 3D LGE-MRI. However, due to the challenges in the nature of myocardial scar segmentation, there are several aspects of limitations in our thesis.

In this study, we described an algorithm for myocardial scar segmentation from 3D LGE-MR images. Our method is 3D and it is considered to be specifically useful in applications, such as computer simulations of cardiac electrophysiology [3]. One of the main limitations of our method is the dependence on the manually segmented myocardium. This requires an extensive amount of user time. For this study, we used the pre-segmented myocardium which was present for creating the 3D model of the heart for computer simulations of cardiac electrophysiology. As future work, we plan to utilize a multi-atlas-based algorithm or a machine learning algorithm for automated segmentation of the myocardium in 3D LGE-MR images prior to the scar segmentation.

3.5.1 Limitations of our 3D Scar Segmentation Study using the CMF Method (Chapter 3)

In the 3D scar segmentation study, we observed that the CMF method failed to exclude the false-positive scar structures for a number of patients. To determine the reasons for the failing cases, we analyzed our scar segmentation results from three patients which yielded the lowest DSC accuracy ($< 64\%$) by the CMF method. The underlying errors for the scar segmentation were mainly due to the errors in manual myocardium segmentations. In Figure 35, the largest regional overlap errors produced by the CMF method can be seen. For one patient, the CMF method yielded the lowest DSC value of 47.9%. For this specific case (Figure 35 (Case1)), the CMF algorithm over-segmented the scar on the left ventricle. For the second case (DSC of 56.62%), the scar was very small in size (Figure 35 (Case2)) in respect to the size of the myocardium. Due to a limitation of the

DSC overlap metric, the DSC value is biased towards the size of the scar. For small scar structures, the DSC metric may yield lower accuracy results than usual despite the high visual agreement between the CMF and manual scar segmentations. For the final case (DSC of 57.01%), the CMF method mislabeled the part of the blood pool as the scar (Figure 35 (Case3)) in the left ventricle due to the errors in the manual myocardium segmentation. The manual myocardium segmentation mistakenly included the blood pool in the myocardium region. On the other hand, the observer was able to distinguish the error in the myocardium segmentation towards the blood pool and excluded the region from the manual scar segmentation.

In our study, one single expert observer created the manual scar and myocardium segmentations. There was a lack of consensus ground truth for evaluating the algorithm results. To overcome this limitation, a consensus ground truth utilizing combinations of independent expert segmentations can be created for future studies. However, the inter and intra-observer variability of the segmentation results remain a problem for any manual segmentation. This feature propagates through the learning stage of scar segmentation algorithms as well.

Another problem was the relativity of the gadolinium absorption on LGE-MR images for different patients. The gadolinium absorption mechanism is relative to patients' age, metabolism, heart rate, and several other patient differences. Absorption of gadolinium by scarred myocardium areas affects the brightness of LGE-MR images. Therefore, scar analysis is relative by nature due to gadolinium kinetics of LGE-MR imaging technique.

For validation, we compared our method against basic th methods such as the FWHM and the STRM methods due to the simplicity of their implementation. For validating the CMF method, different advanced methods such as level sets, hierarchical max-flow (HMF) [82], or active contours methods need to be compared against the CMF method.

The lack of publicly available dataset was a problem for evaluating our algorithms. This common data should represent a big patient population and should be in varying image qualities. Algorithms are highly affected by the image quality, resolution, vendor

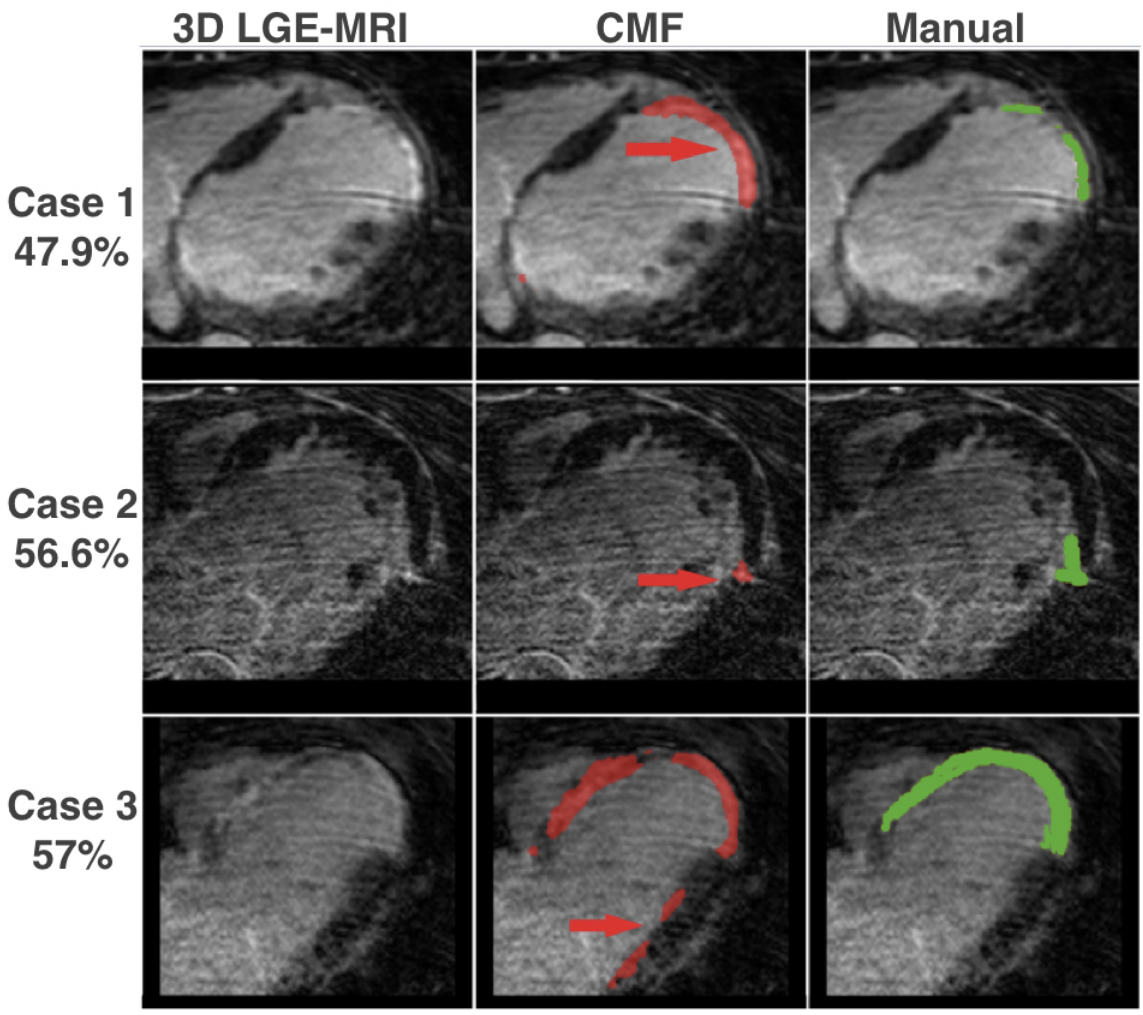

Figure 35: Three patient images which the CMF method performed poorly (in DSC) in the scar segmentation.

and center differences of data. It means that a large amount of data needs to be obtained from different imaging centers (multi-center), using different MRI devices (multi-vendor) with different acquisition parameters. In the study, the CMF method was evaluated using thirty-four 3D LGE-MR images. For the future studies, a larger and more diverse dataset containing multi-center and multi-vendor data with varying image qualities need to be utilized.

The CMF method has several advantages when it is compared to previous scar segmentation methods. For instance, the CMF method is capable of segmenting the scar

from 3D LGE-MRI as opposed to many scar segmentation methods from 2D LGE-MRI. Another advantage of the CMF method is its computational time. Using the CMF method, the scar from a 3D LGE-MR image can be segmented in around 1.8 seconds when the manually segmented myocardium is given. The basic th methods are prone to error since they utilize only the signal intensity of images. On the other hand, the CMF method incorporates neighborhood and shape constraints into the segmentation, as well as the signal intensities of an image dataset.

3.5.2 Atlas-based Myocardial Segmentation

One of the main limitations of our method was the dependency on the manual pre-segmented myocardium to limit the region of interest for the scar. The manual myocardium segmentations required an extensive amount of user time before the scar analysis as well as yielding segmentation errors in the myocardium as mentioned in the paragraph above. As future work, one can utilize an atlas-based segmentation method or a machine learning method for automatically segmenting the myocardium from 3D LGE-MR images.

We tried a preliminary approach for obtaining the myocardium boundaries. We utilized an atlas-based segmentation method called multi-atlas based joint label fusion (JLF) [113] method. Atlas methods are suitable for segmenting organs and structures with a fixed shape such as skull, lung, or myocardium of the heart. Atlas method uses manual myocardium segmentations from different patients to create an average model atlas of the myocardium. This method uses a majority voting technique [114, 115] for segmentation. Taking the model atlas as a reference, the JLF creates a segmentation similar to the segmentation of the atlas myocardium based on the similarity of the new image to the reference atlas image. Using these steps, we segmented the myocardium of twenty-four patients from the 3D MRA images. We obtained high accuracy (a DSC of 75%) in myocardium segmentation when compared to the manual myocardium segmentations.

For this method, we utilized 3D magnetic resonance images (MRA) from twenty-four

patients to distinguish the myocardial boundaries. Distinguishing myocardial boundaries from the LGE-MRI is prone to error due to the presence of a scar on the LGE-MRI. The MRA images are, on the other hand, the type of MRI which highlights the blood pool and the heart anatomy can be easily distinguished. The MRA images are acquired along with but before the LGE-MR images are acquired. Shortly after the injection, the gadolinium reaches to the blood pool by the blood circulation. The gadolinium hyper-enhances the blood pool and the anatomical structures of the heart can be observed clearly. The LGE-MR images are acquired about 10 to 15 minutes apart from the MRA acquisitions while the patient is still lying in the scanner. Since MRA images are acquired along with the LGE-MRI for each patient, they are in the same spatial alignment with the LGE images. Many algorithms utilizing the image intensity tend to fail to distinguish the myocardium from the other structures using LGE-MRI due to the high intensity of the scarred region which attracts segmentation boundaries. For each patient, we had both LGE-MR and their spatially aligned pairs of MRA images in our dataset. Due to the good spatial alignment between the MRA and LGE, myocardium segmentations from the MRA images can be used for limiting the region-of-interest from the LGE-MR images.

For this purpose, we first randomly selected ten 3D MRA and corresponding LGE images for creating the model atlas for the atlas-based segmentation method. These ten MRA images were acquired from different patients. Therefore, they had differences in the heart geometry, shape, spatial alignment, patient position, size of the heart, and the different signal intensity ranges due to different settings of the MR acquisitions for each patient. To account for these variations in the dataset, we first normalized the signal intensities using a linear normalization method. Afterward, to bring the images into the same spatial alignment, we used a pipeline of rigid, affine, and non-rigid registration technique [116, 117]. We selected one image randomly as a reference heart and registered other images into the spatial space of this image.

In order to accelerate the registration, we first used some pre-processing steps for

centering the images prior to registering all other nine images into the reference heart. We automatically found the center of each 3D myocardium from the image labels. We, then, registered all nine images into the reference image space rigidly [118], affinely [118] , and non-rigidly [119]. The rigid registration performed the rotation and translation of the images and the affine registration scaled the myocardium region by shrinking or expanding the myocardium of the different sized patient hearts. Finally, the non-rigid registration warped the 3D LGE-MRI to exactly match the geometries of the nine images into the geometry of the reference image. After the registration, we saved the registration maps which were the transformation matrices. We applied these resulted registration maps into the myocardium segmentations. Finally, using the ten spatially registered MRA images, we created an average heart model or so-called 'atlas' as well as the label of this atlas from the MRA images. After creating the atlas once, we then used the JLF method to segment the myocardium from a dataset of twenty-four MRA images which were not used for creating the atlas.

Since we only created the myocardium segmentations for the MRA images, we registered our spatially aligned MRA images into the LGE-MRI spaces non-rigidly. Using this registration map, we obtained the myocardium segmentations for the LGE-MR images. We had a good visual agreement between the manual expert myocardium segmentations and the automated atlas segmentations. Our atlas segmentation method yielded a DSC of 75% overlap accuracy. However, after using the atlas myocardium as a mask prior to the scar segmentations, the scar segmentation accuracy dropped to a DSC of 40% from a DSC of 72% using the CMF method. Therefore, we did not include the atlas method in our proposed scar segmentation pipeline. Although providing a promising manual segmentation result, the atlas method failed in the unclear endocardial boundaries which led to errors in the scar segmentations afterward. Some scar segmentation results using the manually segmented myocardium and the atlas resulted myocardium can be seen in Figure 36. Due to the computational complexity of the atlas method, we only tested this method on twenty-four randomly selected MRA images out of thirty-four patients.

3.6 Summary

In this chapter, we developed an approach to segment the myocardial scar from 3D LGE-MR images using the CMF method. The data term comprised of a distribution matching term for scar and normal myocardium and a boundary smoothness term for the scar boundaries were used. The region-of-interest for the scar segmentation was constrained using a manually segmented myocardium. We evaluated our CMF method for accuracy by comparing it to manual scar delineations from the 3D LGE-MR images of thirty-four patients. We compared the results of the CMF technique to the ones by conventional FWHM and STRM methods. The CMF method yielded a DSC of 72±18% and an absolute volume error ($|VE|$) of 15.42±14.1 cm^3. Overall, the CMF method outperformed the conventional methods for all reported metrics in 3D scar segmentation except for the recall value. Among the STRM methods, the STRM 5-SD method yielded the highest DSC accuracy and lowest $|VE|$. Figure 36 shows the myocardium and the scar segmentations using the manual versus atlas myocardium as a prerequisite to the scar segmentations generated using manual, CMF, FWHM and the STRM methods.

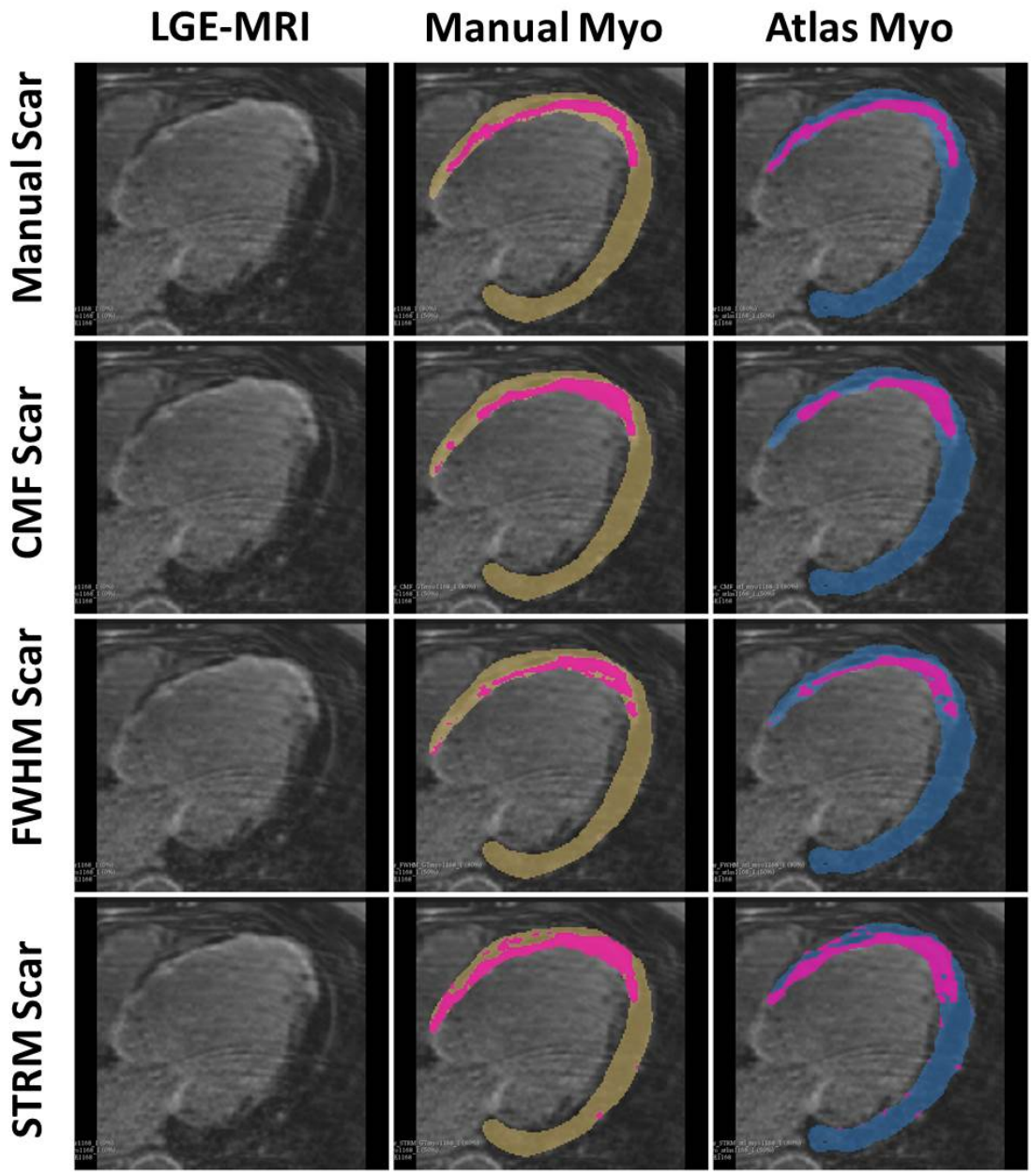

Figure 36: Atlas myocardium and scar segmentation results on axial slice views. The first column is the single slice from an LGE-MR image. The second Column shows manual expert segmentation (in yellow) of the myocardium. The third Column shows the myocardium segmentation (in blue) using the atlas method. Rows (1-4) present the scar segmentation results (in pink). From top to bottom; manual, CMF, FWHM and STRM scar segmentation results given either expert (yellow) or atlas (blue) segmented myocardium.

4

Shape Comparison Study of Manual Scar Segmentations Generated using 2D versus 3D LGE-MRI

Myocardial scar geometry may influence the sensitivity of risk prediction for VT since outcomes of VT simulations are greatly dependent on scar geometry obtained using LGE-MR images [49]. To obtain the 3D scar geometry, scar segmentations generated using 2D or 3D LGE-MR images can be used. Based on the preferred image acquisition, the scar segmentation will differ in terms of scar volume, scar mass, and shape. Previous studies compared the signal to noise ratio (SNR) [83], scar volume, scar mass [53], and image acquisition time [53] between the 2D and 3D LGE-MR images. However, the differences in the scar geometry remained unexplored.

To explore the similarities and differences in the reconstructed geometry of scar from 2D and 3D LGE-MRI, we conduct a manual scar segmentation study. For the study, a retrospectively-acquired dataset of twenty-four patients with myocardial scar underwent both 2D and 3D LGE-MR imaging. First of all, manual scar segmentations are performed for the 2D and 3D datasets individually using a multi-planar image processing software. Second, from the 2D scar segmentation boundaries, 3D scar surfaces are reconstructed using a logarithm of odds (logOdds) based interpolation method. On the other hand, the scar geometries obtained from 3D LGE-MRI are used as is without a need for reconstruction due to the high out-of-plane resolution of 3D images. Finally, we compare the 3D models of scar generated from 2D and 3D LGE-MR images using several shape and volume metrics such as fractal dimensions, number of connected components, mean scar volume, and normalized scar volume. We also provide statistical analysis for scar and myocardium volumes using Bland-Altman plots, Pearson correlation and coefficient plots, and student t-test.

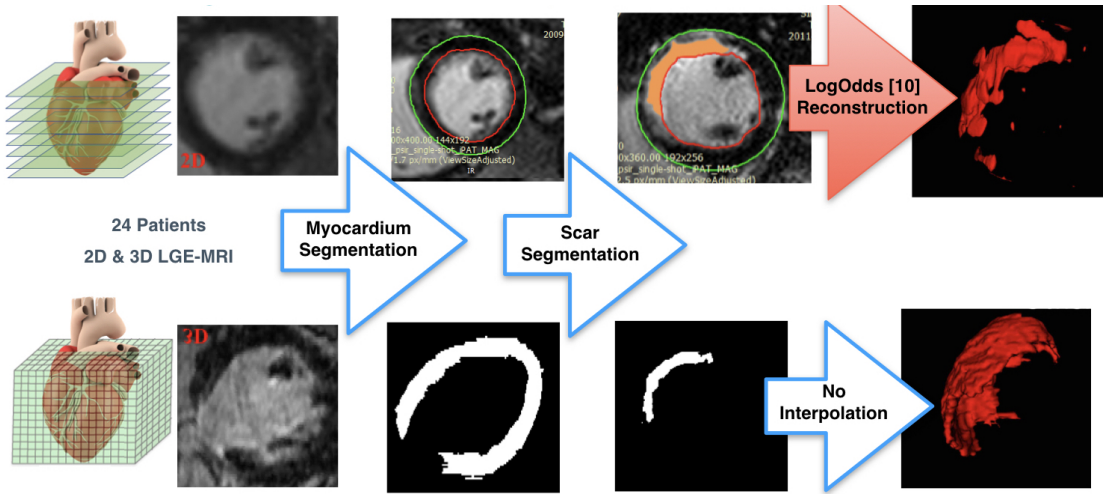

Figure 37: Block diagram for the comparison study using 2D and 3D LGE-MRI.

4.1 Background

The differences in myocardial scar geometry substantially affect the clinical outcomes of cardiac simulations of VT [48]. Previous studies although comparing the 2D and

3D LGE-MRI in regards to several cardiac metrics such as scar volume [53], scar mass [53], SNR [83], and image acquisition times [53], they have not explored the differences in shape of reconstructed scar geometries. Therefore, a comparison study of scar geometries using 2D versus 3D LGE-MRI is highly desirable.

Currently, multi-slice 2D LGE-MRI is the clinical standard for segmenting the myocardial scar, which acquires transverse slices with anisotropic dimensions [51]. However, reconstructing a 3D model of the scar from 2D LGE-MR images is problematic due to the anisotropic pixel dimensions in 2D LGE-MR images. However, through the advancements in MRI technology, we can now acquire 3D LGE-MR images to capture a high-resolution and isotropic representation of myocardial scar. The 3D LGE-MRI is suitable for applications requiring reconstructing the intact scar geometry, as it is isotropic in voxel dimensions and have a higher resolution [52].

In this study, our objective is to compare the scar geometries generated from high-resolution 3D LGE-MRI to that generated from conventional multi-slice 2D LGE-MR images. To this end, we first obtain manual expert delineations of scar regions from 2D multi-slice LGE-MR and 3D LGE-MR images of each of the twenty-four patients. We reconstruct a 3D model of the scar structure from scar segmentations generated using the 2D multi-slice LGE-MRI using a reconstruction method called logOdds[52]. We then compare the 3D scar geometries generated from 2D and 3D LGE-MR images using different metrics based on scar geometry and volume. This study is the first attempt at understanding the similarities and differences between the shape of scar geometries obtained using 2D and 3D LGE-MRI. Figure 37 presents the block diagram of our comparison study. On the left, steps for the 2D manual scar segmentation and reconstruction of scar geometries can be seen. Steps 1 and 2 are similar for the 2D and 3D manual scar segmentations. In step 3, the reconstruction of 2D scar segmentations to 3D scar geometries was performed using the logOdds method. For the 3D, the scar geometries were used as is without the reconstruction required (step 3, right column).

4.2 Methods

4.2.1 Image Dataset

For comparing the scar geometries obtained from 2D vs 3D LGE-MRI, we used two separate image datasets which were acquired simultaneously from a Siemens Trio 3T MRI scanner for twenty-four patients. All patients presented left ventricular scar and underwent both 2D and 3D imaging exams. The 2D LGE-MRI dataset is highly anisotropic with around 1.875x1.875 mm^2 inner-plane and 8 mm out-of-plane resolution. These 2D-multi slice images contain 8 to 12 slices in short-axis (SAX) view. The 3D dataset, on the other hand, is isotropic and has voxel dimensions around 1.3x1.3x1.3 mm^3 in any given plane. The number of SAX slices for the 3D LGE-MR dataset is around 84 $\pm$ 13 (mean and standard deviation) along the long-axis (LAX). The 2D and 3D dataset contained thirty-five patients, while some of the 2D image acquisitions were missing slice locations along the LAX. Therefore, we were able to include only twenty-four 2D and 3D image pairs in the study, while the remaining images were excluded due to the incompleteness of the image locations.

Figure 38 shows the visual representation of 2D and 3D imaging of the heart models. While 2D multi-slice images have thick and anisotropic image slices (8 mm along the LAX), the 3D LGE-MRI can image the heart using over 100 slices along the LAX. The 3D provides high-resolution images of the heart from any axis. Figure 39 indicates the resolution differences between 2D and 3D LGE-MR images from three different patient images. In the 3D LGE-MR images (right column), both image resolution and scar contrast are superior to the 2D LGE-MRI (left column).

4.2.2 Manual Scar Segmentation from 2D LGE-MRI

For the comparison study, the first step was to segment the myocardial scar in both 2D and 3D LGE-MR images. For the 2D LGE-MR dataset, we manually traced the boundaries of the endocardium and epicardium using CVI42, a commercially available software

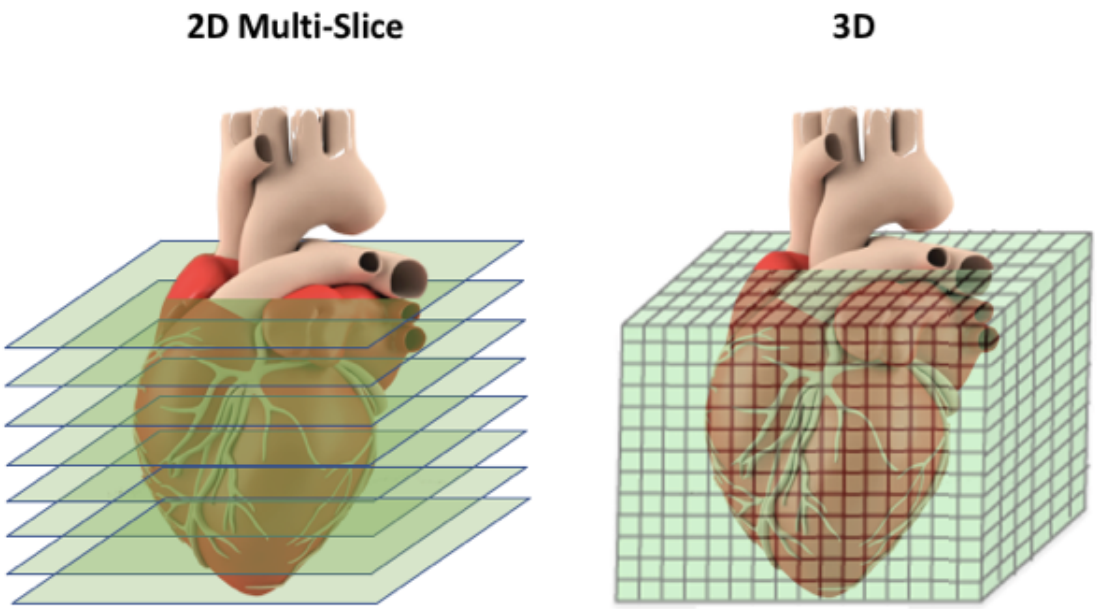

Figure 38: 2D versus 3D LGE-MRI for imaging the full-heart. 2D MR image model on the left uses only 8 slices from consecutive locations of the heart. On the right, the high-resolution 3D LGE-MRI represents the heart as a volume using many slices. In a real LGE-MR image, 3D will have more slices than it appears on the image.

for cardiac image processing. Using the pre-segmented endocardium and epicardium as boundaries of our region of interest, we then segmented the myocardial scar using the full-width-at-half-maximum (FWHM) method in 2D LGE-MRI. The FWHM considers the voxels as scar if the intensities are greater than the half of the maximum intensity within the region of interest, myocardium. The scar segmentations by the FWHM method was then manually inspected and corrected using the CVI42. After the myocardium was segmented, ITK-Snap [120], a multi-planar reformatting software platform was used to interactively correct the FWHM scar segmentations from the 2D LGE-MR images using a brush tool. After the manual corrections, the 2D scar segmentations were finally reconstructed to 3D volumes for comparing the 2D scar geometries against the 3D scar geometries from 3D LGE-MRI.

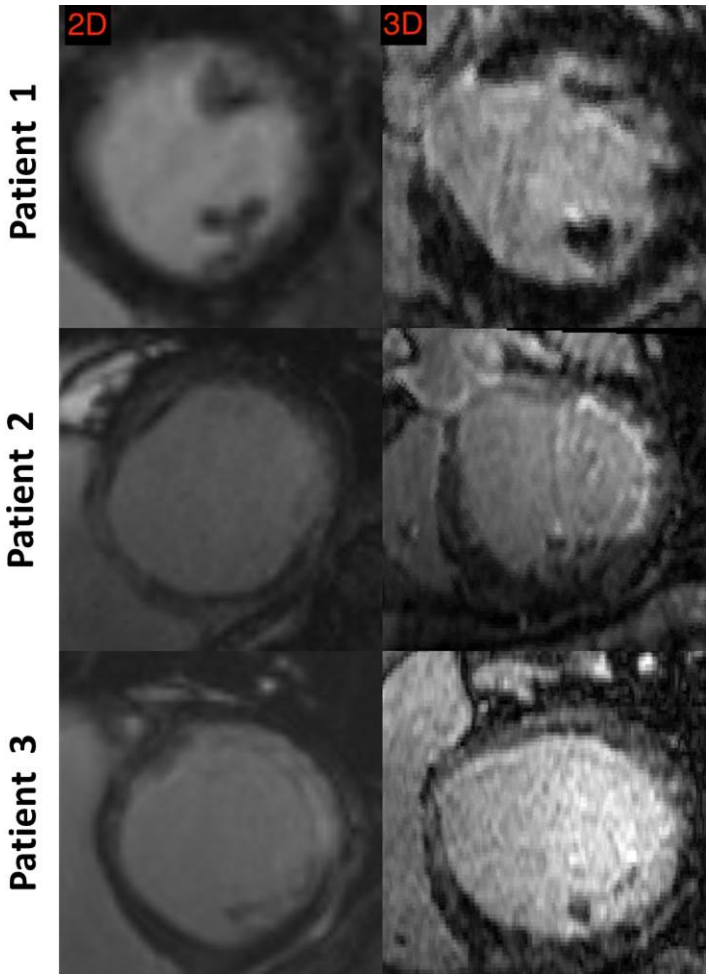

Figure 39: Comparison of single slice views from 2D (left column) and 3D (right column) LGE-MR images of three different patients (three rows). The 2D and 3D images approximately represent the same cardiac location. The resolution difference even in the SAX view can be seen from the single slice SAX view of 2D and 3D LGE-MR images. The 2D LGE-MRI has lower resolution due to the partial volume effect.

4.2.3 Reconstruction of Myocardial Scar Geometry from 2D LGE-MRI

For comparing the 3D geometries of myocardial scar, we reconstructed 3D scar models from the 2D manual scar segmentations. We used a logarithm of odds (logOdds) [121] based reconstruction method for the task. The logOdds is a reconstruction method for creating 3D geometries from 2D image slices[121]. The logOdds method outperformed the nearest neighbor and other well-known reconstruction methods in the reconstruction

of scar geometries in terms of region overlap [48]. Using the logOdds method, a 3D model of the scar was created from only 8 to 12 slices of 2D delineations.

The logOdds method maps a space of probabilities into a Euclidean space to estimate a 3D model from 2D data. A logOdds function allows many linear combinations in its vector space and is not restricted to only convex space usage of binary labels. As seen in the equation below, *logit* is referring to the *logOdds* algorithm, and p is the probability of an anatomical shape to be assigned to a voxel. The $logit(p)$ is the logarithm of odds between p and the complement of p for reconstructing the 3D scar surfaces from the 2D scar segmentations.

$$logit(p) = log\frac{p}{1-p} \tag{17}$$

4.2.4 Manual Scar Segmentation from 3D LGE-MRI

For creating 3D scar models from 3D-LGE MR images, we first obtained the myocardial segmentations on 3D LGE-MRI dataset. Since it is impractical to segment the myocardial boundaries manually on 3D LGE-MRI, an interactive 3D segmentation method [33, 82] was utilized to extract the myocardium region semi-automatically. After obtaining the myocardium segmentations semi-automatically for each patient, we performed manual refinements and obtained the expert segmentations of the myocardium as the region of interest to our 3D scar segmentations [82]. Next, we segmented the myocardial scar manually from the 3D LGE-MRI using the 3D brush tool on the ITK-Snap software. The 3D LGE-MR images contained around 84±13 (minimum 62 and maximum 123 image slices) SAX image slices along the long-axis (LAX). Since 3D LGE-MRI is isotropic in any given dimension, we did not require the reconstruction step for the 3D dataset. Therefore, after creating the manual scar delineations on 3D LGE-MRI, we kept these 3D scar segmentations as is without applying the logOdds algorithm to 3D scar segmentations.

4.3 Metrics Based on Scar Geometry

After obtaining the 3D models of the scar manually from 2D and 3D LGE-MRI, we compared these scar geometries according to the scar shape and volume. For this, we used two different shape descriptor metrics: fractal dimensions, and the number of connected components. We also used scar volume metrics which compare the mean value of scar volumes and normalized scar volumes generated from 2D-reconstructed and 3D LGE-MRI.

4.3.1 Number of Disconnected Components

Connected components analysis is a basic yet useful image processing technique. In a given binary image, the connected component labeling counts the number of disconnected regions present in an image. It considers objects within a set distance of neighborhood as part of the same object and further components as different objects. It can label each object with a different incrementing number, and stores any equivalent labels in an equivalence table. The highest number of labels gives us the number of connected components in an image. The adjacency rule can be changed as either 4, 8 or more pixels/voxels around an object.

We compared the surfaces of scar segmentation results by calculating the number of connected components. The results were interpreted based on the number of disconnected scar regions. If the number of connected components was high, it showed that the scar segmentation contained several partitions of the scar. otherwise, the scar was a continuous and an intact surface.

4.3.2 Fractal Dimensions

Integer dimension values are insufficient to describe the shape of complex objects. On the other hand, the fractal dimension (FD) is a measure of complexity which can describe the dimensionality of an object with real numbers. The FD is positively correlated with

the complexity of a self-similar object. Given a 3D scar surface, the range of the FD can take any value between one and three depending on the complexity of the scar surface. An FD value of one means that the shape of the scar is simple, and the FD value of three means the shape of the scar is more complex. Therefore, the FD calculation is a compelling and a useful measure for comparing the shape scar geometries obtained from 2D versus 3D LGE-MRI.

The box-counting or in our case the 'voxel counting' method can be used to calculate the FD of a 3D volumetric binary image. The FD of a 3D object can be calculated by counting the number of self-similar-cubes $N(s)$, and the magnification factor N. Finally, the FD can be measured by dividing the logarithm of N(s) by the logarithm of N as following;

$$\frac{log(\text{number of self-similar pieces})}{log(\text{magnification factor})} = \frac{log(N(s))}{log(N)} \tag{18}$$

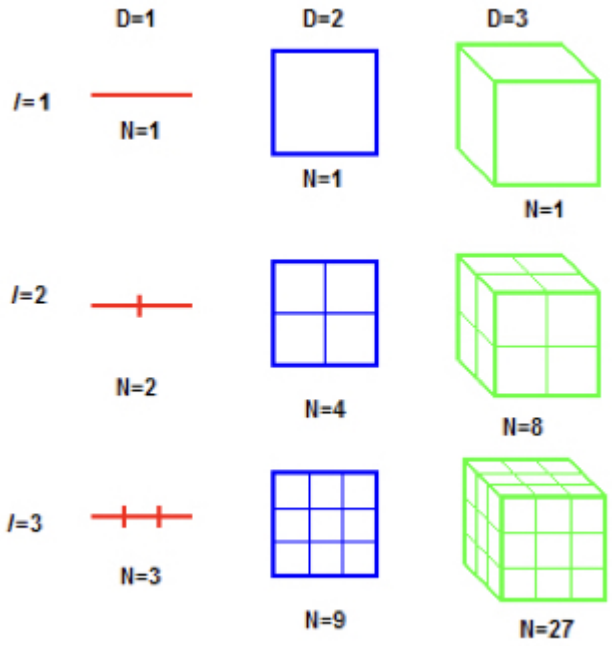

Figure 40: Magnification factor (N) for 1, 2 and 3 dimensional objects.

The magnification factor N can be calculated using the following approach. If a

one-dimensional line can be broken into 2 self-similar objects with the same length, the magnification factor is 2. Similarly, if we magnify these broken self-similar objects twice back to the original size, we obtain the same size as the original line. Different than the line, a square can be divided into 4 sub-similar squares with a magnification factor of 2. Therefore, for a square, the number of self-similar objects is N^2 while the magnification factor is N. Likewise, for a cube, the number of self-similar objects is N^3 while the magnification factor is N. Using the number of self-similar objects and the magnification factor, we can simply calculate the FD of a 3D scar surface. As an example of calculating the FD of a 3D scar volume, let us consider a 3D binary segmentation. If we consider all the voxels of that 3D image carry the value of 1, the number of self-similar objects, or voxels having the value of 1, will be N^3. Then, the FD becomes $FD = log(N^3)/log(N) = 3$. Therefore, the FD of a 3D scar volume will yield to a maximum value of 3 and a minimum value of 1.

4.4 Results

Reconstructed scar geometries from 2D LGE-MR images were compared to the scar geometries generated using 3D LGE-MR images using the two shape descriptor metrics and a volume metric. Figure 41 shows the 3D scar geometries obtained from 2D and 3D LGE-MRI. We used cubic LogOdds [52] and standard nearest neighbor (NN) reconstruction methods. The NN method sets the slice spacing to ten and yields an elevated reconstruction. On the other hand, the cubic logOdds method yields a smoother scar surface due to its reconstruction algorithm. Table 8 presents some quantitative results. We observed the varying size of scar for different patients. Therefore, besides reporting the mean and variation of scar and myocardium volumes from 2D and 3D LGE-MRI, we also found it appropriate to utilize the Pearson correlation coefficient plots for the 2D and 3D scar volumes. Figure 42 shows the different size of the scar tissue among different patients.

The mean fractal dimension was 1.84±0.18 and 2.2±0.12 (out of three) for 3D scar

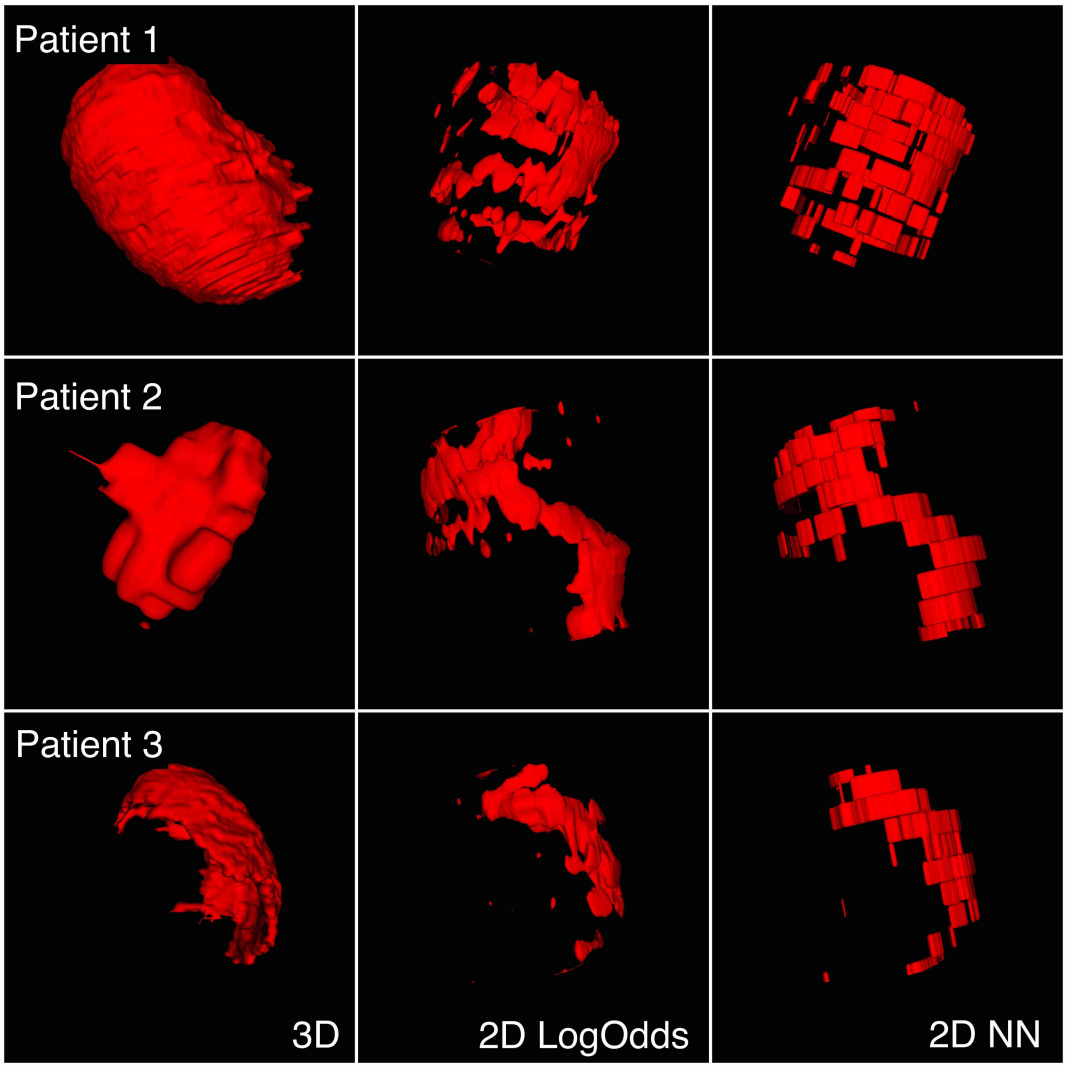

Figure 41: Scar geometries of two different patients (two rows) using 3D LGE-MRI (left column) and 2D LGE-MRI (other two columns) are seen. The 2D scar segmentations are reconstructed using two different reconstruction methods, namely, cubic LogOdds (middle column), and standard nearest neighbor (right column).

geometries generated using 2D and 3D LGE-MR images, respectively. This result indicates that the scar geometries generated using 3D LGE-MR images, as compared to the ones generated from 2D LGE-MR images, are more detailed in shape. We removed two outliers from the 3D dataset due to the uncommonly high connected component values. We observed more discontinuity in the shape of the 2D-reconstructed scar surfaces

Table 8: Comparison of 2D and 3D scar geometries using shape and volume metrics.

Metrics	3D	2D-logOdds	2D-NN
Fractal Dimensions [1-3]	2.2±0.12	1.84±0.18	2±0.09
Number of Connected Components [count]	4.33±3.3	6.29±3.9	22.4±10.6
Mean Absolute Volume [cm^3]	27.1±21.5	20.8±12.14	22.04±13
Normalized Scar Volume [%]	11.25±7.10	17.89±9.80	19.05±11

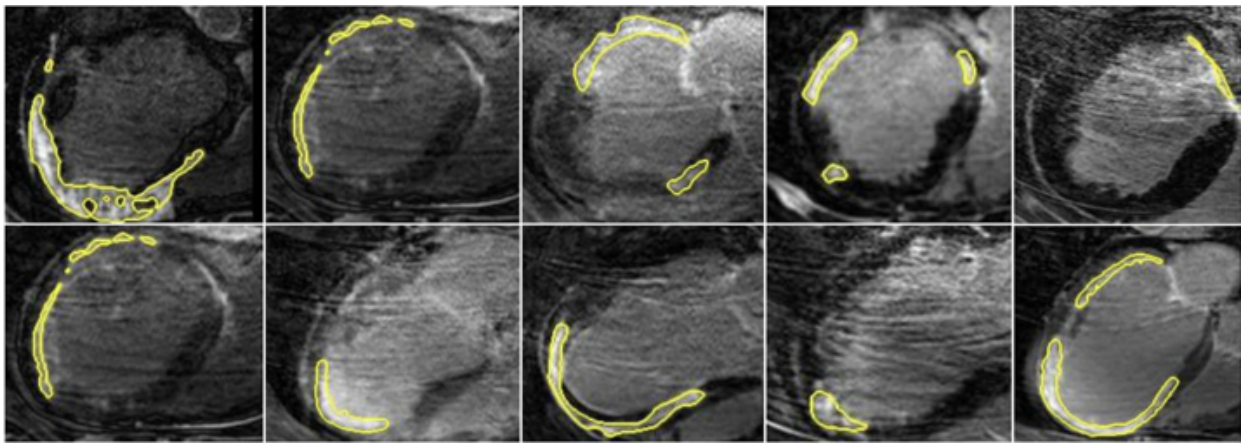

Figure 42: Varying size of scar from different patients in our dataset. Yellow contours represent the scar boundaries obtained using 3D LGE-MR images. Only single slices are shown in the images.

than the 3D. The 2D-reconstructed scar model contained more disconnected scar regions (6.29±3.9) than the 3D model (4.33±3.3). Finally, the 3D LGE-MRI produced higher mean scar volume of 27.1±21.5 cm^3 than the 2D LGE-MRI, 20.8±12.14 cm^3.

4.4.1 Statistical Analysis

We provide statistical analysis for comparing the scar geometries from 2D and 3D LGE-MRI based on surface overlap and scar volumes. The statistical comparison was performed using Pearson's correlation coefficient plots, Bland-Altman plots, and paired t-tests. We created Pearson's correlation and coefficient plots between the generated scar and myocardium volumes using 2D and 3D LGE-MRI. Figures 43 and 44 indicate that

there is a positive correlation between the scar volumes (r = 0.593) of 2D and 3D as well as the myocardial volumes (r = 0.77) obtained from 2D and 3D LGE-MRI, respectively. For the volume values for each patient, readers are referred to the Appendix of this thesis.

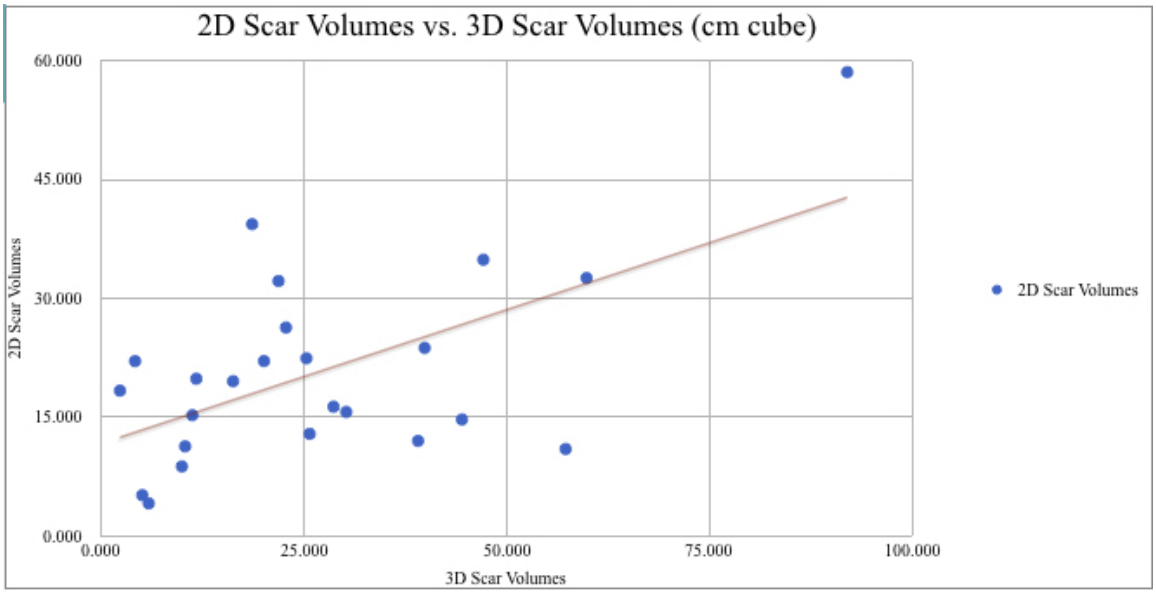

Figure 43: Correlation coefficient plot for the scar volumes of using 2D and 3D LGE-MRI.

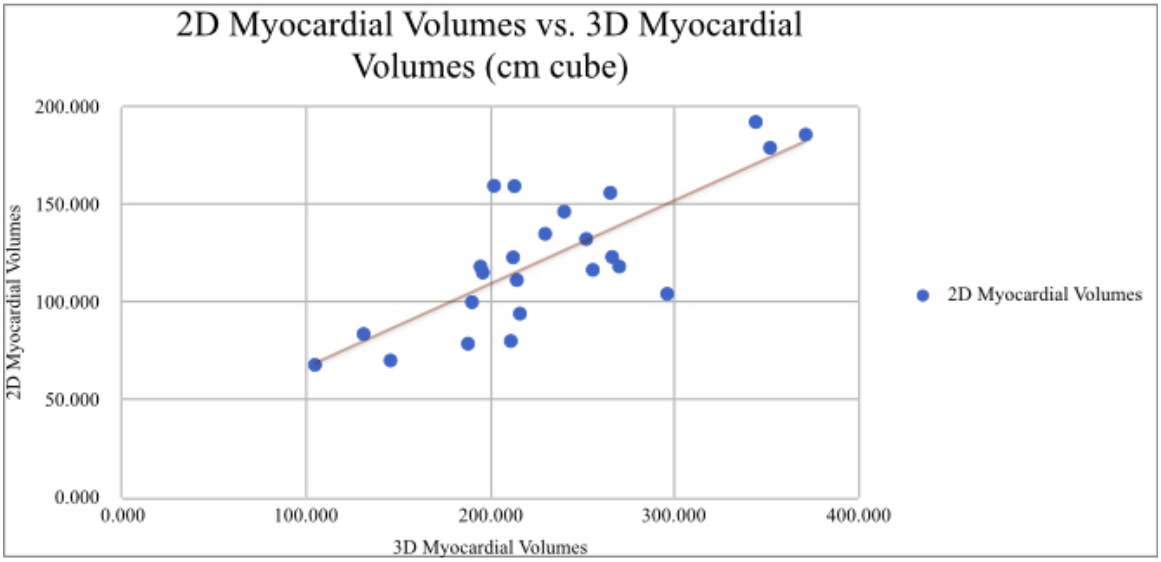

Figure 44: Correlation coefficient plot for the myocardium volumes of using 2D and 3D LGE-MRI.

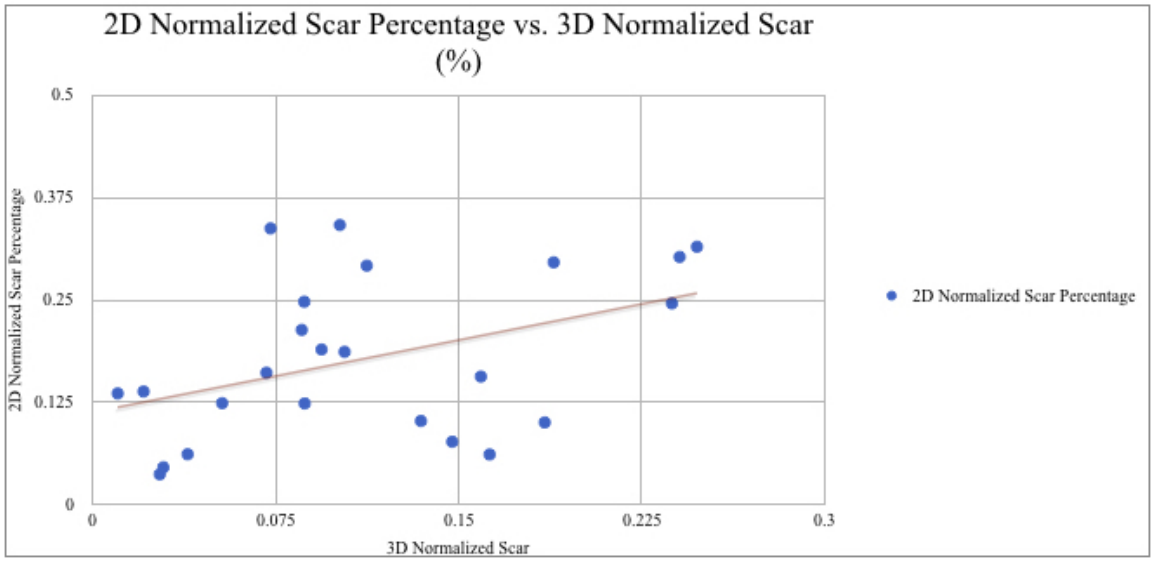

Figure 45: Correlation coefficient plot for the normalized scar volumes of using 2D and 3D LGE-MRI.

The Bland-Altman plots indicate bias, which is the difference of volumes from 2D and 3D LGE-MRI acquisitions. Further, the Bland-Altman plots show the lower and the upper limits of agreement (LOA) of the data which are the $\pm$ 1.96 times the standard deviation between the volume differences of volumes obtained from 2D and 3D images. Our results showed $1.89 \pm 21.63\ cm^3$ bias in scar volume differences between 2D and 3D LGE-MRI. The majority of the data lied between the upper and the lower LOA, showing a good degree of agreement.

The Bland-Altman plots from Figure 46 reveal no significant difference in the means of scar volume results between 2D and 3D LGE-MRI. Therefore, the results indicate that the 2D and 3D LGE-MRI can be used interchangeably for the volumes of manual scar segmentations. For the paired t-test, we set the null hypothesis, H_0, as there is no difference between 2D and 3D scar volume measurements. For the scar volume measurements, we accept the H_0 and found that there is no significant difference ($p > 0.05$) between 2D and 3D LGE-MRI.

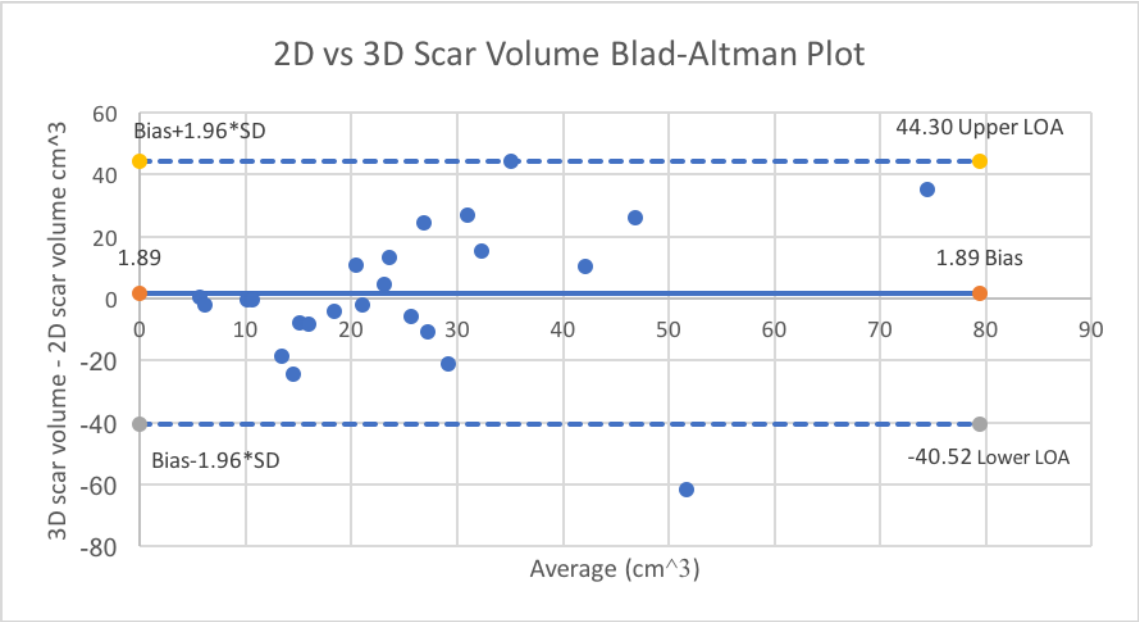

Figure 46: Comparison of the scar volumes from 2D versus 3D LGE-MRI using Bland-Altman plots.

4.5 Discussion

We present a comparison study to analyze the myocardial scar geometries obtained from 2D and 3D LGE-MRI. With this comparison study, we aim to provide insight into the differences between 2D and 3D scar segmentation for applications requiring 3D geometries of myocardial scar. Previous studies [53] have investigated only on the volume differences between the scar geometries generated from 2D and 3D LGE-MR images. Furthermore, we analyzed the scar geometries of manual scar and myocardium segmentations using several shape and volume metrics. We also presented statistical comparison methods. To our knowledge, this study is the first attempt at investigating differences in scar geometries generated using 2D and 3D LGE-MR images by analyzing various shape descriptor metrics.

In conclusion, we compared the differences in scar geometries created from 2D and 3D LGE MR images using several metrics based on the shape and volume of scar surfaces. We utilized two shape metrics to report our results. Overall, our comparisons show that

the 3D LGE-MRI method captured a more complex scar geometry than the 2D LGE-MRI. The 3D LGE-MRI presented a higher mean scar volume than the 2D LGE-MRI. These outcomes might be due to an oversight of the manual 2D scar segmentations. We obtained the manual scar segmentations from a single observer. Therefore, a consensus of manual scar segmentation from 2D LGE-MRI might give different outcomes in terms of mean scar volume. Previous studies only compared the 2D and 3D LGE-MR images and the segmentations using metrics related to the scar mass and scar volume; therefore, this study is unique in comparing the shape of scar geometries obtained from 2D and 3D LGE-MR images.

4.5.1 Limitations of our Study on the Comparison of Scar Geometry using 2D and 3D LGE-MRI (Chapter 4)

For our comparison study on comparing the manual scar geometries, our results were limited to the small number of patients. We used two different but simultaneously acquired 2D and 3D LGE-MR image datasets from twenty-four patients. For more conclusive comparisons, the 2D and 3D image datasets need to be expanded.

For comparing the reconstructed scar geometries obtained using 2D and 3D LGE-MR images, we used two shape descriptor metrics, the fractal dimensions and the number of connected components. Since different metrics provide different insights into the shape of the scar surface, more metrics need to be developed. It is important to understand the smoothness, concavity, or sparsity of shapes; therefore, more metrics such as mean curvature analysis can be included in the future studies.

Accuracy and reproducibility are some of the most important aspects of medical image segmentation since clinical applications of the scar segmentation methods are intolerant to any errors. Therefore, multiple accuracy metrics need to be computed to evaluate the scar segmentation algorithms in respect to different aspects of different aspects of the segmented scar structures.

5

Summary and Conclusion

Computing the myocardial scar volume is an important clinical problem as it is used as a biomarker in clinical procedures in myocardial scarring and predicting the risk of ventricular arrhythmias in patients. Furthermore, the segmentation and modeling of the scar surface are of the utmost importance for image-guided therapies of ventricular arrhythmias. In the scope of this thesis, we segmented the myocardial scar using a continuous max-flow (CMF) segmentation method from 3D LGE-MR images. We evaluated our algorithm on thirty-four patients data by comparing our results against the manual scar segmentations as a surrogate of ground truth. We also conducted a study to compare the reconstructed geometries of scar that are generated from conventional 2D LGE-MR images to the ones generated from high-resolution 3D LGE-MR images. In this chapter, we provide the summaries of our two main method chapters. We conclude by providing suggestions on possible future work and explaining the limitations of our study.

5.1 Summary

In this section, we summarize our scar segmentation techniques briefly by explaining the motivation, experimental setup and our results for the 3D scar segmentation and comparison of reconstructed scar structures.

5.1.1 Summary of our 3D Scar Segmentation Study using the CMF Method (Chapter 3)

In Chapter 3, our objective was to develop a myocardial scar segmentation method using 3D LGE-MR images. We mentioned that due to the latest advancements in image acquisition technology in the past decade, acquiring 3D high-resolution images of the whole heart is possible. These 3D LGE-MR images provide approximately one millimeter inner and outer-plane resolutions as well as high scar contrast in LGE-MR images. On the other hand, we noted that 2D LGE-MR images lack detailed information in the out-of-plane resolution, which may yield inconclusive results in scar segmentation. Since manual scar segmentation is a tedious task from 3D LGE-MR images, computerized scar segmentation methods were needed. Although a decent amount of research has been dedicated on segmenting the scar from 2D LGE-MRI, the 3D scar segmentation methods are limited, which motivated our research on the myocardial scar segmentation methods using the 3D LGE-MR images.

In Chapter 3, we segmented the myocardial scar tissue using an optimization based CMF method from thirty-four 3D LGE-MR images. The region of interest for scar segmentation was restricted using manual myocardium segmentations. We then used an intensity log-likelihood data term from intensity histograms of healthy and scarred myocardium regions. We also incorporated a gradient-weighted smoothness term into the segmentation.

By expressing the segmentation problem as an optimization problem, the CMF method evolved an initial surface S_t based on some energy functions; e_f, e_b, and $g(x)$,

which represented the cost to change a voxel label from background to foreground, from foreground to background, and smoothness term, respectively. Using the CMF method, we expressed the cost function as a non-linear and non-convex continuous min-cut problem. We then expressed the continuous min-cut as its dual convex version, continuous max-flow problem and solved it efficiently.

We quantitatively evaluated our CMF method by comparing the algorithm scar segmentation results against manual expert segmentation results. In particular, we evaluated our results using several comparison metrics to analyze the scar volume and scar surface overlap. We also compared our CMF method to the conventional segmentation methods, such as full-width-at-half-maximum (FWHM) and several signal-threshold-to-reference-mean (STRM) methods. We showed that the CMF method outperformed conventional scar segmentation methods in the majority of comparison metrics presented. We performed several different statistical analysis for comparing the results of the aforementioned algorithms and the manual scar segmentations. Ultimately, the CMF method outperformed conventional methods by yielding the DSC of 72.18±8.51% when compared to the DSC of 59.77±12.29% and 58.3±15% from FWHM and STRM 5-SD methods, respectively. The scar volumes generated using the CMF method statistically agreed with the scar volumes generated manually by medical experts.

To be able to understand the observer variability for manual scar segmentations, we performed an inter and intra-observer variability analysis for scar segmentations from 3D LGE-MR images. We asked three different observers to segment a randomly selected subset of five 3D LGE-MR images repetitively three times. To overcome the memory bias, the observers were asked to perform the repetitions of the segmentations on different days for the same patient. We calculated the volumes of manual scar segmentations from each observer. The variations in scar volumes among three observers showed that there were differences in segmented scar volumes among different observers. For the intraobserver variability, the repetitive scar segmentations showed that each observer had certain variability in their own delineations when they were asked to re-segment the

scar on the same dataset three times on different days.

5.1.2 Summary of our Study on the Comparison of Scar Geometries using 2D and 3D LGE-MRI (Chapter 4)

In Chapter 4, to understand the differences in reconstructed geometry of scar generated using 2D vs 3D LGE-MRI, we compared manual scar segmentations using separate datasets of twenty-four 2D and twenty-four 3D LGE-MR images. We noted that the myocardial scar geometry obtained using 2D and 3D LGE-MR images differ, and the reconstructed geometry of scar greatly influences the outcomes of VT simulations [49]. Our work was motivated by the fact that the previous studies although comparing the 2D and 3D LGE-MRI in regards to several cardiac metrics such as scar volume [53], scar mass [53], SNR [83], and image acquisition times [53], have not explored the reconstructed scar geometries. Therefore, we quantitatively analyzed the scar geometries based on scar volume as well as the shape of scar geometries.

The computed shape metrics showed that the 3D LGE-MRI produced a more complex scar structure; capturing the sparse nature of the scar, having fewer disconnected regions and higher fractal dimension than the 2D LGE-MRI. The volume metrics revealed that the 3D LGE-MRI produced a larger volume of the scar than the 2D LGE-MRI. Further, we presented a statistical analysis of the manual scar and myocardium segmentations to compare the volumes obtained from 2D and 3D LGE-MR images. According to the Bland-Altman and student t-test, we found that there were no significant differences in scar volumes generated using 2D and 3D LGE-MRI, and they could be used interchangeably.

5.2 Conclusion

In this thesis, we developed a continuous max-flow based image processing method for segmenting the myocardial scar from thirty-four 3D LGE-MR images. In our evaluation of accuracy in segmentation, the CMF method outperformed other widely used th meth-

ods in terms of segmentation accuracy in almost all presented metrics. Using the CMF method, we segmented the myocardial scar tissue within the borders of the pre-segmented myocardium without any further user interactions. The proposed CMF method yielded a mean DSC of 72±18% accuracy, outperforming the most commonly used methods for scar segmentation including the FWHM and the STRM methods.

We also conducted a comparison study to analyze the myocardial scar geometries obtained using twenty-four 2D and 3D LGE-MR images. We compared the differences in reconstructed scar geometries created from 2D and 3D LGE MR images using several metrics based on shape and volume of scar surfaces. Overall, our comparisons show that the 3D LGE-MRI method captured a more complex scar geometry than the 2D-reconstructed method which might be more helpful for interpreting the scar shape for clinical applications. The 3D LGE-MRI presented a higher mean scar volume than the 2D LGE-MRI. This might be due to the large slice-thickness (8 mm) in the LGE-MR images, which might lead to an oversight in the manual scar segmentation results. A consensus of manual scar segmentations from several observers using 2D LGE-MRI might yield varying results in terms of mean scar volume. Previous studies have investigated only the differences in scar mass, scar volume, and statistical analysis between the scar geometries generated from 2D and 3D LGE-MR images; therefore, this study is unique in comparing the shape of scar surfaces obtained from 2D and 3D LGE-MR images.

5.3 Future Directions

Scar segmentation is a challenging task due to the complexity of medical images, varying size and shape of scar structures, the presence of false positive scar structures, and the relativity of image contrast due to patient differences in LGE-MRI. Therefore, researchers make continuous efforts to develop algorithms which outperform other methods [36]. Since 3D LGE-MRI is capable of providing high-quality information beyond the human eye can realize, there is a need to conduct even further computerized studies to unlock the full potential of the 3D LGE-MR imaging in scar segmentation.

5.3.1 Myocardium Segmentation

In our developed scar segmentation method, the largest drawback is the prerequisite of the manually segmented myocardium. Automating the myocardium segmentation will decrease the introduced human error and total time for the scar segmentation [82]. Atlas-based segmentation methods are suitable for segmenting objects that have a certain shape such as the donut-shaped heart myocardium or the skull of the brain. These methods can create an average model of the heart by non-rigidly registering different patients' heart images into each other. Then, the resulted non-rigid registration map can be applied to manual myocardial segmentations to align the labels with the registered heart images. Finally, any new image (called target image) can be segmented by registering it to the model heart (called atlas), which produces a label for the target image based on its similarity to the atlas heart model.

To automatically segment the myocardium, we explored an atlas-based segmentation method [113] on a random subset of twenty-four 3D magnetic resonance angiography (MRA) images. Our atlas method yielded a DSC of 75% accuracy when compared to the manual myocardium segmentations. However, our atlas method under-segmented the myocardium along the endocardial boundaries, which caused our CMF algorithm to miss the scar structures in these locations. Therefore, the scar segmentation results dropped from 72% to 45% after applying the atlas segmented myocardium as a region of interest to our CMF method. Due to the computational expenses of the atlas method, we stopped doing further experiments for the automated myocardium segmentation. For future work, an atlas-based myocardium segmentation method can be utilized with the use of graphics processing units (GPU) for accelerating the registration step of the atlas methods.

5.3.2 Machine Learning Techniques

Machine learning and deep learning methods have shown a tremendous potential for computer vision and image segmentation applications. Although there are several recently

developed methods exist in the scar segmentation using machine learning techniques from the 2D and the 3D LGE-MR images, these methods either use a 2D LGE-MRI [58] or perform on a small 3D dataset [109]. A machine learning method that has been evaluated on a larger 3D LGE-MR image dataset to segment the myocardial scar is still missing. Using several machine learning approaches, the 3D scar can be segmented for future studies.

The convolutional neural networks (CNN) are the most popular machine learning method that can be used for semantic segmentation tasks. The CNN models are capable of automatically learning image features solely from the 3D LGE-MR images. These models can learn an extensive number of features that are not intuitive or visible to the human eye for solving this challenging segmentation problem. This feature of the CNN can defeat other classical image segmentation methods; therefore, it is surely the next step to pursue the myocardial scar segmentation studies.

To explore machine learning techniques for our scar segmentation task using the preliminarily experimented CNN model, we randomly separated our 3D image dataset into two for training and testing. We selected ten images out of thirty-four for training and the remaining twenty-four images for testing. For training and testing, we used manually segmented myocardiums to limit the region-of-interest for the CNN method. We then used a sliding window approach to prepare the data for training. For this, we extracted small overlapping images (7x7 squares of pixels) that we call patches. Each patch was assigned a label. The label '1' is for scar and the label '0' is for background based on the majority of pixels belonging to either class within each patch. We trained our CNN model on over a million image patches that we call samples. We tuned several hyperparameters for our CNN model. Table 9 shows the hyperparameters used for training the network. We tested our model on a separated testing dataset of twenty-four patients. We then computed a DSC accuracy metric between the CNN scar segmentation results and the manual scar segmentations. The CNN method yielded a mean DSC of 68.9% over twenty-four 3D LGE-MR images. Due to the time constraints we had, we stopped

Table 9: Hyper-parameters of the preliminary CNN model for the myocardial scar segmentation.

patch size	window size	epochs	scar ratio	scar definition ratio
1	7	20	30%	50%

exploring the machine learning techniques for the scar segmentation task using 3D LGE-MR images. We believe that the machine learning techniques, CNN, in particular, will be suitable for scar segmentation as well as the myocardium segmentation tasks from 3D LGE-MR images in the near future.

5.3.3 Medical Image Segmentation Challenges

To solve the challenging medical image segmentation problems, several challenges have taken place in recent years on different topics. In these challenges, given a clinically driven motivation, such as scar segmentation, researchers are provided with common training data to develop their algorithms on. After the submission of final algorithms, researchers are given a new dataset to test their algorithms. These challenges are important since they simulate the real-life clinical scenario where the data is always new and unexpected for the pre-written medical image segmentation algorithms. As for the future directions, several scar algorithm challenges in scar segmentation will be helpful to evaluate our scar segmentation method.

References

[1] Duckett, S.G. *et al.* *Cardiac MRI to investigate myocardial scar and coronary venous anatomy using a slow infusion of dimeglumine gadobenate in patients undergoing assessment for cardiac resynchronization therapy.* Journal of Magnetic Resonance Imaging, **33**(1):87–95 (2011). ISSN 10531807. http://dx.doi.org/10.1002/jmri.22387. (Cited on pages 1 and 50.)

[2] Shetty, A.K. *et al.* *Cardiac magnetic resonance-derived anatomy, scar, and dyssynchrony fused with fluoroscopy to guide LV lead placement in cardiac resynchronization therapy: a comparison with acute haemodynamic measures and echocardiographic reverse remodelling.* European Heart Journal - Cardiovascular Imaging, **14**(7):692–699 (2013). ISSN 2047-2404, 2047-2412. http://dx.doi.org/10.1093/ehjci/jes270. (Cited on pages 1 and 50.)

[3] Giannakidis, A. *et al.* *Rapid automatic segmentation of abnormal tissue in late gadolinium enhancement cardiovascular magnetic resonance images for improved management of long-standing persistent atrial fibrillation.* BioMedical Engineering OnLine, **14**(1):88 (2015). ISSN 1475-925X. http://dx.doi.org/10.1186/s12938-015-0083-8. (Cited on pages 1, 52, and 73.)

[4] Yuan, J. *et al.* *A fast global optimization-based approach to evolving contours with generic shape prior.* submission in IEEE TPAMI, also UCLA Tech. Report CAM 12, **38** (2012). (Cited on pages 1, 3, 40, 43, 44, 49, 53, 55, and 56.)

[5] Usta, F. *et al. 3D scar segmentation from LGE-MRI using a continuous max-flow method*. page 29 (2018). http://dx.doi.org/10.1117/12.2294406. (Cited on page 5.)

[6] Usta, F. *et al. Comparison of myocardial scar geometries generated from 2D and 3D LGE MRI*. page 19 (2018). http://dx.doi.org/10.1117/12.2293961. (Cited on page 5.)

[7] Go, A.S. *et al. Heart Disease and Stroke Statistics—2014 Update*. Circulation, **129**(3):e28–e292 (2014). ISSN 0009-7322. http://dx.doi.org/10.1161/01.cir.0000441139.02102.80. (Cited on page 6.)

[8] Bogaert, J. *et al.*, editors. *Clinical Cardiac MRI*. Medical Radiology. Springer Berlin Heidelberg, Berlin, Heidelberg (2012). ISBN 978-3-642-23034-9 978-3-642-23035-6. http://link.springer.com/10.1007/978-3-642-23035-6. DOI: 10.1007/978-3-642-23035-6. (Cited on pages 7 and 33.)

[9] Arenal, A. *et al. Do the spatial characteristics of myocardial scar tissue determine the risk of ventricular arrhythmias?* Cardiovascular research, **94**(2):324–332 (2012). ISSN 1755-3245 0008-6363. http://dx.doi.org/10.1093/cvr/cvs113. (Cited on page 8.)

[10] Trayanova, N.A. *Computational cardiology: the heart of the matter*. ISRN cardiology, **2012**:269680 (2012). ISSN 2090-5599 2090-5580. http://dx.doi.org/10.5402/2012/269680. (Cited on pages 8, 28, and 50.)

[11] Kim, R.J. *et al. Relationship of MRI delayed contrast enhancement to irreversible injury, infarct age, and contractile function*. Circulation, **100**(19):1992–2002 (1999). http://circ.ahajournals.org/content/100/19/1992.short. (Cited on pages 8 and 32.)

[12] Wagner, A. *et al. Contrastenhanced MRI detects subendocardial myocardial infarcts that are missed by routine SPECT perfusion imaging.* Lancet, **361**:374–379 (2003). (Cited on page 8.)

[13] Estner, H.L. *et al. The critical isthmus sites of ischemic ventricular tachycardia are in zones of tissue heterogeneity, visualized by magnetic resonance imaging.* Heart Rhythm, **8**(12):1942–1949. ISSN 1547-5271. http://dx.doi.org/10.1016/j.hrthm.2011.07.027. (Cited on pages 9 and 35.)

[14] Gao, P. *et al. Prediction of Arrhythmic Events in Ischemic and Dilated Cardiomyopathy Patients Referred for Implantable Cardiac Defibrillator: Evaluation of Multiple Scar Quantification Measures for Late Gadolinium Enhancement Magnetic Resonance Imaging.* Circulation: Cardiovascular Imaging, **5**(4):448–456 (2012). ISSN 1941-9651, 1942-0080. http://dx.doi.org/10.1161/CIRCIMAGING.111.971549. (Cited on pages 9 and 50.)

[15] Marsan, N.A. *et al. Magnetic resonance imaging and response to cardiac resynchronization therapy: relative merits of left ventricular dyssynchrony and scar tissue.* European Heart Journal, **30**(19):2360–2367 (2009). ISSN 0195-668X, 1522-9645. http://dx.doi.org/10.1093/eurheartj/ehp280. (Cited on pages 9 and 50.)

[16] Amplatz, K. *Radiology of congenital heart disease.* Thieme-Stratton Inc.,New York, NY (1986). (Cited on page 9.)

[17] Klem, I. *et al. Assessment of Myocardial Scarring Improves Risk Stratification in Patients Evaluated for Cardiac Defibrillator Implantation.* Journal of the American College of Cardiology, **60**(5):408–420 (2012). ISSN 07351097. http://dx.doi.org/10.1016/j.jacc.2012.02.070. (Cited on page 10.)

[18] Sudarshan, V. *et al. Automated Identification of Infarcted Myocardium Tissue Characterization Using Ultrasound Images: A Review.* IEEE Reviews in Biomedical

Engineering, **8**:86–97 (2015). ISSN 1937-3333, 1941-1189. http://dx.doi.org/10.1109/RBME.2014.2319854. (Cited on page 14.)

[19] Jaarsma, W. *et al. Usefulness of two-dimensional exercise echocardiography shortly after myocardial infarction.* American Journal of Cardiology, **57**(1):86–90. ISSN 0002-9149. http://dx.doi.org/10.1016/0002-9149(86)90957-4. (Cited on page 14.)

[20] Nishimura, R.A. *et al. Role of two-dimensional echocardiography in the prediction of in-hospital complications after acute myocardial infarction.* Journal of the American College of Cardiology, **4**(6):1080–1087 (1984). (Cited on page 14.)

[21] Stypmann, J. *et al. Echocardiographic assessment of global left ventricular function in mice.* Laboratory Animals, **43**(2):127–137 (2009). ISSN 0023-6772, 1758-1117. http://dx.doi.org/10.1258/la.2007.06001e. (Cited on page 14.)

[22] Lang, R.M. *et al. Recommendations for Chamber Quantification: A Report from the American Society of Echocardiography's Guidelines and Standards Committee and the Chamber Quantification Writing Group, Developed in Conjunction with the European Association of Echocardiography, a Branch of the European Society of Cardiology.* Journal of the American Society of Echocardiography, **18**(12):1440–1463. ISSN 0894-7317. http://dx.doi.org/10.1016/j.echo.2005.10.005. (Cited on page 14.)

[23] Lavie, C.J. *et al. Impact of left ventricular geometry on prognosis—a review of Ochsner studies.* The Ochsner Journal, **8**(1):11–17 (2008). (Cited on page 14.)

[24] De Bruyne, B. and Heyndrickx, G.R. *Changes in Infarct Size and Left Ventricular Ejection Fraction.* Journal of the American College of Cardiology, **50**(2):157–158 (2007). ISSN 07351097. http://dx.doi.org/10.1016/j.jacc.2007.03.032. (Cited on page 14.)

[25] Delewi, R. *et al. Left ventricular thrombus formation after acute myocardial infarction.* Heart, **98**(23):1743–1749 (2012). (Cited on page 14.)

[26] Vidya, K.S. *et al. Computer-aided diagnosis of Myocardial Infarction using ultrasound images with DWT, GLCM and HOS methods: A comparative study.* Computers in Biology and Medicine, **62**(Complete):86–93 (2015). ISSN 00104825. http://dx.doi.org/10.1016/j.compbiomed.2015.03.033. (Cited on page 14.)

[27] Budoff, M.J. and Shinbane, J.S., editors. *Cardiac CT Imaging.* Springer International Publishing, Cham (2016). ISBN 978-3-319-28217-6 978-3-319-28219-0. http://link.springer.com/10.1007/978-3-319-28219-0. DOI: 10.1007/978-3-319-28219-0. (Cited on page 15.)

[28] Mahnken, A.H. *et al. Assessment of Myocardial Viability in Reperfused Acute Myocardial Infarction Using 16-Slice Computed Tomography in Comparison to Magnetic Resonance Imaging.* Journal of the American College of Cardiology, **45**(12):2042 – 2047 (2005). ISSN 0735-1097. http://dx.doi.org/https://doi.org/10.1016/j.jacc.2005.03.035. (Cited on page 16.)

[29] Nieman, K. *et al. Reperfused Myocardial Infarction: Contrast-enhanced 64-Section CT in Comparison to MR Imaging.* Radiology, **247**(1):49–56 (2008). http://dx.doi.org/10.1148/radiol.2471070332. PMID: 18372464. (Cited on page 16.)

[30] Yushkevich, P.A. *et al. User-guided 3D active contour segmentation of anatomical structures: Significantly improved efficiency and reliability.* NeuroImage, **31**(3):1116–1128 (2006). ISSN 10538119. http://dx.doi.org/10.1016/j.neuroimage.2006.01.015. (Cited on page 21.)

[31] Top, A. *et al. Active Learning for Interactive 3D Image Segmentation.* pages 603–610 (2011). https://doi.org/10.1007/978-3-642-23626-6_74. DOI: 10.1007/978-3-642-23626-6_74. (Cited on page 21.)

[32] Tao, Q. *et al. Automated segmentation of myocardial scar in late enhancement MRI using combined intensity and spatial information.* Magnetic Resonance in Medicine, pages n/a–n/a (2010). ISSN 07403194, 15222594. http://dx.doi.org/10.1002/mrm.22422. (Cited on pages 21, 32, 33, and 36.)

[33] Rajchl, M. *et al. Fast interactive multi-region cardiac segmentation with linearly ordered labels.* In *Biomedical Imaging (ISBI), 2012 9th IEEE International Symposium on*, pages 1409–1412. IEEE (2012). http://ieeexplore.ieee.org/abstract/document/6235832/. (Cited on pages 21 and 87.)

[34] Sorensen, T.J. *A method of establishing groups of equal amplitude in plant sociology based on similarity of species content and its application to analyses of the vegetation on Danish commons.* I kommission hos E. Munksgaard, Kobenhavn (1948). (Cited on page 23.)

[35] Dice, L.R. *Measures of the Amount of Ecologic Association Between Species*. Ecology, **26**(3):297–302 (1945). ISSN 00129658, 19399170. http://dx.doi.org/10.2307/1932409. (Cited on page 23.)

[36] Karim, R. *et al. Evaluation of state-of-the-art segmentation algorithms for left ventricle infarct from late Gadolinium enhancement MR images.* Medical image analysis, **30**:95–107 (2016). ISSN 1361-8415. (Cited on pages 23, 35, 37, 42, 47, and 101.)

[37] Baish, J.W. and Jain, R.K. *Fractals and Cancer.* Cancer Research, **60**(14):3683–3688 (2000). ISSN 0008-5472. http://cancerres.aacrjournals.org/content/60/14/3683. (Cited on page 26.)

[38] Alberich-Bayarri, A. *et al. Assessment of 2D and 3D fractal dimension measurements of trabecular bone from high-spatial resolution magnetic resonance images at 3 T.* Medical Physics, **37**(9):4930–4937 (2010). ISSN 2473-4209. http://dx.doi.org/10.1118/1.3481509. (Cited on page 27.)

[39] Di Bella, G. *et al. Scar extent, left ventricular end-diastolic volume, and wall motion abnormalities identify high-risk patients with previous myocardial infarction: a multiparametric approach for prognostic stratification.* European Heart Journal, **34**(2):104–111 (2013). ISSN 0195-668X, 1522-9645. http://dx.doi.org/10.1093/eurheartj/ehs037. (Cited on page 28.)

[40] Yokota, H. *et al. Quantitative characterization of myocardial infarction by cardiovascular magnetic resonance predicts future cardiovascular events in patients with ischemic cardiomyopathy.* Journal of Cardiovascular Magnetic Resonance, **10**(1):17 (2008). ISSN 1097-6647. http://dx.doi.org/10.1186/1532-429X-10-17. (Cited on pages 28 and 50.)

[41] Ashikaga, H. *et al. Feasibility of image-based simulation to estimate ablation target in human ventricular arrhythmia.* Heart rhythm, **10**(8):1109–1116 (2013). ISSN 1556-3871 1547-5271. http://dx.doi.org/10.1016/j.hrthm.2013.04.015. (Cited on pages 28 and 29.)

[42] Winslow, R.L. *et al. Computational medicine: translating models to clinical care.* Science translational medicine, **4**(158):158rv11 (2012). ISSN 1946-6242 1946-6234. http://dx.doi.org/10.1126/scitranslmed.3003528. (Cited on page 28.)

[43] Vadakkumpadan, F. *et al. Image-based estimation of ventricular fiber orientations for personalized modeling of cardiac electrophysiology.* IEEE transactions on medical imaging, **31**(5):1051–1060 (2012). ISSN 1558-254X 0278-0062. http://dx.doi.org/10.1109/TMI.2012.2184799. (Cited on pages 28 and 29.)

[44] Stillman, A.E. *et al. Assessment of acute myocardial infarction: current status and recommendations from the North American society for cardiovascular imaging and the European society of cardiac radiology.* The International Journal of Cardiovascular Imaging, **27**(1):7–24 (2011). ISSN 1569-5794. http://dx.doi.org/10.1007/s10554-010-9714-0. (Cited on page 28.)

[45] Ismail, T.F. *et al.* *Prognostic importance of late gadolinium enhancement cardiovascular magnetic resonance in cardiomyopathy.* Heart, **98**(6):438–442 (2012). ISSN 1355-6037. http://dx.doi.org/10.1136/heartjnl-2011-300814. (Cited on page 28.)

[46] Morita, K. *et al.* *Comparison of 3D Phase-Sensitive Inversion-Recovery and 2D Inversion-Recovery MRI at 3.0 T for the Assessment of Late Gadolinium Enhancement in Patients with Hypertrophic Cardiomyopathy.* Academic Radiology, **20**(6):752–757 (2013). ISSN 10766332. http://dx.doi.org/10.1016/j.acra.2013.01.014. (Cited on pages 29 and 33.)

[47] Akçakaya, M. *et al.* *Accelerated late gadolinium enhancement cardiac MR imaging with isotropic spatial resolution using compressed sensing: initial experience.* Radiology, **264**(3):691–699 (2012). http://pubs.rsna.org/doi/abs/10.1148/radiol.12112489. (Cited on pages 29 and 33.)

[48] Ukwatta, E. *et al.* *Image-based reconstruction of three-dimensional myocardial infarct geometry for patient-specific modeling of cardiac electrophysiology.* Medical physics, **42**(8):4579–4590 (2015). http://onlinelibrary.wiley.com/doi/10.1118/1.4926428/full. (Cited on pages 29, 50, 82, and 87.)

[49] Ukwatta, E. *et al.* *Myocardial Infarct Segmentation From Magnetic Resonance Images for Personalized Modeling of Cardiac Electrophysiology.* IEEE Transactions on Medical Imaging, **35**(6):1408–1419 (2016). ISSN 0278-0062, 1558-254X. http://dx.doi.org/10.1109/TMI.2015.2512711. (Cited on pages 29, 47, 50, 81, and 100.)

[50] Ukwatta, E. *et al.* *Myocardial infarct segmentation and reconstruction from 2D late-gadolinium enhanced magnetic resonance images.* Medical image computing and computer-assisted intervention : MICCAI ... International Conference on Medical

Image Computing and Computer-Assisted Intervention, **17**(Pt 2):554–561 (2014). (Cited on pages 29, 43, and 50.)

[51] Neizel, M. *et al. Rapid and accurate determination of relative infarct size in humans using contrast-enhanced magnetic resonance imaging.* Clinical Research in Cardiology, **98**(5):319–324 (2009). ISSN 1861-0684, 1861-0692. http://dx.doi.org/10.1007/s00392-009-0007-3. (Cited on pages 29, 33, 36, and 83.)

[52] Amano, Y. *et al. Free-breathing high-spatial-resolution delayed contrast-enhanced three-dimensional viability MR imaging of the myocardium at 3.0T: A feasibility study.* Journal of Magnetic Resonance Imaging, **28**(6):1361–1367 (2008). ISSN 10531807, 15222586. http://dx.doi.org/10.1002/jmri.21595. (Cited on pages 30, 33, 35, 50, 83, and 90.)

[53] Goetti, R. *et al. Acute, subacute, and chronic myocardial infarction: quantitative comparison of 2D and 3D late gadolinium enhancement MR imaging.* Radiology, **259**(3):704–711 (2011). ISSN 0033-8419. (Cited on pages 32, 33, 34, 35, 81, 83, 95, and 100.)

[54] Flett, A.S. *et al. Evaluation of Techniques for the Quantification of Myocardial Scar of Differing Etiology Using Cardiac Magnetic Resonance.* JACC: Cardiovascular Imaging, **4**(2):150–156 (2011). ISSN 1936878X. http://dx.doi.org/10.1016/j.jcmg.2010.11.015. (Cited on pages 32, 33, and 36.)

[55] Neizel, M. *et al. A fully automatic cardiac model with integrated scar tissue information for improved assessment of viability.* Journal of Cardiovascular Magnetic Resonance, **14**(Suppl 1):M12 (2012). ISSN 1532-429X. http://dx.doi.org/10.1186/1532-429X-14-S1-M12. (Cited on pages 32 and 48.)

[56] Hennemuth, A. *et al. A Comprehensive Approach to the Analysis of Contrast Enhanced Cardiac MR Images.* IEEE Transactions on Medical Imaging, **27**(11):1592–

1610 (2008). ISSN 0278-0062, 1558-254X. http://dx.doi.org/10.1109/TMI.2008.2006512. (Cited on pages 32, 33, 36, and 48.)

[57] Elagouni, K. *et al. Automatic segmentation of pathological tissues in cardiac MRI.* In *Biomedical Imaging: From Nano to Macro, 2010 IEEE International Symposium on*, pages 472–475. IEEE (2010). http://ieeexplore.ieee.org/abstract/document/5490306/. (Cited on page 32.)

[58] Xu, C. *et al. Direct detection of pixel-level myocardial infarction areas via a deep-learning algorithm.* In *International Conference on Medical Image Computing and Computer-Assisted Intervention*, pages 240–249. Springer (2017). https://link.springer.com/chapter/10.1007/978-3-319-66179-7_28. (Cited on pages 32, 33, 44, 47, and 103.)

[59] Säring, D. *et al. Analysis of the Left Ventricle After Myocardial Infarction Combining 4D Cine-MR and 3D DE-MR Image Sequences.* In H. Handels, J. Ehrhardt, A. Horsch, H.P. Meinzer and T. Tolxdorff, editors, *Bildverarbeitung für die Medizin 2006: Algorithmen Systeme Anwendungen Proceedings des Workshops vom 19. – 21. März 2006 in Hamburg*, pages 56–60. Springer Berlin Heidelberg, Berlin, Heidelberg (2006). ISBN 978-3-540-32137-8. https://doi.org/10.1007/3-540-32137-3_12. DOI: 10.1007/3-540-32137-3_12. (Cited on pages 32, 33, and 36.)

[60] Dikici, E. *et al. Quantification of Delayed Enhancement MR Images.* In C. Barillot, D.R. Haynor and P. Hellier, editors, *Medical Image Computing and Computer-Assisted Intervention – MICCAI 2004: 7th International Conference, Saint-Malo, France, September 26-29, 2004. Proceedings, Part I*, pages 250–257. Springer Berlin Heidelberg, Berlin, Heidelberg (2004). ISBN 978-3-540-30135-6. https://doi.org/10.1007/978-3-540-30135-6_31. DOI: 10.1007/978-3-540-30135-6_31. (Cited on pages 32, 33, and 39.)

[61] Kolipaka, A. *et al. Segmentation of non-viable myocardium in delayed enhancement magnetic resonance images.* The International Journal of Cardiovascular Imaging, **21**(2-3):303–311 (2005). ISSN 1569-5794, 1573-0743. http://dx.doi.org/10.1007/s10554-004-5806-z. (Cited on pages 33 and 36.)

[62] O'Donnell, T.P. *et al. Semi-automatic segmentation of nonviable cardiac tissue using cine and delayed enhancement magnetic resonance images.* In *Proc. of SPIE Vol*, volume 5031, page 243 (2003). (Cited on pages 33 and 39.)

[63] Positano, V. *et al. A fast and effective method to assess myocardial necrosis by means of contrast magnetic resonance imaging.* Journal of Cardiovascular Magnetic Resonance, **7**(2):487–494 (2005). http://www.tandfonline.com/doi/abs/10.1081/JCMR-53630. (Cited on pages 33 and 39.)

[64] Kecskemeti, S. *et al. Volumetric late gadolinium-enhanced myocardial imaging with retrospective inversion time selection: 3D Radial Delayed Enhanced Imaging.* Journal of Magnetic Resonance Imaging, **38**(5):1276–1282 (2013). ISSN 10531807. http://dx.doi.org/10.1002/jmri.24037. (Cited on pages 33 and 34.)

[65] Keegan, J. *et al. Improved respiratory efficiency of 3D late gadolinium enhancement imaging using the continuously adaptive windowing strategy (CLAWS): Improved Respiratory Efficiency of 3D LGE Imaging with CLAWS.* Magnetic Resonance in Medicine, **71**(3):1064–1074 (2014). ISSN 07403194. http://dx.doi.org/10.1002/mrm.24758. (Cited on pages 33 and 34.)

[66] Kino, A. *et al. Three-Dimensional Phase-Sensitive Inversion-Recovery Turbo FLASH Sequence for the Evaluation of Left Ventricular Myocardial Scar.* American Journal of Roentgenology, **193**(5):W381–W388 (2009). ISSN 0361-803X, 1546-3141. http://dx.doi.org/10.2214/AJR.08.1952. (Cited on pages 33 and 34.)

[67] Bauner, K.U. *et al.* *Assessment of Myocardial Viability with 3D MRI at 3 T.* American Journal of Roentgenology, **192**(6):1645–1650 (2009). ISSN 0361-803X. http://dx.doi.org/10.2214/AJR.08.1394. (Cited on page 33.)

[68] Viallon, M. *et al.* *Head-to-head comparison of eight late gadolinium-enhanced cardiac MR (LGE CMR) sequences at 1.5 tesla: From bench to bedside.* Journal of Magnetic Resonance Imaging, **34**(6):1374–1387 (2011). ISSN 10531807. http://dx.doi.org/10.1002/jmri.22783. (Cited on page 33.)

[69] Matsumoto, H. *et al.* *Feasibility of free-breathing late gadolinium-enhanced cardiovascular MRI for assessment of myocardial infarction: Navigator-gated versus single-shot imaging.* International Journal of Cardiology, **168**(1):94–99 (2013). ISSN 01675273. http://dx.doi.org/10.1016/j.ijcard.2012.09.066. (Cited on page 33.)

[70] Syed, M.A. and Mohiaddin, R.H., editors. *Magnetic Resonance Imaging of Congenital Heart Disease.* Springer London, London (2012). ISBN 978-1-4471-4266-9 978-1-4471-4267-6. http://link.springer.com/10.1007/978-1-4471-4267-6. DOI: 10.1007/978-1-4471-4267-6. (Cited on page 33.)

[71] Rajchl, M. *et al.* *Comparison of semi-automated scar quantification techniques using high-resolution, 3-dimensional late-gadolinium-enhancement magnetic resonance imaging.* The international journal of cardiovascular imaging, **31**(2):349–357 (2015). ISSN 1875-8312 1569-5794. http://dx.doi.org/10.1007/s10554-014-0553-2. (Cited on pages 33, 34, 35, 37, 38, 50, and 51.)

[72] Nguyen, T.D. *et al.* *A fast navigator-gated 3D sequence for delayed enhancement MRI of the myocardium: Comparison with breathhold 2D imaging.* Journal of Magnetic Resonance Imaging, **27**(4):802–808 (2008). ISSN 10531807, 15222586. http://dx.doi.org/10.1002/jmri.21296. (Cited on page 34.)

[73] Peters, D.C. *et al. Left ventricular infarct size, peri-infarct zone, and papillary scar measurements: A comparison of high-resolution 3D and conventional 2D late gadolinium enhancement cardiac MR.* Journal of Magnetic Resonance Imaging, **30**(4):794–800 (2009). ISSN 10531807, 15222586. http://dx.doi.org/10.1002/jmri.21897. (Cited on page 34.)

[74] van den Bosch, H.C.M. *et al. Free-Breathing MRI for the Assessment of Myocardial Infarction: Clinical Validation.* American Journal of Roentgenology, **192**(6):W277–W281 (2009). ISSN 0361-803X, 1546-3141. http://dx.doi.org/10.2214/AJR.08.1580. (Cited on page 34.)

[75] Foo, T.K.F. *et al. Myocardial Viability: Breath-hold 3D MR Imaging of Delayed Hyperenhancement with Variable Sampling in Time.* Radiology, **230**(3):845–851 (2004). ISSN 0033-8419, 1527-1315. http://dx.doi.org/10.1148/radiol.2303021411. (Cited on page 34.)

[76] Dewey, M. *et al. Myocardial Viability: Assessment with Three-dimensional MR Imaging in Pigs and Patients.* Radiology, **239**(3):703–709 (2006). http://dx.doi.org/10.1148/radiol.2393050586. (Cited on page 34.)

[77] Kim, R.J. *et al. How we perform delayed enhancement imaging.* Journal of cardiovascular magnetic resonance : official journal of the Society for Cardiovascular Magnetic Resonance, **5**(3):505–514 (2003). ISSN 1097-6647 1097-6647. (Cited on page 34.)

[78] Kim, R.J. *et al. How We Perform Delayed Enhancement Imaging.* Journal of Cardiovascular Magnetic Resonance, **5**(3):505–514 (2003). http://dx.doi.org/10.1081/JCMR-120022267. PMID: 12882082. (Cited on page 34.)

[79] Andreu, D. *et al. Integration of 3D electroanatomic maps and magnetic resonance scar characterization into the navigation system to guide ventricular tachycardia ab-*

lation. Circulation: Arrhythmia and Electrophysiology, pages CIRCEP–111 (2011). ISSN 1941-3149. (Cited on pages 34, 35, and 50.)

[80] Fernández-Armenta, J. *et al. Three-dimensional architecture of scar and conducting channels based on high resolution ce-CMR: insights for ventricular tachycardia ablation.* Circulation: Arrhythmia and Electrophysiology, pages CIRCEP–113 (2013). http://circep.ahajournals.org/content/early/2013/05/17/CIRCEP.113.000264.short. (Cited on pages 34 and 50.)

[81] White, J.A. *et al. Fused Whole-Heart Coronary and Myocardial Scar Imaging Using 3-T CMR.* JACC: Cardiovascular Imaging, **3**(9):921–930 (2010). ISSN 1936878X. http://dx.doi.org/10.1016/j.jcmg.2010.05.014. (Cited on page 34.)

[82] Rajchl, M. *et al. Interactive Hierarchical-Flow Segmentation of Scar Tissue From Late-Enhancement Cardiac MR Images.* IEEE transactions on medical imaging, **33**(1):159–172 (2014). ISSN 1558-254X 0278-0062. http://dx.doi.org/10.1109/TMI.2013.2282932. (Cited on pages 34, 35, 44, 47, 51, 52, 74, 87, and 102.)

[83] Pierce, I.T. *et al. Free-breathing 3D late gadolinium enhancement imaging of the left ventricle using a stack of spirals at 3T.* Journal of Magnetic Resonance Imaging, **41**(4):1030–1037 (2015). ISSN 1522-2586. (Cited on pages 35, 81, 83, and 100.)

[84] Otsu, N. *A Threshold Selection Method from Gray-Level Histograms.* IEEE Transactions on Systems, Man, and Cybernetics, **9**(1):62–66 (1979). ISSN 0018-9472. http://dx.doi.org/10.1109/TSMC.1979.4310076. (Cited on page 36.)

[85] VLIDIS, T.P. *Integrating Region Growing and Edge Detection.* page 9. (Cited on page 36.)

[86] V. Grau *et al. Improved watershed transform for medical image segmentation using prior information.* IEEE Transactions on Medical Imaging, **23**(4):447–458 (2004). ISSN 0278-0062. http://dx.doi.org/10.1109/TMI.2004.824224. (Cited on page 39.)

[87] Cimino, M.G. *et al. A novel approach to fuzzy clustering based on a dissimilarity relation extracted from data using a TS system*. Pattern Recognition, **39**(11):2077–2091 (2006). ISSN 0031-3203. http://dx.doi.org/10.1016/j.patcog.2006.05.005. (Cited on page 39.)

[88] D. J. hemanth *et al. Effective Fuzzy Clustering Algorithm for Abnormal MR Brain Image Segmentation*. In *2009 IEEE International Advance Computing Conference*, pages 609–614 (2009). http://dx.doi.org/10.1109/IADCC.2009.4809081. (Cited on page 39.)

[89] Vasuda, P. and Satheesh, S. *Improved fuzzy C-means algorithm for MR brain image segmentation*. International Journal on Computer Science and Engineering, **2**(5):2010 (1713). (Cited on page 39.)

[90] X. Li *et al. Research and Application of Improved K-Means Algorithm Based on Fuzzy Feature Selection*. In *2008 Fifth International Conference on Fuzzy Systems and Knowledge Discovery*, volume 1, pages 401–405 (2008). http://dx.doi.org/10.1109/FSKD.2008.451. (Cited on page 39.)

[91] Khan, S.S. and Ahmad, A. *Cluster Center Initialization Algorithm for K-means Clustering*. Pattern Recogn. Lett., **25**(11):1293–1302 (2004). ISSN 0167-8655. http://dx.doi.org/10.1016/j.patrec.2004.04.007. (Cited on page 39.)

[92] Detsky, J. *et al. Reproducible Classification of Infarct Heterogeneity Using Fuzzy Clustering on Multicontrast Delayed Enhancement Magnetic Resonance Images*. IEEE Transactions on Medical Imaging, **28**(10):1606–1614 (2009). ISSN 0278-0062, 1558-254X. http://dx.doi.org/10.1109/TMI.2009.2023515. (Cited on pages 39 and 48.)

[93] Kass, M. *et al. Snakes: Active contour models*. International journal of computer vision, **1**(4):321–331 (1988). (Cited on page 40.)

[94] Osher, S. and Sethian, J.A. *Fronts propagating with curvature-dependent speed: algorithms based on Hamilton-Jacobi formulations*. Journal of computational physics, **79**(1):12–49 (1988). (Cited on pages 40 and 41.)

[95] Boykov, Y. and Funka-Lea, G. *Graph Cuts and Efficient N-D Image Segmentation*. Int. J. Comput. Vision, **70**(2):109–131 (2006). ISSN 0920-5691. http://dx.doi.org/10.1007/s11263-006-7934-5. (Cited on pages 40 and 42.)

[96] Yuan, J. *et al. A continuous max-flow approach to potts model*. Computer Vision–ECCV 2010, pages 379–392 (2010). (Cited on page 40.)

[97] Mahesan, K.V. *et al. Segmentation of MR Images using Active Contours: Methods, Challenges and Applications*. International Journal of Innovative Research in Advanced Engineering, **4**(02):9 (2017). (Cited on pages 40 and 41.)

[98] McInerney, T. and Terzopoulos, D. *MTedopicoallogImicaalgley SAedgampetnatbaletioSnnaUkseisng*. page 10. (Cited on page 41.)

[99] Zhou, W. and Xie, Y. *Interactive Medical Image Segmentation Using Snake and Multiscale Curve Editing*. Computational and Mathematical Methods in Medicine, **2013**:1–13 (2013). ISSN 1748-670X, 1748-6718. http://dx.doi.org/10.1155/2013/325903. (Cited on page 41.)

[100] Bumrungkun, P. *et al. Detection Skin Cancer Using SVM and Snake Model*. page 4. (Cited on page 41.)

[101] Itai, Y. *et al. A SEGMENTATION METHOD OF LUNG AREAS BY USING SNAKES AND AUTOMATIC DETECTION OF ABNORMAL SHADOW ON THE AREAS*. page 8. (Cited on page 41.)

[102] Lara, L. *et al. Supervised learning modelization and segmentation of cardiac scar in delayed enhanced MRI*. In *International Workshop on Statistical Atlases and Computational Models of the Heart*, pages 53–61. Springer (2012). (Cited on page 42.)

[103] Karim, R. *et al.* *Infarct segmentation of the left ventricle using graph-cuts*. In *International Workshop on Statistical Atlases and Computational Models of the Heart*, pages 71–79. Springer (2012). (Cited on page 42.)

[104] Lu, Y. *et al.* *Automated quantification of myocardial infarction using graph cuts on contrast delayed enhanced magnetic resonance images.* Quantitative imaging in medicine and surgery, **2**(2):81–86 (2012). ISSN 2223-4292 2223-4306. http://dx.doi.org/10.3978/j.issn.2223-4292.2012.05.03. (Cited on pages 42 and 50.)

[105] Li, S.Z. and Li, S. Z., . *Markov Random Field Modeling in Image Analysis*. Advances in pattern recognition. Springer London, London. ISBN 1-84800-278-5. (Cited on page 43.)

[106] Klodt, M. *et al.* *An Experimental Comparison of Discrete and Continuous Shape Optimization Methods*. In D. Forsyth, P. Torr and A. Zisserman, editors, *Computer Vision – ECCV 2008: 10th European Conference on Computer Vision, Marseille, France, October 12-18, 2008, Proceedings, Part I*, pages 332–345. Springer Berlin Heidelberg, Berlin, Heidelberg (2008). ISBN 978-3-540-88682-2. https://doi.org/10.1007/978-3-540-88682-2_26. DOI: 10.1007/978-3-540-88682-2_26. (Cited on page 43.)

[107] Litjens, G. *et al.* *A survey on deep learning in medical image analysis*. arXiv preprint arXiv:1702.05747 (2017). https://arxiv.org/abs/1702.05747. (Cited on page 44.)

[108] Shen, D. *et al.* *Deep learning in medical image analysis*. Annual Review of Biomedical Engineering, (0) (2017). (Cited on page 45.)

[109] Zabihollahy, F. *et al.* *Myocardial scar segmentation from magnetic resonance images using convolutional neural network*. page 106. SPIE (2018). ISBN 978-1-5106-1639-4 978-1-5106-1640-0. http://dx.doi.org/10.1117/12.2293518. (Cited on pages 47 and 103.)

[110] Karim, R. *et al. A Method to Standardize Quantification of Left Atrial Scar From Delayed-Enhancement MR Images.* IEEE Journal of Translational Engineering in Health and Medicine, **2**:1–15 (2014). http://dx.doi.org/10.1109/JTEHM.2014.2312191. (Cited on page 48.)

[111] Yuan, J. *et al. A study on continuous max-flow and min-cut approaches.* In *Computer Vision and Pattern Recognition (CVPR), 2010 IEEE Conference on*, pages 2217–2224. IEEE (2010). http://ieeexplore.ieee.org/abstract/document/5539903/. (Cited on pages 56 and 57.)

[112] Boykov, Y.Y. and Jolly, M.P. *Interactive graph cuts for optimal boundary & region segmentation of objects in ND images.* In *Computer Vision, 2001. ICCV 2001. Proceedings. Eighth IEEE International Conference on*, volume 1, pages 105–112. IEEE (2001). http://ieeexplore.ieee.org/abstract/document/937505/. (Cited on page 57.)

[113] Wang, H. *et al. Multi-Atlas Segmentation with Joint Label Fusion.* IEEE transactions on pattern analysis and machine intelligence, **35**(3):611–623 (2013). ISSN 0162-8828. http://dx.doi.org/10.1109/TPAMI.2012.143. (Cited on pages 76 and 102.)

[114] Sabuncu, M.R. *et al. A Generative Model for Image Segmentation Based on Label Fusion.* IEEE transactions on medical imaging, **29**(10):1714–1729 (2010). ISSN 0278-0062. http://dx.doi.org/10.1109/TMI.2010.2050897. (Cited on page 76.)

[115] *Multi-Atlas-Based Segmentation With Local Decision Fusion x2014;Application to Cardiac and Aortic Segmentation in CT Scans.* IEEE Transactions on Medical Imaging, **28**(7):1000–1010 (2009). ISSN 0278-0062. http://dx.doi.org/10.1109/TMI.2008.2011480. (Cited on page 76.)

[116] *Fast Free-form Deformation Using Graphics Processing Units*. Comput. Methods Prog. Biomed., **98**(3):278–284 (2010). ISSN 0169-2607. http://dx.doi.org/10.1016/j.cmpb.2009.09.002. (Cited on page 77.)

[117] Rueckert, D. *et al. Nonrigid registration using free-form deformations: application to breast MR images*. IEEE Transactions on Medical Imaging, **18**(8):712–721 (1999). ISSN 0278-0062. http://dx.doi.org/10.1109/42.796284. (Cited on page 77.)

[118] Ourselin, S. *et al. Reconstructing a 3D structure from serial histological sections*. Image and vision computing, **19**(1):25–31 (2001). http://www.sciencedirect.com/science/article/pii/S0262885600000524. (Cited on page 78.)

[119] Modat, M. *et al. Fast free-form deformation using graphics processing units*. Computer Methods and Programs in Biomedicine, **98**(3):278–284 (2010). ISSN 01692607. http://dx.doi.org/10.1016/j.cmpb.2009.09.002. (Cited on page 78.)

[120] Yushkevich, P.A. *et al. User-Guided 3D Active Contour Segmentation of Anatomical Structures: Significantly Improved Efficiency and Reliability*. Neuroimage, **31**(3):1116–1128 (2006). (Cited on page 85.)

[121] Pohl, K.M. *et al. Using the logarithm of odds to define a vector space on probabilistic atlases*. Medical Image Analysis, **11**(5):465–477 (2007). ISSN 13618415. http://dx.doi.org/10.1016/j.media.2007.06.003. (Cited on page 86.)

Appendixes

Results of 3D Algorithm Scar Segmentation Study from 3D LGE-MRI

Appendix A.1 DSC Accuracy Results of Different Scar Segmentation Methods

Table 10: DCS (%) value of CMF, FWHM, STRM 2-SD, 3-SD, 5-SD, and 6-SD methods for over 34 patients.

pID	CMF	FWHM	STRM 2-SD	STRM 3-SD	STRM 5-SD	STRM 6-SD
1	80.297%	61.940%	73.670%	78.710%	51.980%	27.840%
2	83.494%	55.810%	73.930%	84.920%	71.000%	50.580%
3	67.885%	75.180%	7.970%	16.840%	55.810%	73.790%
4	57.011%	64.120%	32.550%	46.710%	61.640%	38.000%
5	65.500%	68.700%	35.650%	57.200%	65.250%	31.680%
6	64.028%	66.250%	37.680%	53.780%	68.380%	55.070%
7	79.015%	60.090%	39.440%	55.500%	75.290%	68.270%
8	64.008%	79.510%	33.240%	54.060%	79.080%	71.850%
9	78.695%	46.560%	80.680%	67.770%	19.890%	4.880%
10	66.309%	74.370%	34.230%	56.360%	68.360%	37.900%
11	68.278%	59.200%	18.600%	30.010%	55.900%	63.610%
13	67.422%	66.740%	18.900%	35.620%	65.710%	65.590%

14	79.188%	69.520%	62.060%	76.510%	57.640%	26.420%
15	77.822%	54.310%	63.130%	77.780%	54.560%	30.710%
16	65.885%	43.670%	46.020%	64.790%	54.900%	36.160%
17	69.288%	27.650%	38.800%	56.240%	73.330%	71.990%
18	56.618%	43.010%	3.390%	5.650%	17.090%	25.750%
19	66.903%	76.770%	46.760%	67.910%	68.560%	43.190%
20	68.984%	44.490%	78.190%	77.880%	57.790%	41.210%
21	81.912%	66.660%	9.370%	18.060%	56.100%	68.750%
22	79.204%	66.320%	44.080%	62.940%	74.300%	64.040%
23	79.583%	76.890%	70.610%	80.540%	59.130%	32.320%
24	79.095%	75.990%	51.360%	67.810%	76.820%	70.910%
25	78.141%	56.490%	76.450%	78.090%	42.210%	18.700%
26	75.430%	47.700%	58.660%	71.540%	64.870%	49.500%
27	74.720%	42.580%	40.200%	60.940%	65.260%	43.960%
28	74.755%	67.730%	43.790%	63.710%	63.000%	45.720%
29	81.239%	47.000%	60.930%	75.520%	60.040%	37.300%
30	67.930%	49.040%	11.860%	24.190%	49.630%	45.930%
31	82.950%	61.260%	72.980%	81.850%	44.340%	19.090%
32	79.652%	68.350%	48.210%	72.290%	60.500%	35.050%
33	76.526%	69.060%	46.460%	62.610%	72.530%	56.190%
34	47.899%	57.620%	14.350%	23.910%	49.170%	59.190%
MIN	47.899%	27.650%	3.390%	5.650%	17.090%	4.880%
MAX	83.494%	79.510%	80.680%	84.920%	79.080%	73.790%
MEAN	72.183%	60.230%	43.480%	56.320%	58.310%	45.520%
STD	8.511%	12.370%	23.100%	22.838%	15.192%	17.934%

Appendix A.2 Scar Volumes using Different Segmentation Methods

Table 11: Volume values ($cm\hat{3}$) of 34 3D LGE-MR images using Manual Scar, Manual LV, CMF, FWHM, and STRM 3-SD methods .

pID	Manual	LV	CMF	FWHM	STRM 3SD
1	41.59	219.2	40.73	20.03	45.97
2	25.42	183.97	18.66	10.08	31.79
3	3.48	202.83	5.98	4.87	39.83
4	19.9	198.22	35.61	20.78	57.94
5	16.95	232.91	31.98	16.12	43.04
6	15.42	176.27	26.09	13.89	43.81
7	14.95	187.85	15.09	7.2	39.17
8	16.24	255.65	32.29	19.7	45.68
9	86.8	372.16	57.32	26.91	50.03
10	16.13	266.13	22.37	14.64	40.34
11	12.74	256.83	19.48	8.47	75.32
12	2.42	202.02	2.53	1.95	72.32
13	8.27	212.34	11.4	8.12	38.72
14	35.3	231.67	39.73	25.19	48.16
15	34.28	256.97	24.75	13.6	39.36
16	49.73	352.57	35.64	14.38	51.32
17	20.16	196.88	8.47	4.39	50.49
18	1.75	229.75	2.1	2.28	59.27
19	26.67	215.21	44.45	29.94	47.85
20	53.9	252.3	31.53	15.75	51.79
21	8.91	344.12	10.36	5.88	91.43

22	7.92	145.76	6.89	5.72	17.97
23	41.22	195.87	40.67	31.75	48.26
24	10.3	104.71	9.96	8.14	18.89
25	36.2	211.09	27.27	16.29	37.17
26	22.84	269.97	15.92	7.75	32.91
27	16.24	217.85	7.99	5.24	34.28
28	24.24	296.05	33.78	19.21	40.87
29	28.84	190.01	25.48	10.18	40.34
30	3.66	214.8	3.17	3.01	24.29
31	39.51	240.35	36.79	18.64	43.29
32	33.77	265.15	38.96	24.57	53.04
33	18.16	194.63	24.73	14.85	40.08
34	3.95	131.16	11.93	8.38	32.04
MIN	1.75	104.71	2.1	1.95	17.97
MAX	86.8	372.16	57.32	31.75	91.43
MEAN	23.47	227.15	23.53	13.47	44.91
STD	17.88	57.09	14.21	8.12	14.73

Appendix A.3 Volume Error and Absolute Volume Error Values of Scar using Different Segmentation Methods

Table 12: Volume Error (VE) and Absolute Volume Error of 34 3D LGE-MR images using CMF, FWHM, and STRM 3-SD methods.

pID	VE CMF	VE FWHM	VE STRM 3SD	AVE CMF	AVE FWHM	AVE STRM 3SD

1	-0.85	-21.56	4.39	0.85	21.56	4.39
2	-6.76	-15.34	6.37	6.76	15.34	6.37
3	2.5	1.39	36.35	2.5	1.39	36.35
4	15.71	0.88	38.04	15.71	0.88	38.04
5	15.04	-0.82	26.09	15.04	0.82	26.09
6	10.67	-1.53	28.39	10.67	1.53	28.39
7	0.15	-7.75	24.23	0.15	7.75	24.23
8	16.05	3.47	29.45	16.05	3.47	29.45
9	-29.48	-59.89	-36.77	29.48	59.89	36.77
10	6.24	-1.49	24.2	6.24	1.49	24.2
11	6.73	-4.27	62.57	6.73	4.27	62.57
12	0.11	-0.47	69.9	0.11	0.47	69.9
13	3.13	-0.15	30.45	3.13	0.15	30.45
14	4.43	-10.1	12.87	4.43	10.1	12.87
15	-9.53	-20.69	5.08	9.53	20.69	5.08
16	-14.09	-35.35	1.59	14.09	35.35	1.59
17	-11.68	-15.76	30.34	11.68	15.76	30.34
18	0.35	0.53	57.52	0.35	0.53	57.52
19	17.78	3.27	21.18	17.78	3.27	21.18
20	-22.37	-38.14	-2.11	22.37	38.14	2.11
21	1.45	-3.03	82.52	1.45	3.03	82.52
22	-1.03	-2.2	10.05	1.03	2.2	10.05
23	-0.55	-9.47	7.04	0.55	9.47	7.04
24	-0.34	-2.16	8.59	0.34	2.16	8.59
25	-8.93	-19.91	0.97	8.93	19.91	0.97
26	-6.91	-15.08	10.08	6.91	15.08	10.08
27	-8.25	-11.01	18.04	8.25	11.01	18.04

28	9.55	-5.03	16.63	9.55	5.03	16.63
29	-3.37	-18.67	11.5	3.37	18.67	11.5
30	-0.49	-0.65	20.62	0.49	0.65	20.62
31	-2.72	-20.87	3.77	2.72	20.87	3.77
32	5.19	-9.19	19.28	5.19	9.19	19.28
33	6.57	-3.31	21.92	6.57	3.31	21.92
34	7.98	4.43	28.09	7.98	4.43	28.09
MIN	-29.48	-59.89	-36.77	0.11	0.15	0.97
MAX	17.78	4.43	82.52	29.48	59.89	82.52
MEAN	0.07	-10	21.45	7.56	10.82	23.73
STD	10.39	13.77	22.44	7.01	13.12	19.93

Appendix A.4 Absolute Volume Percentage Error of Different Scar Segmentation Methods

Table 13: Absolute Volume Percentage (%) Error of 34 3D LGE-MR images using CMF, FWHM, and STRM 3-SD methods.

pID	CMF (%)	FWHM (%)	STRM 3SD (%)
1	2.05%	51.84%	10.55%
2	26.59%	60.34%	25.05%
3	71.85%	39.80%	1044.25%
4	78.94%	4.43%	191.16%
5	88.73%	4.86%	153.98%
6	69.18%	9.90%	184.08%

7	0.97%	51.84%	162.08%
8	98.86%	21.36%	181.38%
9	33.96%	69.00%	42.36%
10	38.65%	9.26%	150.02%
11	52.82%	33.51%	490.98%
12	4.59%	19.53%	2888.02%
13	37.87%	1.82%	368.08%
14	12.56%	28.62%	36.45%
15	27.81%	60.34%	14.82%
16	28.34%	71.08%	3.19%
17	57.96%	78.20%	150.52%
18	19.81%	30.08%	3285.24%
19	66.66%	12.25%	79.42%
20	41.50%	70.77%	3.91%
21	16.26%	34.02%	925.84%
22	13.05%	27.72%	126.94%
23	1.33%	22.96%	17.09%
24	3.27%	20.96%	83.40%
25	24.68%	55.00%	2.67%
26	30.27%	66.04%	44.13%
27	50.81%	67.75%	111.04%
28	39.39%	20.74%	68.64%
29	11.68%	64.72%	39.87%
30	13.52%	17.67%	563.19%
31	6.89%	52.82%	9.55%
32	15.37%	27.23%	57.08%
33	36.19%	18.23%	120.73%
34	201.90%	112.24%	711.17%

MIN	0.97%	1.82%	2.67%
MAX	201.90%	112.24%	3285.24%
MEAN	38.95%	39.32%	363.14%
STD	39.04%	26.36%	739.94%

Appendix A.5 Scar/Left-Ventricle Volume Fraction Percentage of Different Scar Segmentation Methods

Table 14: Scar/Left-Ventricle Volume Fraction (%) of 34 3D LGE-MR images using CMF, FWHM, and STRM 3-SD methods.

pID	Manual (%)	CMF (%)	FWHM (%)	STRM (%)
1	18.97%	18.58%	9.14%	20.97%
2	13.82%	10.14%	5.48%	17.28%
3	1.72%	2.95%	2.40%	19.64%
4	10.04%	17.96%	10.48%	29.23%
5	7.28%	13.73%	6.92%	18.48%
6	8.75%	14.80%	7.88%	24.85%
7	7.96%	8.03%	3.83%	20.85%
8	6.35%	12.63%	7.71%	17.87%
9	23.32%	15.40%	7.23%	13.44%
10	6.06%	8.41%	5.50%	15.16%
11	4.96%	7.58%	3.30%	29.33%
12	1.20%	1.25%	0.96%	35.80%
13	3.90%	5.37%	3.83%	18.24%

14	15.24%	17.15%	10.87%	20.79%
15	13.34%	9.63%	5.29%	15.32%
16	14.11%	10.11%	4.08%	14.56%
17	10.24%	4.30%	2.23%	25.65%
18	0.76%	0.91%	0.99%	25.80%
19	12.39%	20.65%	13.91%	22.24%
20	21.36%	12.50%	6.24%	20.53%
21	2.59%	3.01%	1.71%	26.57%
22	5.43%	4.72%	3.93%	12.33%
23	21.04%	20.76%	16.21%	24.64%
24	9.84%	9.52%	7.78%	18.04%
25	17.15%	12.92%	7.72%	17.61%
26	8.46%	5.90%	2.87%	12.19%
27	7.46%	3.67%	2.40%	15.74%
28	8.19%	11.41%	6.49%	13.81%
29	15.18%	13.41%	5.36%	21.23%
30	1.70%	1.47%	1.40%	11.31%
31	16.44%	15.31%	7.76%	18.01%
32	12.74%	14.69%	9.27%	20.01%
33	9.33%	12.71%	7.63%	20.59%
34	3.01%	9.09%	6.39%	24.43%
MIN	0.76%	0.91%	0.96%	11.31%
MAX	23.32%	20.76%	16.21%	35.80%
MEAN	10.01%	10.31%	6.04%	20.07%
STD	6.16%	5.66%	3.56%	5.52%

Results of 2D vs 3D Manual Scar Segmentation Study

Appendix A.6 Volumes of Manual Scar and Myocardium Segmentation Results

Table 15: Volumes of Manual Scar and Myocardium Segmentations using twenty-four 2D and 3D LGE-MRI. The myocardium is referred as LV below. The volumes of scar and myocardium are calculated in cm^3. The minimum, maximum, average and standard deviation values are presented for 24 patients data. The normalized scar volumes are calculated as fraction of scar volume and myocardium value, and multiplied by 100.

PID	3D Scar (cm^3)	3D LV (cm^3)	3D Scar/LV (%)	2D Scar (cm^3)	2D LV (cm^3)	2D Scar/LV (%)
1	16.3	187.85	8.68%	19.55	78.86	24.79%
2	18.65	255.65	7.30%	39.36	116.63	33.75%
3	92	371.25	24.78%	58.54	185.81	31.51%
4	22.82	266.13	8.57%	26.32	123.25	21.35%
5	4.22	202.02	2.09%	22.08	159.65	13.83%
6	11.28	212.34	5.31%	15.26	123.01	12.41%
7	57.29	351.92	16.28%	11	179.1	6.14%
8	2.36	229.75	1.03%	18.36	135.06	13.59%
9	28.68	213.03	13.46%	16.33	159.49	10.24%
10	59.87	252.04	23.75%	32.57	132.44	24.59%
11	9.99	344.12	2.90%	8.8	192.28	4.58%
12	10.39	145.76	7.13%	11.33	70.28	16.12%
13	47.15	195.87	24.07%	34.88	115.26	30.26%

14	11.77	104.71	11.24%	19.86	68.02	29.20%
15	39.91	211.09	18.91%	23.75	80.23	29.60%
16	25.34	269.97	9.39%	22.44	118.34	18.96%
17	21.9	216.04	10.14%	32.19	94.22	34.16%
18	25.74	296.02	8.70%	12.91	104.32	12.38%
19	30.25	190.01	15.92%	15.67	100.1	15.65%
20	5.9	214.37	2.75%	4.14	111.42	3.72%
21	44.51	240.09	18.54%	14.72	146.44	10.05%
22	39.1	265.15	14.75%	12.02	156.07	7.70%
23	20.11	194.63	10.33%	22.09	118.3	18.67%
24	5.11	131.16	3.90%	5.17	83.77	6.17%
min	2.36	104.71	1.03%	4.14	68.02	3.72%
max	92	371.25	24.78%	58.54	192.28	34.16%
mean	27.11	231.707	11.25%	20.806	123.015	17.89%
std	21.504	65.291	7.10%	12.147	35.84	9.80%

Appendix A.7 Shape Metrics of Manual Scar and Myocardium Segmentation Results

Table 16: Shape metrics of manual scar segmentations from 2D and 3D LGE-MRI using twenty-four LGE-MRI. The fractal dimensions (FD) reported between 1 and 3. The number of connected components is (NCC) calculated for 2D and 3D. The minimum, maximum, average and standard deviation values are presented for 24 patients data.

PID	3D FD [1-3]	2D FD [1-3]	3D NCC (count)	2D NCC (count)
1	2.19	1.89	3	2
2	2.15	2.17	7	2
3	2.41	2.08	81	7
4	2.17	1.95	36	4
5	2	2.01	15	8
6	2.1	1.81	9	9
7	2.17	1.73	5	12
8	2.13	1.7	2	19
9	2.34	1.65	5	13
10	2.33	1.91	1	7
11	2.29	1.49	11	3
12	2.14	1.95	5	4
13	2.27	1.94	2	5
14	2.13	1.95	3	5
15	2.32	2.03	1	4
16	2.31	1.85	2	5
17	2.2	2.08	1	5
18	2.2	1.74	5	5
19	2.35	1.95	2	7

20	2	1.48	1	6
21	2.3	1.62	2	5
22	2.26	1.67	5	8
23	2.18	2.02	4	2
24	1.94	1.7	5	4
min	1.944	1.48	1	2
max	2.409	2.174	81	19
mean	2.204	1.849	8.875	6.292
std	0.12	0.188	17.005	3.906